Dipl.-Ing. Eva-Maria Steyskal

Porous Nanophase Metals with Electrochemically Tunable Properties Studied By Resistometry and Dilatometry

DOCTORAL THESIS

to achieve the university degree

Doktorin der technischen Wissenschaften

submitted to

Graz University of Technology

Supervisor:

Univ.-Prof. Dr.rer.nat. Roland Würschum

Institut für Materialphysik

Graz, March 2017

To Isabella and Konstantin

Abstract

Owing to extraordinary high surface-to-volume ratios, porous nanophase metals are actively studied in various fields, ranging from basic research to technology applications such as sensing, energy storage or (electro-)catalysis. The present thesis studies property variations of porous nanophase samples due to electrochemical stimuli. The porous sample materials are prepared by nanopowder compaction (Pt, Pd) as well as dealloying (Au, Pt, Pd), an (electro-)chemical etching process in which the less noble component is removed from a master alloy by selective etching. By this method nanoporous metals with three-dimensionally macroscopic outer dimensions can be generated in quasi unrestrained shape.

The optimization of dealloying is an active research topic, since the attractive properties of the outcoming nanostructures may be sensitively influenced by the parameters of the etching process. In the present work the dealloying process is studied in-situ by resistometry for the first time, dynamically monitoring the entire macroscopic sample. During etching, the resistance increases by about three orders of magnitude due to porosity formation and concommitant oxide formation. Taking into account the consumed charge, modeling of the resistance variations shows that the etching proceeds in two stages. These stages denoted 'primary (or bulk) dealloying' and 'secondary (or ligament) dealloying' were proposed recently based on ex-situ SEM investigations and could be confirmed by an in-situ study for the first time in the framework of the present thesis.

Due to their high specific surface areas, porous nanophase metals are also predestined systems for property tuning by electrochemical charging, since surface modifications may affect a considerable fraction of the bulk material. In this work the charging-induced actua-

tion and resistance variation are studied in different electrochemical conditions, in particular in the double layer and oxygen regime. Dealloyed metals show adsorption-driven resistance variations up to several tens of percents, which are attributed mainly to manipulations of the interfacial charge-carrier scattering and which by almost one order of magnitude exceed those observed for the powder compacted samples. The stronger sensitivity of the dealloyed metals can be attributed to their higher surface-to-volume ratio.

For platinum, also the primary oxide, a strongly oxidized condition formed during dealloying, is investigated, exhibiting particular properties. Upon charging, primary oxide samples show an actuation with opposed sign compared to the well-reduced (metallic) condition. In resistometry even a sign inversion in the resistance-to-charge response is observed during scanning within the primary oxide regime.

Since Pd is a frequently used model system for hydrogen storage, well known for its ability to absorb hydrogen from the gas phase as well as by electrochemical charging, the nanoporous palladium structures were especially investigated with regards to their hydrogenation characteristics. Both the electrical resistance and the specific volume of palladium are highly sensitive tools which enable the in-situ monitoring of the hydrogen content during charging. By suitable loading procedures, hydrogen concentrations up to almost 60 % H:Pd were obtained, along with a sample thickness increase of about 5 %. The observed reversible acutation clearly exceeds the values available in the literature, which is most likely due to the unique structure of np-Pd with its high specific surface area.

Kurzfassung

Das Interesse an porösen, nanophasigen Metallen, welche sich durch ein hohes Verhältnis von Oberfläche zu Volumen auszeichnen, ist breit gefächtert. Es erstreckt sich von Themen der Grundlagenforschung bis hin zu technologischen Anwendungen wie Sensorik, Energiespeicherung oder (Elektro-)Katalyse. Die vorliegende Arbeit behandelt elektrochemisch verursachte Änderungen der physikalischen Eigenschaften poröser Metalle. Untersucht werden hierbei sowohl kompaktierte Nanopulver (Pt, Pd) als auch nanoporöse Metalle (Au, Pt, Pd), hergestellt durch sogeanntes 'Dealloying', einen (elektro-)chemischen Entlegierungsprozess bei welchem die unedlere Komponente selektiv aus einer Legierung geätzt wird. Durch diesen Prozess lassen sich in quasi uneingeschränkter Form nanoporöse Metalle mit makroskopischen Abmessungen in drei Dimensionen herstellen.

Die Optimierung des Dealloying-Prozesses ist ein Thema aktiver, aktueller Forschung, da die vorteilhaften Eigenschaften der erzeugten Nanostrukturen durch verschiedene Prozessparameter empfindlich beeinflusst werden können. In der vorliegenden Arbeit wurden erstmals in-situ Widerstandsmessungen während des Entlegierungsvorgangs durchgeführt, wodurch die gesamte makroskopische Probe dynamisch beobachtet werden konnte. Durch die Entstehung der Porosität und gleichzeitige Oxidbildung steigt der gemessene Widerstand während des Ätzprozesses um etwa drei Größenordnungen an. Basierend auf den Messergebnissen wird ein Modell aufgestellt, welches die Widerstandsänderung näherungsweise aufgrund der Abnahme des Querschnitts der Ausgangslegierung beschreibt. Im Einklang mit früheren Ergebnissen aus ex-situ Elektronenmikroskopiestudien können während des Ätzvorgangs zwei Subprozesse unterschieden werden: 'primäres (oder Bulk-) Dealloying' und 'sekundäres (oder

Ligament-) Dealloying'.

Aufgrund der hohen spezifischen Oberfläche poröser, nanophasiger Materialien lassen sich ihre Eigenschaften empfindlich durch elektrochemische Beladung beeinflussen, da von oberflächlichen Veränderungen ein hoher Anteil des Gesamtvolumens betroffen ist. In dieser Arbeit werden Volumen- und Widerstandsänderungen der Probenmaterialien in verschiedenen elektrochemischen Zuständen untersucht, insbesondere im Doppelschicht- und Sauerstoffbereich. Durch Adsorption können in entlegierten, nanoporösen Materialien Widerstandsänderungen bis in den hohen zweistelligen Prozentbereich generiert werden, die hauptsächlich aufgrund von Änderungen der Ladungsträgerstreuung an der Metall-Elektrolyt-Grenzfläche zustande kommen und welche jene von kompaktierten Nanopulvern um fast eine Größenordnung übersteigen. Diese höhere Empfindlichkeit der mittels Dealloying hergestellten Proben kann ihrer höheren spezifischen Oberfläche zugeschrieben werden.

Für Platin wurde auch das sogenannte 'Primäroxid' untersucht, ein stark oxidierter Zustand, der während des Ätzprozesses entsteht und der besondere Eigenschaften aufweist. Eine elektrochemische Beladung führt im Primäroxid-Zustand zu einer Längenänderung, deren Vorzeichen jener einer reduzierten (metallischen) Probe entgegengesetzt ist. Bei der Messung des Widerstandes wird sogar eine Vorzeichenumkehr der Widerstands-Ladungs-Charakteristik während der Beladung innerhalb des Primäroxid-Zustandes beobachtet.

Da Pd ein zentrales Modellsystem für Wasserstoffspeicherung darstellt, welches Wasserstoff sowohl aus der Gasphase als auch bei elektrochemischer Beladung aufnehmen kann, wurden die nanoporösen Palladiumproben in dieser Arbeit insbesondere auch in Hinblick auf Wasserstoffeinbau untersucht. Sowohl der elektrische Widerstand als auch das spezifische Volumen von Palladium stellen empfindliche Messgrößen für die in-situ Charakterisierung des Wasserstoffgehalts dar. Durch geeignete Beladeprogramme wurden Wasserstoffkonzentrationen von etwa 60 % H:Pd erreicht, verbunden mit einer Längenänderung von etwa 5 %. Diese erzielte reversible Ausdehnung ist deutlich höher als vergleichbare Werte in der Literatur, was der einzigartigen Struktur von np-Pd mit einer hohen spezifischen Oberfläche zugeschrieben wird.

Table of Contents

1 | Introduction

Porous materials are like music: the gaps are as important as the filled-in bits. [1]

This sentence, quoted from the book *Nanoporous Materials: Science and Engineering* by G. Q. Lu and X. S. Zhao [1], metaphorically describes the fact that porosity significantly influences the properties and associated functionalities of a material, compared to its bulk structured counterpart. The variety of porous structures used in science and engineering covers many material categories, such as polymers, glasses, oxides or metals, and their fields of application are just as diverse. Generally, porous materials can be divided into two groups, characterized by open porosity (connected to the surface) or closed pores. While, open pore structures are used, for example, in catalysis, adsorption or sensing applications, closed pores are desired in insulating or light-weight structural materials [1].

One particularly interesting sub-category of porous materials are nanoporous materials, which, due to their nanostructure, possess unique properties, especially a high surface-to-volume ratio. The term 'nanoporous' typically refers to large porosities, higher than 40 %, and pore sizes in the range of $1 - 100$ nm [1], which according to the pore size definition of the *International Union of Pure and Applied Chemistry* (*IUPAC*) includes all mesoporous ($2 - 50$ nm) but also some microporous (< 2 nm) and macroporous (> 50 nm) materials [2].

The methods to generate nanoporosity can be divided into bottom-up and top-down approaches. Bottom-up denotes the formation of the final structure by smaller building blocks. The most simple realization of this approach would be the loose compaction of a nanopowder, optionally followed by sintering, but also many advanced methods such as different deposition and self-assembly processes are known in the literature. In top-down techniques, on the other hand, the nanostructures evolve due to a controlled removal of material from a solid (bulk) sample. Among them, by far, lithographic methods are most widely used, however, also several chemical top-down processes are known in the literature such as thermal decomposition or in particular dealloying [3], which will be the formation process of major importance for this thesis.

Dealloying denotes an (electro-)chemical technique in which one or more less noble elements are removed from a bulk master alloy by selective etching, which results in a nanoscale, bicontinuous structure of pores and solid network branches (ligaments), consisting of the more noble component(s) [4]. By this method nanoporous metals can be fabricated in quasi unrestrained shape, combining nanoporosity-related desirable properties with macroscopic size in three dimensions. By far the most intensively studied dealloyed material is nanoporous gold (np-Au), selectively etched from Ag-Au master alloys, with typical pore sizes in the range of tens of nanometers. However, also a variety of other dealloyable systems is known in the literature in some of which, depending on the involved elements and dealloying parameters, ligament diameters and pore sizes as low as a few nanometers can be achieved [5].

Dealloyed materials, which exhibit extraordinarily high surface-to-volume ratios, are successfully used in many important fields of science and technology, such as sensing [6, 7], energy storage [8, 9] or (electro-)catalysis [10–15]. Growing research interest is also placed on the attractive biological applications of the nanoporous metal structures. Besides pioneering studies on biosensing [16] and biocatalytic activity [17], dealloyed materials show promising performance as materials for implantation [18, 19] or selective drug release [20, 21].

The high surface-to-volume ratio also makes nanoporous materials predestined systems

for property tuning by electrochemical stimuli, since surface modifications may affect a considerable fraction of the bulk material [22]. Following first studies on nanoporous metals made by powder compaction [23, 24], property tuning of dealloyed nanoporous gold has successfully been demonstrated in the literature, e.g., with respect to various mechanical properties [25–27] as well as electrical resistance [28, 29].

In the present thesis porous nanophase gold, platinum and palladium are studied. The major focus lies on electrochemically induced resistance variations, based on previous investigations in our group by M. Sagmeister et al. [24], representing the first resistance tuning study of a three-dimensionally macroscopic metallic material, and P. Wahl et al. [29], in which the highest adsorption-driven resistance variation of a dealloyed material could be achieved prior to the present thesis. The resistometric results are supported by dilatometry data as well as by structural and chemical analysis.

The electrical resistance and actuation of the porous nanophase samples are dynamically monitored in-situ upon different electrochemical charging procedures, especially in the double layer regime as well as upon specific ad/desorption. For dealloyed metals also the primary oxide, a strongly oxidized condition due to the etching process associated with peculiar properties, is investigated in detail. In the case of palladium, a special focus is placed on the hydrogen absorption characteristics and associated property variations of the porous nanostructure. Moreover the first in-situ resistometric study of the dealloying process itself is presented, which is used for the development of a model capable of describing the etching progress.

A list of publications arising from this work is given on the following pages.

List of Peer Reviewed Publications

directly related to this thesis

Steyskal, E.-M.; Qi, Z.; Pölt, P.; Albu, M.; Weissmüller, J.; Würschum, R.
Electrochemically Tunable Resistance of Nanoporous Platinum Produced by Dealloying
Langmuir, Volume 32, Issue 31, 2016, Pages 7757-7764

Cited as reference [30]
Author contributions: E.-M. Steyskal prepared the nanoporous samples by dealloying, designed and performed the property tuning experiments, conducted the data analysis and wrote the manuscript. Final editing of the manuscript was done in collaboration with the co-authors. Z. Qi and J. Weissmüller synthesized the master alloys for dealloying and participated in the discussion of the experimental results. P. Pölt and M. Albu performed the SEM and TEM investigations respectively. R. Würschum supervised the research project as well as the manuscript writing.

Steyskal, E.-M.; Wiednig, C.; Enzinger, N.; Würschum, R.
In Situ Characterization of Hydrogen Absorption in Nanoporous Palladium Produced by Dealloying
Beilstein Journal of Nanotechnology, Volume 7, Issue 1, 2016, Pages 1197-1201

Cited as reference [31]
Author contributions: E.-M. Steyskal prepared the nanoporous samples by dealloying, designed and performed all experiments, conducted the data analysis and wrote the manuscript. Final editing of the manuscript was done in collaboration with the co-authors. C. Wiednig and N. Enzinger synthesized the master alloys for dealloying. R. Würschum supervised the research project as well as the manuscript writing.

Steyskal, E.-M.; Topolovec, S.; Landgraf, S.; Krenn, H.; Würschum, R.
In situ monitoring magnetism and resistance of nanophase platinum upon electrochemical oxidation
Beilstein Journal of Nanotechnology, Volume 4, Issue 1, 2013, Pages 394-399

Cited as reference [32]
Author contributions: E.-M. Steyskal designed and performed all experiments as well as the data analysis regarding resistometry. S. Topolovec designed and performed all experiments as well as the data analysis regarding magnetometry. E.-M. Steyskal drafted and wrote the manuscript, supported by S. Topolovec. Final editing of the manuscript was done in collaboration with all co-authors. H. Krenn supervised the magnetic measurements with the SQUID magnetometer and participated in the discussion of the results. S. Landgraf was involved in the discussion and interpretation of the electrochemical results. R. Würschum supervised the research project as well as the manuscript writing.

Steyskal, E.-M.; Besenhard, M.; Landgraf, S.; Zhong, Y.; Weissmüller, J.; Pölt, P.; Albu, M.; Würschum, R.
Sign-inversion of charging-induced variation of electrical resistance of nanoporous platinum
Journal of Applied Physics, Volume 112, Issue 7, 2012, Article number 073703

Cited as reference [33]
Author contributions: E.-M. Steyskal performed all property tuning experiments as well as the data analysis and wrote the manuscript. Final editing of the manuscript was done in collaboration with the co-authors. The design of the experimental setup as well as preliminary testing was done by M. Besenhard. S. Landgraf prepared the nanoporous Pt samples by electrochemical dealloying. Y. Zhong and J. Weissmüller synthesized the master alloys for dealloying and participated in the discussion of the experimental results. P. Pölt and M. Albu performed the SEM and TEM investigations respectively. R. Würschum supervised the research project as well as the manuscript writing.

List of Peer Reviewed Publications

in other research areas

Steyskal, E.-M.; Oberdorfer, B.; Sprengel, W.; Zehetbauer, M.; Pippan, R.; Würschum, R.
Direct experimental determination of grain boundary excess volume in metals
Physical Review Letters, Volume 108, Issue 5, 2012, Article number 055504

Kotzurek, J.; Steyskal, E.-M.; Oberdorfer, B.; Hohenwarter, A.; Pippan, R.; Sprengel, W.; Würschum, R.
Direct measurement of vacancy relaxation by dilatometry
Applied Physics Letters, Volume 109, Issue 2, 2016, Article number 021906

Oberdorfer, B.; Setman, D.; Steyskal, E.-M.; Hohenwarter, A.; Sprengel, W.; Zehetbauer, M.; Pippan, R.; Würschum, R.
Grain boundary excess volume and defect annealing of copper after high-pressure torsion
Acta Materialia, Volume 68, 2014, Pages 189-195

Oberdorfer, B.; Steyskal, E.-M.; Sprengel, W.; Pippan, R.; Zehetbauer, M.; Puff, W.; Würschum, R.
Recrystallization kinetics of ultrafine-grained Ni studied by dilatometry
Journal of Alloys and Compounds, Volume 509, Issue SUPPL. 1, 2011, Pages S309-S311

Würschum, R.; Oberdorfer, B.; Steyskal, E.-M.; Sprengel, W.; Puff, W.; Pikart, P.; Hugenschmidt, C.; Pippan, R.
Free volumes in bulk nanocrystalline metals studied by the complementary techniques of positron annihilation and dilatometry
Physica B: Condensed Matter, Volume 407, Issue 14, 2012, Pages 2670-2675

Sprengel, W.; Oberdorfer, B.; Steyskal, E.-M.; Würschum, R.
Dilatometry: A powerful tool for the study of defects in ultrafine-grained metals
Journal of Materials Science, Volume 47, Issue 22, 2012, Pages 7921-7925

Oberdorfer, B.; Steyskal, E. -M.; Sprengel, W.; Puff, W.; Pikart, P.; Hugenschmidt, C.; Zehetbauer, M.; Pippan, R.; Würschum, R.
In-situ probing of fast defect annealing in Cu and Ni with a high-intensity positron beam
Physical Review Letters, Volume 105, Issue 14, 2010, Article number 146101

2 | Basics and State of the Art

In this chapter, the most important basics as well as modern research forming the basis for this thesis will be introduced. Such a summary cannot make any claim to be complete, but should be seen as a brief overview. For more detailed information, selected references are given in each section. After an introduction to electrochemical surface processes relevant for this thesis, the fabrication and properties of nanoporous metals, mainly produced by dealloying, will be discussed.

2.1 Electrochemistry at Electrode Surfaces

The phase boundary between a (liquid) electrolyte and an immersed (solid metal) electrode also represents a boundary between regions with different conduction mechanisms and charge carrier concentrations: while in the electrolyte charge is carried by dissolved ions of different sign, in the metal we find free (negative) electrons and fixed (positive) ionic cores. Depending on the system, a variety of interactions can take place between these phases. The term 'electrochemical reaction' summarizes all redox reactions in which charge is transferred across the interface. [34]

Since no potential can be assigned to a single redox couple, but only potential differences between two couples can be measured, a general reference point has to be determined for

the comparison of different reactions. The electrochemical series is based on the standard hydrogen electrode with the redox system

$$H_2 + 2H_2O \leftrightarrow 2H_3O^+ + 2e^- \tag{2.1}$$

which is associated with an (arbitrarily chosen) potential of 0 V. [34]

The equilibrium potential of a redox couple φ_0 is dependent on the concentration of the electrolytic components involved and can be described by the Nernst equation

$$\varphi_0 = \varphi_{00} + \frac{RT}{nF} \ln \frac{[\mathrm{Ox}]}{[\mathrm{Red}]} \tag{2.2}$$

with the standard potential φ_{00}, the gas constant R, the Faraday constant F, the valence n of the ionic species, the temperature T and the concentrations [x] of the respective components. The concentration of a pure, solid phase (e.g. metal electrode) equals one. [34]

In general, due to the electrochemical potential difference between the electrode and the electrolyte, regions of opposite charge accumulation will form on both sides of the interface, the so-called electrochemical double layer (see figure 2.1A), even if no external potential is applied to the system. Due to the excellent conductivity of a metal (high density of small, mobile electrons), the excess charge in the electrode is confined to a narrow surface layer with a thickness of no more than about 1 Å. The charge carrier concentration in the electrolyte (at common concentrations between 10^{-3} and 1 mol/l) is by orders of magnitude smaller, which leads to a significantly wider spread double layer in the solution, typically between 5 and 20 Å. [34]

In the electrochemical double layer regime no charge is transferred across the interface and the system electrolyte–electrode can be considered similar to a capacitor, which exhibits a linear relationship between applied potential and stored charge. In a simplified model (Helmholtz model) the electrode surface can be considered as covered by a rigid ionic layer, separated by the solvation shell of the ions. The plane carrying the centers of the solvated ions is accordingly called the outer Helmholtz plane. [35]

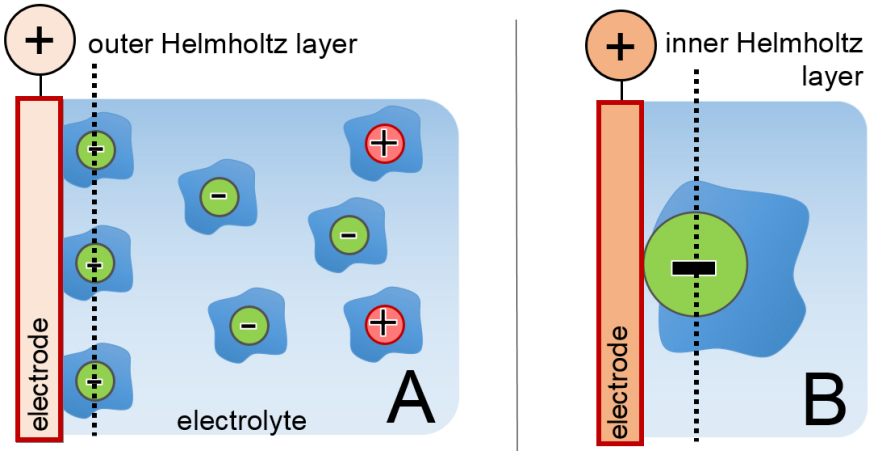

Figure 2.1: Electrochemical processes at a positively charged electrode. (A) Double layer formation in Stern model, combining a rigid and a diffuse component. (B) Specific adsorption of an anion, partially stripping off its solvation shell.

When this simple Helmholtz-model is applied to the picture of the capacitor, the distance between the electrode surface and the outer Helmholtz layer would represent the separation of the capacitor plates. This however strongly overestimates the actual capacity of a double layer as determined experimentally. For an accurate description, a combination of the rigid double layer (Helmholtz model) and a diffuse electrolytic double layer, decreasing with distance to the electrode (as proposed by Gouy and Chapman) is necessary, which is given by the so-called Stern model. [35]

Most electrochemical reactions, characterized by charge transfer across the interface, involve an ionic adsorption step. For an ion, solvatized in an electrolyte, to 'specifically adsorb' at least partially it has to strip off its solvation shell which is illustrated in figure 2.1B. Specific adsorption is particularly favorable for anions due to their larger ionic radii and therefore weaker bound solvation shells. The plane passing through the specifically adsorbed species is called the inner Helmholtz plane accordingly. [35]

2.2 Dealloying and Dealloyed Materials

Dealloying is an (electro-)chemical process, in which one or more of the less noble elements are removed from a master alloy by selective etching. The history of metal processing in

such a way dates back to Pre-Columbian South America where selective etching of Au-Cu alloys was applied during the fabrication of different cultural objects [36].

In research, dealloying was studied for a long time mainly with regards to unwanted selective corrosion, which may lead to an accelerated failure of the affected materials [37, 38]. During the past three decades, however, a rapidly growing interest was placed on the superior properties of nanoporous metals specifically designed by selective etching, which were introduced in pioneering works by R. Li et al. [39] and J. Erlebacher et al. [4] and which have triggered countless follow-up studies, theoretically and experimentally investigating the etching process itself as well as the properties of the outcoming materials.

A sketch of the evolution of nanoporosity during a dealloying experiment is given in figure 2.2. The underlying mechanisms can briefly be described as follows: At the beginning of an electrochemical dealloying experiment an alloy, usually a solid solution, in which the more noble element is present in dilute concentration, is immersed into an electrolyte and set at a potential, which is suitable for selectively etching the less noble component. During the etching process, atoms of the less noble component are dissolved into the electrolyte, leaving behind surface vacancies, while the more noble atoms tend to seek energetically favorable, low coordinate positions by surface diffusion. In early stages of the etching experiment this rearrangement leads to the formation of noble element islands on top of the bulk alloy. As the dealloying proceeds and the etching front penetrates deeper into the bulk, cavities are formed in between the islands, which finally leads to a bicontinuous structure of a spongy metallic network, riddled with fine pores. [40]

The branches of the metallic network formed by dealloying, the so called ligaments, exhibit a composition gradient with almost pure layers of the more noble element near the surface and higher concentrations of the less noble alloy partner in the middle [13]. The average distances of the islands formed during dealloying, and in further consequence the pore and ligament sizes, are characteristic for the elements involved, i.e., strongly dependent on the surface diffusivities and thus on the melting points of the respective materials. In fact, it was shown by Chen et al. that the ligament diameters of dealloyed, nanoporous

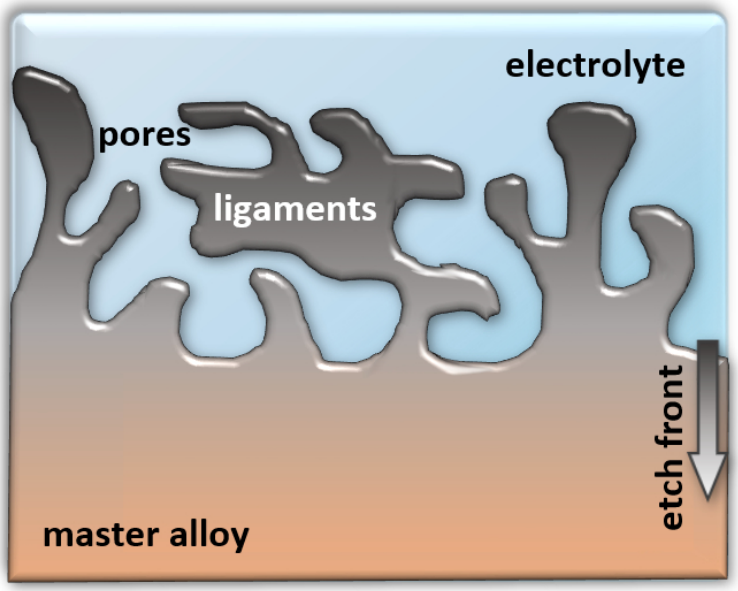

Figure 2.2: Schematic illustration of the etching front propagation into an alloy during a dealloying experiment, leaving behind a nanoporous structure of the more noble element.

materials logarithmically decrease with the melting point of the host reservoir [5].

The etching process itself, with its variety of adjustable parameters, strongly influences the properties of the outcoming nanostructures. Not only pore- and ligament sizes, but also macroscopic shrinkage, internal stresses, oxide formation, or the concentration of the less noble component remaining in the porous network may be affected by the experimental conditions. In order to achieve a deeper understanding of the underlying mechanisms, the processes at the etching front are discussed intensively in the literature. Available studies include computer simulations [4,41], X-ray [42,43] and imaging techniques [44,45]. However it should be pointed out here, that all mentioned experiments were conducted ex-situ and/or sensitive to surfaces or thin films with a maximum thickness of several micrometers only.

By far the most intensively studied dealloyed material is nanoporous gold (np-Au) produced from Ag-Au master alloys, which typically exhibits ligament sizes in the range of 20 nm [46]. Nanoporosity can be achieved by free corrosion, usually in nitric acid (HNO_3) solutions [47], as well as potential-assisted, e.g. in perchloric acid ($HClO_4$) [39] or neutral silver nitrate ($AgNO_3$) solution [48]. Successful dealloying requires a suitable composition

of the master alloy, which for Ag-Au lies between 15 and 40 wt% Au [49]. While the lower limit is given by a continuous formation of a percolating network, the upper boundary, the so called parting limit, represents the case of passivation during etching: if the concentration of the more noble component is too high in the master alloy, the rearrangement processes during etching will lead to a dense surface layer of the more noble element covering the master alloy, which inhibits further dissolution processes.

Even though the above mentioned np-Au produced from Ag-Au alloys represents the most common case, also a variety of other dealloyable systems are known in the literature, e.g. nanoporous silver [50], platinum [51], palladium [52], copper [53], or nickel [54]. Moreover also master alloy systems other than binary solid solutions are studied with regard to improving the properties of the outcoming nanostructures. For example, a stabilizing backbone for the brittle nanoporous structure can be introduced with multi-phase master alloys (Ag-Pt). [55] Moreover it was shown that, compared to typical nanoporous gold dealloyed from Ag-Au, finer porosities can be achieved by dealloying ternary alloys which contain a higher-melting minor component that inhibits structural rearrangements, as reported for the Ag-Au-Pt system [56].

In the present work, besides np-Au, nanoporous platinum (np-Pt), produced from Cu-Pt, [51] and nanoporous palladium, produced from Co-Pd, [52] will be studied with regard to electrochemically induced property variations. Both systems, which can be etched in sulphuric acid (H_2SO_4) solutions, show extraordinarily fine porosities with ligament diameters of only a few nanometers due to their high melting points.

2.3 Nanostructured Materials with Tunable Properties

The concept of bulk nanostructured metals with electrochemically tunable properties, which was proposed by Gleiter at al. in 2001 [22], makes use of the high surface-to-volume ratio inherent to porous nanophase structures. When a dense bulk metal is subjected to an external electric field or, as sketched in figure 2.3 (left), is charged as an electrode immersed

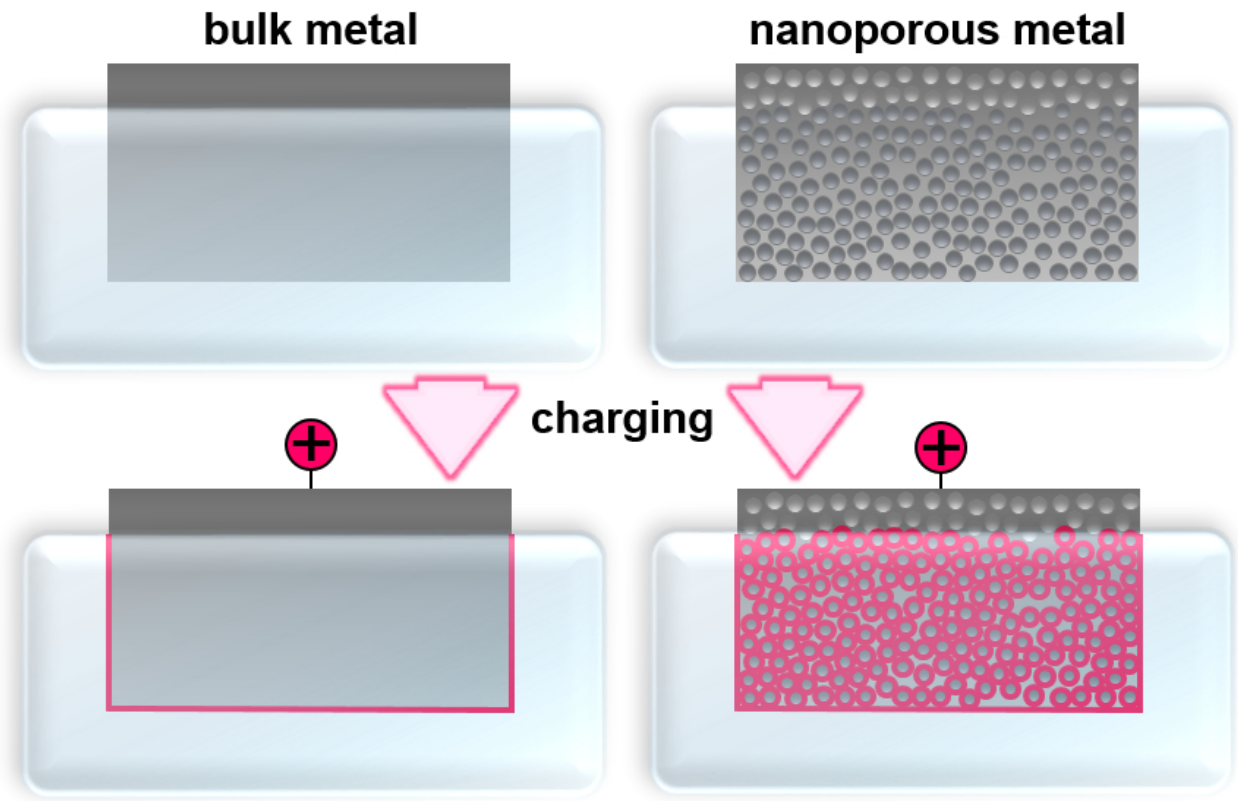

Figure 2.3: Concept of property tuning using porous nanophase metals. While electrochemical surface charging hardly affects the bulk properties of a dense electrode (left), charging-induced surface effects may alter the macroscopic properties of a nanoporous material (right) due to the high surface to volume ratio.

in an electrolyte, the concommitant effects will be restricted to superficial regions (sketched in pink) of the metallic material: Due to the effective screening of metals, associated with their high conductivity, an applied electric field decays rapidly within only a few surface atomic layers, while the major part of the charged electrode remains field-free, resulting in unaltered bulk properties of the material.

Significant effects can be generated, however, when instead of a macroscopically sized, dense metal electrode a nanophase metal with continuous porosity is used (figure 2.3, right). In this case all internal surfaces of pores, penetrated by the electrolyte, can be charged by applying a potential to the metal. Due to the high surface-to-volume ratio, a charging-induced influence on surface layers affects a substantial volume fraction of the material and may therefore lead to variations of the macroscopic properties of the material.

In such a way, a variety of physical bulk properties of metallic conductors can be tuned reversibly, ranging from optical [57, 58] and magnetic [32, 59–61] to electrical [24, 28–32] and mechanical [23, 27, 62] properties. Since the focus of this work lies on the tunable electrical resistance and actuation behavior of porous nanophase metals, a more detailed literature overview of the key results regarding these effects will be presented in the following.

Tunable Electrical Resistance

Experiments on charging-induced resistance tuning of nanostructures, including metallic ones, reach back by far earlier than to the year 2001, when the above mentioned concept was published by Gleiter et al. [22]. Those early studies were however restricted to thin film structures or nanoscale wires of (semi-)precious metals, with a strong focus on silver. A summary in chronological order is given in table 2.1.

A first study, published in 1956, presented the influence of electrostatic charging on the resistance of silver thin films [63], resulting in resistance variations in the range of 10^{-4} %. A variety of electrochemical resistance tuning experiments followed during the decades, starting in the 1960s, which investigated resistance variations upon double layer charging as well as adsorption/corrosion phenomena [64–74], presenting resistance variations up to 80 % by corrosion [68] or 20 % upon reversible charging [70]. Moreover, after this initial study of the resistance senisitivity to the adsorption of different halide ions [70] also sensing applications based on resistance variations of thin metal films were published [75]. Among the just mentioned references, a detailed review article by Tucceri [72], representing an excellent overview on surface resistance measurements in electrochemistry, should be pointed out particularly.

The first successful resistance tuning of a three dimensionally macroscopic sample material following the concept of Gleiter [22] was published by our group in 2006 [24]. In the experiment presented by Sagmeister et al. a Pt nanopowder pellet with a mass of 120 mg, produced by compacting commercial Platinum Black, exhibited resistance variations up to

Table 2.1: Charging-induced resistance variations of metal and alloy nanostructures reported in the literature.

First Author	**Year**	**Material(s)**	**Electrochemical Regimes**				**Maximum Variation** $\Delta R/R$ [%]
			Double Layer	Adsorption	Corrosion	Deposition	
Deubner [63]	1956	Ag thin films (electrostatic charging)					10^{-4}
Shimizu [64, 65]	1968	Pt thin films	×	×			10
Dickinson [66]	1974	Pt thin films	×	×	×		12
Tucceri [67]	1990	Ag thin films	×	×			2
Körwer [68]	1991	Ag thin films		×	×	×	80
Hanewinkel [70]	1997	Ag thin films		×			20
Xu [71]	2002	Au thin wires	×	×			10
Tucceri [72] (review)	2004	Ag, Au, Pt thin films	×	×	×		
Schöning [75]	2004					×	
Sagmeister [24]	2006	Pt nanopowder	×	×			8
Bansal [76]	2007	Au-Fe nanopowder	×				1.3
Dasgupta [73]	2008	Au thin films	×				1.5
Mishra [28]	2008	Au, dealloyed	×				6
Wahl [29]	2010	Au, dealloyed	×	×			43
Steyskal [33]	2012	Pt, dealloyed (present thesis)	×				4
Steyskal [32]	2013	Pt nanopowder (present thesis)	×	×			6
Ding [74]	2015	Pt nanowires	×	×			15
Bai [77]	2016	Ag, dealloyed	×	×	×		1100
Steyskal [30]	2016	Pt, dealloyed (present thesis)	×	×			58
Steyskal [31]	2016	Pd, dealloyed (present thesis)	×	×			30

8 % upon electrochemical charging. Follow-up studies on compacted nanopowders investigated Au-Fe [76] and, in the framework of this thesis, different electrochemical charging regimes of Platinum Black, which was published in reference [32].

A particularly interesting group of candidates for property tuning is represented by nanoporous metals produced by dealloying, which offer a higher freedom of design. During the past few years a variety of property tuning experiments has been published for this class of materials, with a strong focus on mechanical properties (e.g. see reference [78]). Resistance variations upon electrochemical charging have been studied in the literature using dealloyed nanoporous gold [28, 29] and silver [77]. In the present thesis R-tuning of platinum [30,33] and palladium [31] was investigated. Due to significantly enhanced surface-to-volume ratios compared to compacted powder pellets dealloyed materials showed strong resistance variations of 6 % in the double layer (nanoporous gold) [28] and up to 58 % in the adsorption regime (nanoporous platinum, present work, published in reference [30]) or, in the case of less noble silver, even a resistance increase by more than 1000 % due to corrosion [77].

In the present thesis, the major focus of resistance tuning experiments will be placed on the electrochemical regimes of double layer charging and adsorption. In the latter the observed behavior is exclusively dominated by scattering processes at the metal-electrolyte interfaces [29], while in the double layer regime also variations in the charge carrier density give a considerable resistance contribution [24]. Significant resistance variations caused by electrochemically induced actuation could be excluded in both electrochemical regimes. A detailed evaluation of the respective contributions for the present data will be given in chapter 5.2.

In the literature also studies of the charging induced resistance changes of various carbon materials can be found. A brief overview of the available data is given in table 2.2. Interestingly, besides high field-induced resistance variations, these materials show a sign inversion behavior of the resistance variation upon electrochemical charging, similar to that observed for freshly dealloyed nanoporous platinum ('primary oxide condition'), which will be discussed extensively in chapter 4.2.2.

Table 2.2: Charging-induced resistance variations ΔR reported in the literature for different carbon materials.

First Author	**Year**	**Carbon Material**	ΔR [%]
Kastening [79]	1994	particles	400
Kazaoui [80]	2001	nanotube films	70
Barisci [81]	2003	nanotube paper	40
Barisci [82]	2004	nanotube paper	30
Pollak [83]	2006	porous films	12
Ruch [84]	2009	nanotube paper	80
Biener [85]	2012	porous, amorphous	150

In the context of this summary of literature reports on resistance tuning, also the research field of 'resistive switching' should be mentioned briefly. The concept of this method is the electrochemical formation of a conductive channel between two electrodes immersed in an electrolyte, which can be deposited or dissolved depending on the desired switching state. In such a way conductance changes of several orders of magnitude can be achieved reversibly. Resistive switching represents a very active research field with many technology-relevant applications. Since however the achievable conductance variations, even though generated electrochemically, arise from strongly different effects than the charging-induced resistance tuning investigated in this thesis, a detailed discussion of resistive switching goes beyond the scope of this introductory chapter. For more information about the topic of resistive switching the reader is referred to the review articles listed under references [86–88] in this thesis.

Charging Induced Actuation

Prior to resistance tuning the concept of Gleiter [22] was applied to generate charging-induced actuation. In a study published in 2003 by Weißmüller et al., a compacted platinum nanopowder pellet exhibited a reversible expansion of about 0.15 % upon cyclic voltammetry in aqueous KOH solution [23]. Follow−up studies were performed on platinum [62] and palladium [89] nanopowders in different chemical regimes, inducing actuation up to 0.24 % in

the oxygen regime [62] or up to more than 0.4 % upon hydrogen absorption in palladium [89].

The first actuation application of a dealloyed metal was published in 2003 [90]. In this study by Kramer et al. the electrochemically induced volume changes were made visible for the naked eye via macroscopic bending of nanoporous gold cantilevers. Until today, nanoporous gold by far represents the most intensively studied system with regards to tunable mechanical properties. Among a variety of studies ranging from tunable strength [27] or imbibition [91] to piezoelectric effects [92], a detailed work published by H.-J. Jin in 2008 [46], investigating the actuation behavior of nanoporous gold in different electrochemical regimes, is of particular relevance for the present thesis. Moreover a well-arranged review about (electro-)chemically induced volume changes of dealloyed metals is given in reference [26].

Giving a brief summary, the reason for electrochemical actuation can be found in variations of the surface stress, which arise because charging modifies the atomic bonding forces at the metal surface. In contrast to a semiconductor, a charging-induced electric field can penetrate only a few surface layers of a metal, while the interior remains field-free. Within the metal surface layers affected by charging however, significant amounts of (positive or negatvie) charge, up to several ten percents of an elemetary charge per surface atom, can be hosted, which causes high local space-charge densities [26]. It can be shown computationally (DFT), that such a charging significantly modifies the atomic bonding forces of the surface, leading to changes in the surface stress f and in further consequence to volume strain [93], which is illustrated in figure 2.4. The electrochemically induced variation of the surface stress, which is assumed to be isotropic in the surface plane, is characterized by the surface-stress charge coefficient ζ with

$$\zeta = \frac{\partial f}{\partial q}. \tag{2.3}$$

For a clean metal surface ζ exhibits a negative sign in the double layer regime. Thus metals expand upon positive surface charging, which is shown in references [62] and [46] for compacted platinum nanopowder and dealloyed gold respectively. Upon adsorption of

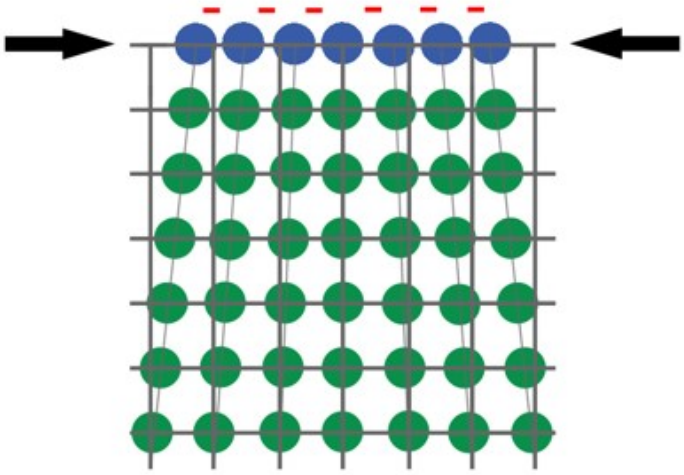

Figure 2.4: Schematic illustration of increasing surface stress due to imposing negative charge (red) on a metal surface (blue). The electrochemical treatment leads to a volume contraction of several surface atomic layers (blue and green), compared to the ideal lattice (grey grid).

oxygen as well as hydrogen, an expansion is reported, irrespective of the charge sign of the adsorbing species leading to $\zeta < 0$ for OH^- and $\zeta > 0$ for H^+ adsorption. The sample volume variations in these chemical regimes are much higher than those achieved upon double layer charging. Since this strong actuation is however associated with a large charge transfer from/to the electrode, the resulting surface-stress charge coefficients are significantly lower in the chemical regime [62].

A peculiarity is reported for nanoporous gold, covered by the so called primary oxide, that develops as a byproduct of the dealloying process [46]. Upon pseudocapacitive 'double layer like' charging of samples in such an oxidized condition, the surface-stress charge coefficient exhibits an opposed sign compared to the clean metal surface: The samples expand upon charging with excess electrons. This behavior is interpreted as most probably being caused by the less effective screening and therefore deeper penetration of the excess charge in the oxidized material. If band bending results in a location of the Fermi energy close to the valence band near the surface, the excess electrons will populate antibonding valence band states rather than bonding conduction band states. This weakening of the bonding between atoms would cause an expansion of the sample.

Besides gold, also other dealloyed materials with actuator properties are known in the literature, for example nanoporous silver [94] or nickel [95]. An extraordinary high reversible expansion up to 1.3 % was reported for nanoporous $Au_{0.8}Pt_{0.2}$ alloys [78], which are dealloyed from Ag-Au-Pt master alloys [56]. Due to the presence of the high melting platinum in this ternary alloy system, the structural rearrangement of the nanoporous network during the etching process is inhibited compared to conventional Ag-Au dealloying, resulting in finer porosities and a higher surface-to-volume ratio of the produced material [56], which in further consequence leads to an enhanced actuation behavior [78].

Dilatometry can also be used for the characterization of hydrogen absorption into the bulk of a solid. A frequently used model system for this purpose is Pd-H, which is introduced in chapter 2.4. In the field of dealloyed, nanoporous metals, acutation upon hydrogen absorption represents a very new, emerging research topic. The few works available in the literature [96,97] will be discussed in relation to the present results (published in reference [31]) in chapter 5.4.

2.4 Hydrogen Absorption in Palladium

The ability of hydrogen uptake into the bulk metal volume was discovered in the mid-nineteenth century for palladium by T. Graham [98] and has been in the focus of active research ever since. In various experimental and theoretical studies H absorption from the gas phase [99, 100] as well as by electrochemical methods [101] was investigated.

At room temperature two different phases of the Pd-H system may exist: the α-phase, a solid solution of H in Pd, and the β-phase, Pd hydride. The presence of the phases depends on the amount of hydrogen incorporated in palladium. At very low concentrations up to an atomic ratio H/Pd $\approx$ 2 % only the α-phase is present in the Pd-H system. When the hydrogen concentration is increased above this threshold, the wide regime of α-β coexistence is entered until at H/Pd ratios above 58 % Pd-H exists only in the β-phase. [102]. A phase diagram of the Pd-H system is sketched in figure 2.5.

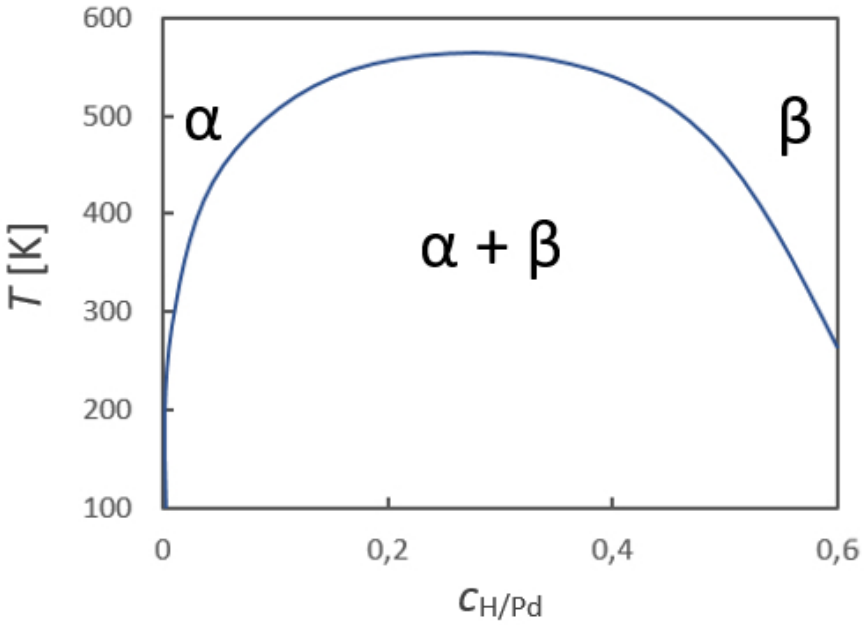

Figure 2.5: Sketch of the Pd-H binary phase diagram, according to reference [102].

Upon hydrogenation of Pd, which is illustrated in figure 2.6, a variety of physical properties of the host metal are altered. Among them, the sample's increase in electrical resistance [103, 104] as well as the volume expansion [105] with increasing H concentration will be of particular interest in the present work.

During the past few decades, particular research interest was placed on hydrogen absorption in micro- and nanostructured metals, including palladium, such as ultrafine−grained structures [106, 107], thin films [108] and most recently the already mentioned nanoporous palladium [30, 96, 97]. The available literature ranges from fundamental research questions to technological applications: For example, crystal lattice defects can be probed due to their influence on the hydrogen absorption characteristics [109, 110]. Moreover Pd nanostructures were shown to exhibit superior (faster) hydrogen uptake characteristics, advantageous for technological hydrogen storage [107].

Here it should be pointed out clearly, that Pd itself is not of direct relevance as a future hydrogen storage material. Besides of its high cost, being a precious metal, it also possesses a by far too high mass density, which rules out a reasonable applicability e.g. for mobile devices or as an on-board energy storage medium for vehicles. However due to the long history of

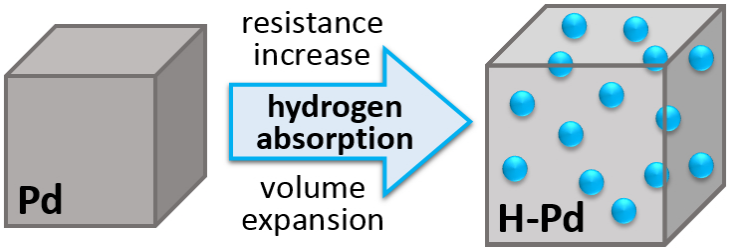

Figure 2.6: Schematic illustration of hydrogen uptake in palladium, which is associated with an increase in sample volume as well as electrical resistance.

studies on the hydrogen absorption in palladium with its well-understood characteristics, Pd is a popular and frequently used model system for studying the potentials of hydrogen uptake in novel systems such as the nanoporous structures investigated in this work.

3 | Experimental Methods and Sample Preparation

The key results obtained in the framework of this thesis are the generation and in situ monitoring of property variations of porous nanophase metals upon different electrochemical treatments. The methods applied to record these data will be presented in the following. A list of the samples used in this work is given in section 3.3.

3.1 Electrochemical Methods

All electrochemical measurements were recorded in three electrode geometry. The sample material, immersed in the electrolyte, was controlled as the working electrode (WE) of a potentiostat, which is sketched in figure 3.1. For resistometry experiments a Voltalab PGZ-100 (Radiometer Analytical) potentiostat was used, dilatometry experiments were conducted with an Autolab PGSTAT204 (Metrohm) potentiostat.

The potential of the working electrodes was measured relative to commercial reference electrodes (REF), purchased from the manufacturer of the potentiostat used for the respective measurement. Besides dealloying experiments of nanoporous gold, all used reference electrodes were conventional Ag/AgCl systems, based on the half cell reaction

$$Ag_{(s)} + Cl^-_{(aq)} \leftrightarrow AgCl_{(s)} + e^-$$

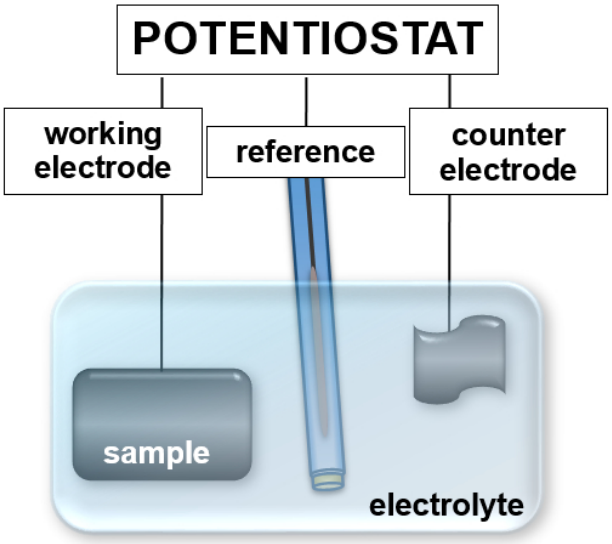

Figure 3.1: Schematic cell setup for electrochemical measurements in three electrode geometry.

and filled with a saturated (Radiometer Analytical) or 3.5 mol/l (Metrohm) aqueous solution of KCl, which exhibit potentials of +197 mV (saturated) or +205 mV (3.5 mol/l) relative to the standard hydrogen electrode. For np-Au dealloying in $AgNO_3$ electrolyte, a double junction reference electrode (Metrohm) with KNO_3 as salt bridge (outer chamber) had to be used in order to avoid AgCl precipitation in the measurement cell. When referring to the potential of the samples, $U_{Ag/AgCl}$ will be given relative to the respective reference electrode in the following.

The potential recorded between the working and the reference electrode without external charging is called open circuit potential (OCP). If a potential of the WE other than the OCP is to be adjusted, a third electrode, the counter electrode (CE), is required since currents between the sample and the reference electrode are undesirable. For the property tuning experiments (chapter 4.2), counter electrodes with sufficiently high electrochemically active surfaces were required, which was provided by sheets of highly porous carbon fabric. As counter electrodes for dealloying, graphite sheets (np-Au) or wires of platinum (np-Pt) or palladium (np-Pd) were used.

The electrochemical methods used to obtain the majority of the results in this work are

cyclic voltammetry and chronoamperometry. These methods will be briefly introduced in the following with Pt in an aqueous solution as examplary working electrode, representing one of the most intensively studied electrochemical systems. While the sample potential is varied in a defined manner the concommitant current flowing to/from the samples is recorded. Charge transfers are determined by integration with the simple trapezoid method, using the potentiostatic data as corner points.

Cyclic Voltammetry

During cyclic voltammetry (CV) the potential of the working electrode is varied in triangular characteristics with a constant scan rate

$$\left|\frac{\mathrm{d}U}{\mathrm{d}t}\right| = const. \tag{3.1}$$

between an upper and a lower limit. This method gives an overview of the electrochemical behavior of the studied material as a function of U, allowing to distinguish between double layer and chemically active regimes. An exemplary cyclic voltammogram, recorded for a compacted pellet of commercial Platinum Black in a 1 mol/l aqueous solution of KOH is shown in figure 3.1. While the potential is varied with a scan rate of 1 mV/s between the lower limit -1000 mV and the upper limit $+450$ mV, both stated versus the Ag/AgCl reference electrode, the recorded current curve is run through in clockwise direction.

We start the discussion in the double layer region (marked yellow) of the upper branch, characterized by a rather low current flow. As the potential is scanned towards more positive values, a strong increase in current occurs when the regime of oxygen adsorption is reached (marked red). Near the upper potential limit a slight increase in curvature is visible in the current-curve, indicating the onset of oxygen evolution from the electrolyte associated with bubbles emerging from the electrolyte, which was preferably avoided during the property tuning experiments in this thesis.

When the scanning direction is reversed at $U_{Ag/AgCl} = +450$ mV we enter the lower

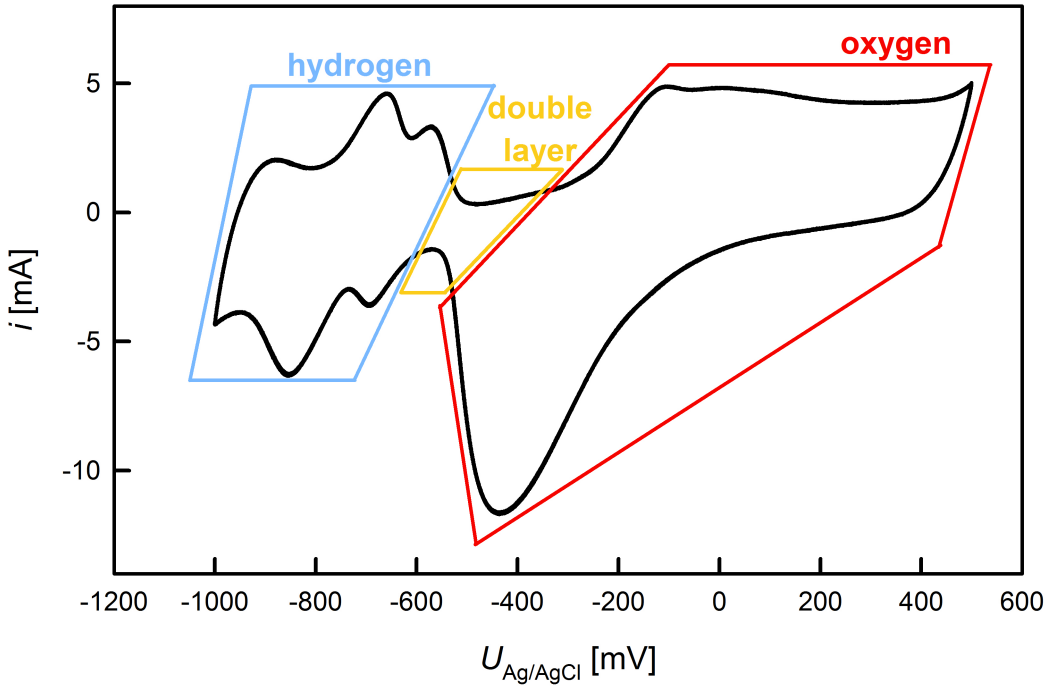

Figure 3.2: Exemplary cyclic voltammogram of compacted Platinum Black powder (commercial) in 1 mol/l KOH aqueous solution, recorded with a scan rate of 1 mV/s at potentials $U_{Ag/AgCl}$ between -1000 mV and $+450$ mV. While the sample potential is varied with triangular characteristics, the current curve is run through in clockwise direction. Different chemical regimes are marked: double layer (yellow), oxygen ad-/desorption (red), hydrogen ad-/desorption (blue).

branch of the CV. The adsorbed oxygen remains stable on the sample surface in a certain potential range, associated with low currents, until oxygen is desorbed in a prominent peak with a maximum at about -450 mV. Following the oxygen desorption peak, again low double layer currents are visible in a narrow potential range (yellow), before the scan reaches the hydrogen regime marked in blue. Here hydrogen ad-/desorption takes place in several current peaks, representing the main low index crystallographic planes offering differently attractive adsorption sites for the small hydrogen atoms [111], finally approaching again the regime of gas evolution near the lower potential limit.

In order to achieve reproducable electrochemical results, a working electrode is usually activated by repeated CV cycling prior to an actual measurement. The activation is per-

formed until stable conditions of a steady state are achieved which is the case when successive cycles can no longer be discerned.

Even though no exemplary cyclic voltammograms are shown in this section for the other porous nanophase metals investigated in this thesis (Au, Pd), the peculiarities of these systems with regards to the hydrogen regime should be mentioned here briefly: While no hydrogen adsorption prior to H_2 gas evolution can be observed for gold, resulting in an extended potential range of double layer charging, palladium's ability to absorb hydrogen into the bulk results in enhanced currents in this regime, compared to Pt (see below, figures 4.32 and 4.26).

Since during a cyclic voltammetry scan the ions tend to adsorb in registry with the surface atoms, the recorded charge transfer can be used to determine the electrochemically active surface area of a sample material. In the case of Pt, one complete scan as shown in figure 3.1 is associated with the ad- and desorption of one monolayer of hydrogen, corresponding to a charge transfer of 210 $\mu C/cm^2$ for polycrystalline Pt as an average value over all relevant low index crystal faces [112].

For the platinum samples studied in this thesis, the determination of the active electrode surface areas was performed using the charge flow recorded upon hydrogen desorption, which had to be corrected for the double layer current. As double layer current the lowest current value recorded in the double layer regime (upper branch of the CV) is taken, which is assumed to give a constant contribution throughout the entire potential scan. This double layer contribution is subtracted from the CV curve before integration by the trapezoid method as described above in this chapter.

Chronoamperometry

In chronoamperometry mode (CA) the potential of the working electrode (sample) is set to a constant value. The current i is recorded while the sample approaches an equilibrium state. The current characteristics of a CA step show an approximately exponential behavior,

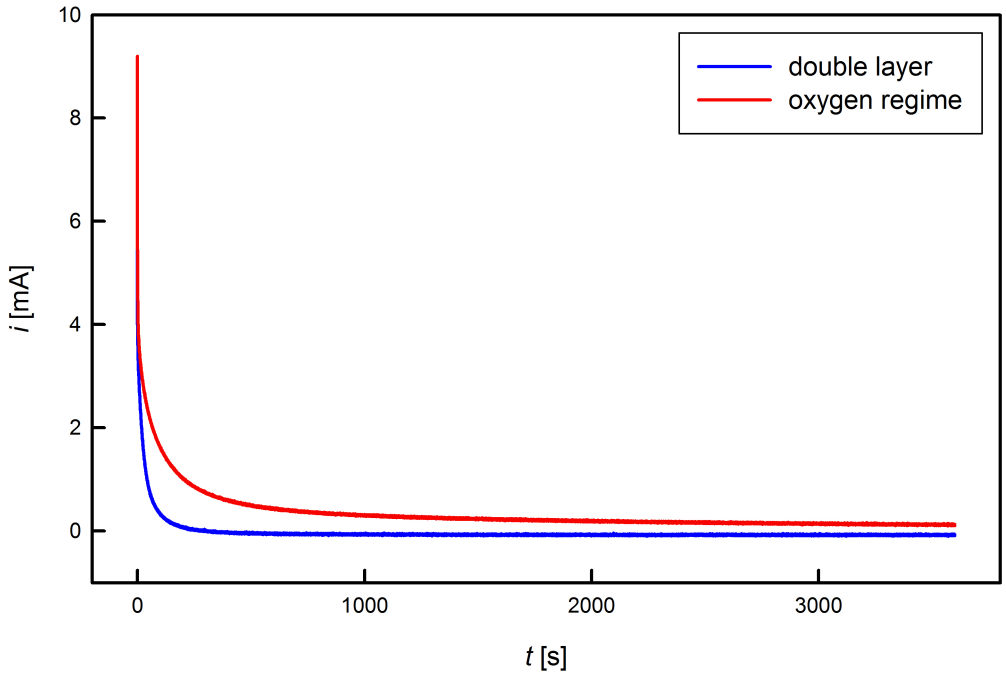

Figure 3.3: Exemplary chronoamperometric charging curves of nanoporous Platinum in different chemical regimes. Double layer charging (blue) occurs fast and with small leakage currents, while the oxygen regime (red) is associated with higher time constants and leakages.

comparable to the charging current of a capacitor.

Different chemical regimes can clearly be distinguished by the time constants of charging, which is illustrated in figure 3.3 for nanoporous platinum produced by dealloying. In the double layer regime (blue), which is characterized by shifts in the charge carrier density with no charge penetrating the interface similar to an electrical capacitor, the charging current rapidly decays, whereas in the oxygen regime (red), associated with chemical reactions at the solid-electrolyte interface with a concomitant charge exchange, longer charging times and higher currents are recorded.

One major advantage of chronoamperometric measurements is the correction of leakage currents. In contrast to the theoretically expected exponential decay of the charging current towards zero, experimentally a leakage rather than zero current is reached finally, regardless of the sample, charging time or potential used. Such a leakage current, which is caused

by chemical electrode reactions and/or electrolysis, is present also in other electrochemical methods, such as CV, however superimposed to the (usually higher) measurement current.

Since this leakage current does not contribute to the charge transfer associated with the investigated process, it should be subtracted from the recorded signal for an accurate charge determination. In an idealized correction for a measurement with the duration t_{max}, the transferred charge

$$Q_{ideal} = \int_0^{t_{max}} \left(i(t) - \lim_{t \to \infty} i \right) dt \tag{3.2}$$

is determined by subtracting the leakage limiting value for extended times from the recorded current before integration. In practice a CA measurement is stopped after a measurement time t_{max}, when the current signal i has faded to a flat line, exhibiting variations only due to noise. The average value $\overline{i_{Leak}}$, recorded for the current at times t between $0.9 \cdot t_{max}$ and t_{max}, is assigned to leakages . The corrected charge Q is then calculated as

$$Q_{ideal} = \int_0^{t_{max}} \left(i(t) - \overline{i_{Leak}} \right) dt. \tag{3.3}$$

Dealloying

The preparation of nanoporous metals by electrochemical dealloying represents a special application of chronoamperometry in which a master alloy with a dilute concentration of the more noble component(s) is used as the working electrode. The alloy is held at an anodic potential, suitable to selectively dissolve the less noble component(s), which results in a nanoporous structure of the more noble element(s).

An exemplary dealloying curve recorded for a $Cu_{75}Pt_{25}$ master alloy platelet is presented in figure 3.4. The etching experiment was performed in a 1 mol/l aqueous solution of H_2SO_4 at a potential $U_{Ag/AgCl}$=+1075 mV. The recorded curve shows peculiar characteristics that significantly differ from the CA curves shown above: At the beginning of the etching experiment the current increases and reaches a maximum, here at about t=3000 s, before

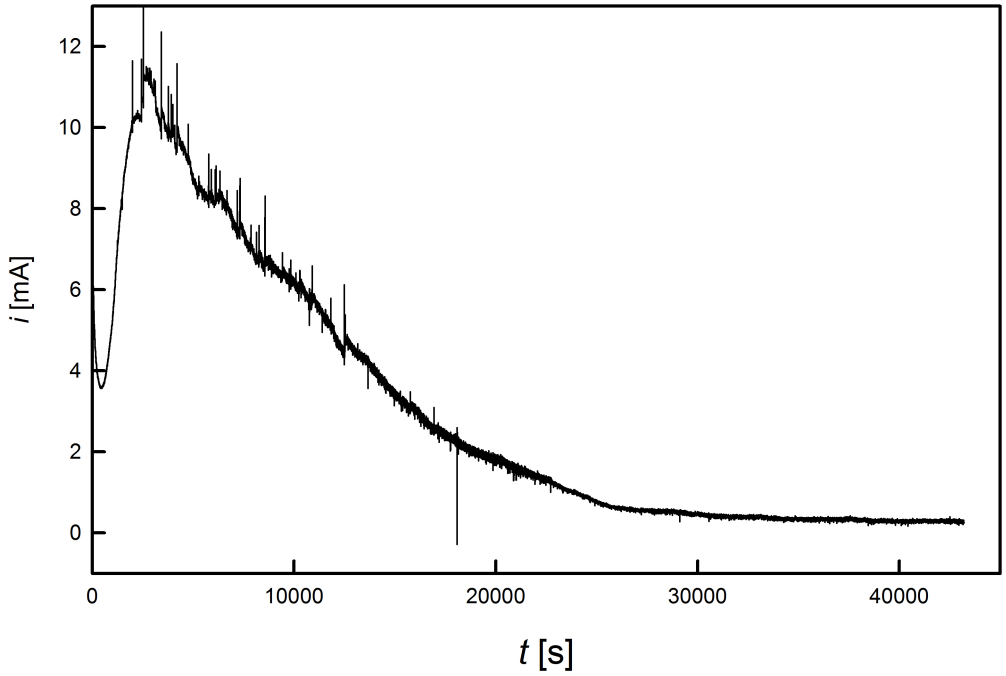

Figure 3.4: Dealloying curve recorded for a $Cu_{75}Pt_{25}$ master alloy platelet in 1 mol/l H_2SO_4 at a potential $U_{Ag/AgCl}$=+1075 mV.

it shows the typical decay of a CA curve. This behavior is recorded since two concurring processes influence the charge flow during a dealloying experiment. While the sample is depleted of the sacrificial element (here Cu) the active surface area of the sample rapidly grows as nanoporosity evolves. At early stages of the dealloying experiment the latter effect is dominant which leads to an increasing current. Later the depletion of Cu prevails, causing the current to decay until it finally fades out at values well below 1 mA.

The dealloying parameters such as electrolyte(-concentration) and applied potential have to be chosen appropriately for each master alloy system in order to avoid severe damages of the sample (cracking) or passivation during dealloying. A stagnation of the etching process can occur due to oxidation or due to a rearrangement of the more noble atoms resulting in a dense layer of the more noble element covering the sample surface with a substantial amount of the sacrificial element, or even a remaining master alloy backbone, buried beneath.

In the framework of this thesis, nanoporous (np) gold, platinum and palladium produced

by dealloying were investigated. The Ag-Au and Cu-Pt master alloys for np-Au and np-Pt were obtained from the Hamburg-Harburg University of Technology where they were prepared by arc melting. The Co-Pd master alloy for np-Pd was prepared by electron beam melting (EBM) at the TU Graz Institute of Materials Science and Welding.

The first set of nanoporous platinum samples investigated during this work, denoted as samples np-Pt R3-R5, were dealloyed by Prof. Stephan Landgraf at the TU Graz Institute of Physical and Theoretical Chemistry. All other samples presented in this thesis were etched directly at our institute (see table 3.1 below).

For the resistometric investigations (chapter 4.1) and modeling of dealloying (chapter 5.1), special demands had to be put on the etching process. Since in the proposed model the recorded resistance variation is expressed as a function of transferred charge, a reliable charge determination is crucial. Therefore the choice of dealloying systems was restricted to those, where no free corrosion takes place at open circuit potential, which unfortunately does not apply to the most common etching procedure in the literature, namely dealloying of Ag-Au in nitric acid [4]. In the present work, following reference [48], dealloying of Ag-Au was performed in neutral silver nitrate solution, where no electroless current component is observed. Nanoporous platinum and palladium were produced by dealloying Cu-Pt and Co-Pd master alloys in sulphuric acid solutions. A detailed collection of the applied dealloying parameters is given below in table 4.1.

3.2 Property Tuning

The property tuning experiments performed in this thesis cover electrochemically induced variations of the electrical resistance as well as the volume expansion of porous nanophase metals. The resistometric measurements include samples produced by dealloying as well as by compaction of metallic nanopowders, whereas the dilatometric experiments were limited to dealloyed samples. The applied setups with their respective requirements and constraints will be presented in the following.

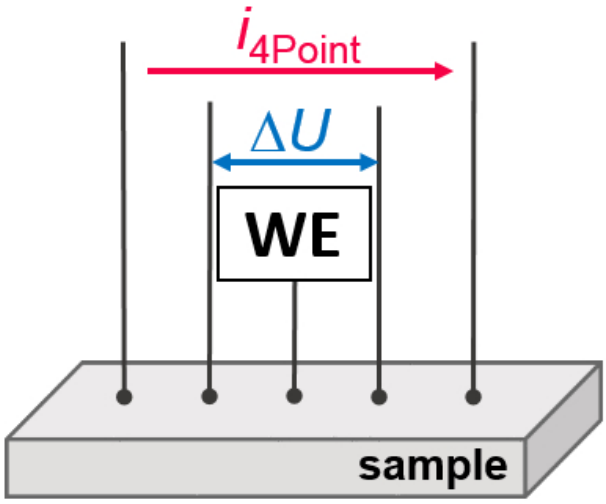

Figure 3.5: Schematic setup of a four point resistance measurement of a nanoporous sample. Five contact wires are attached to the sample, the middle one serves as working electrode contact of the potentiostat. The remaining four wires are used for four point resistometry, the outermost two wires supply the four point measuring current while the remaining two wires sense the voltage drop.

Resistometry

All resistometric measurements presented in this thesis were performed in four point geometry, by means of which contact resistances between the sample materials and the attached wires are eliminated from the measurement results. The different material types required different setups, which will be presented in detail below. In all cases, however, five electrode contacts were attached to the sample surface in line as shown schematically in figure 3.5. The mid-positioned wire served as working electrode contact to the Voltalab PGZ-100 (Radiometer Analytical) potentiostat, the other wires were connected to a Keithley 2400 Source Meter for the four point measurements. The outermost wires connected to the sample were used for the current supply, as indicated by i_{4point} in figure 3.5, the voltage drop ΔU was sensed between the remaining two wires.

The four point current was applied in pulsed mode with a period of approximately 2.5 seconds. For accurate resistance measurements during electrochemical charging the four point current pulses have to be chosen sufficiently high, in the present case i_{4point}=100 mA

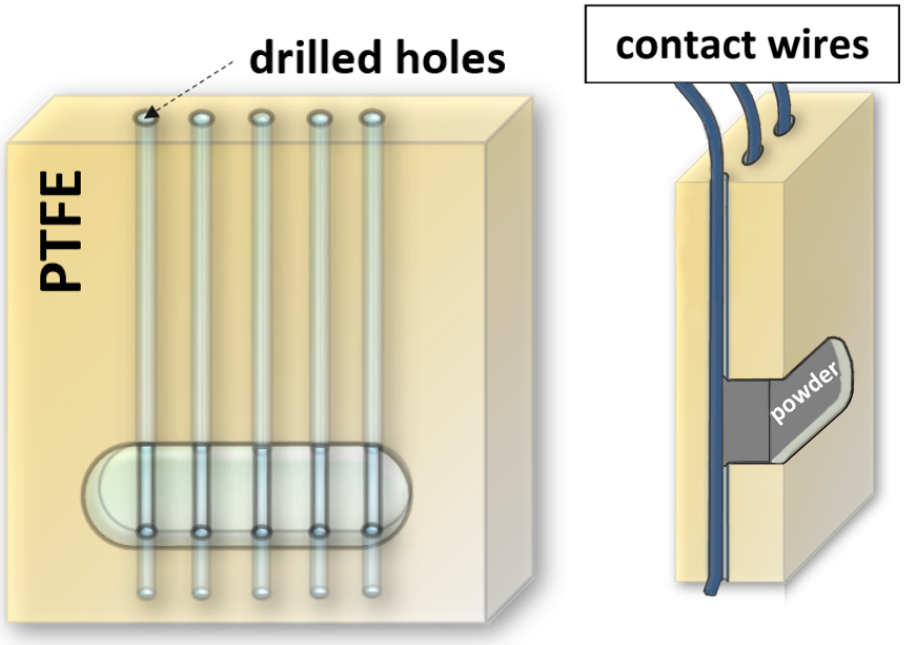

Figure 3.6: Sketch of a PTFE groove, used for the compacted nanopowder pellet samples nc-Pt and nc-Pd in empty (left) and filled (right) condition.

was used. This causes certain irregularities visible as spikes in the otherwise smooth cyclic voltammograms (e.g. see figure 4.10), whenever potentiostatic and resistometric measurement points coincide. An influence of the potentiostatic charging current on the resistance measurements was however thoroughly excluded by means of comparative CA measurements, which will be presented in detail below (see figure 4.11). When the charge transfers were determined by a trapezoid integration of CV curves, the spikes caused by the current pulses were corrected by a linear approximation, which will be shown in chapter 4.2 (e.g. see figure 4.13).

For the compacted nanopowder samples commercial Platinum Black, purchased from ChemPur with a nominal specific surface area of 20−40 m^2/g (sample nc-Pt), and palladium nanopowder, produced by inert gas condensation (sample nc-Pd) were used. The measurement setup was based on earlier measurements by Martin Sagmeister et al. [24]: The nanopowder was compacted into a groove in a Teflon (PTFE) specimen holder, as sketched in figure 3.6. The specimen holders were manufactured in the TUG Physics Workshop out

of prism-shaped PTFE-pieces sized initially about 12 × 12 × 5 mm^3. Into these PTFE pieces, grooves with a depth of about 3 mm were cut, sized 9.5 × 2.5 mm^2 with rounded edges, fitting an available anvil. Holes with a diameter of 0.5 mm were drilled through these specimen holders, to embed platinum wires serving as electrical contacts. After inserting the wires, the nanopowders were filled into the grooves and compacted carefully with an anvil, using a hand vise. The masses of the nanoporous pellets produced in this manner are listed in table 3.6.

In the present work, the sample geometry was improved by the addition of a fifth wire, compared to the earlier setup where only four wires were embedded in the PTFE groove. In the setup used earlier, one of the inner two wires was used both as working electrode contact as well as for sensing the four point voltage drop ΔU, which caused severe interferences and therefore limited the measurements to CA mode, where the resistometric data points could be only taken when the charging currents had faded. By adding a fifth wire, the potentiostatic charging and four point sensing could be attached to separate contacts, allowing for dynamic measurements of property tuning and especially expanding the experiments to the important electrochemical method of cyclic voltammetry by which most of the experiments presented below were recorded (see chapter 4.2).

For the dealloyed samples, two different setups were employed to monitor the resistance variations upon electrochemical charging. In early stages of this thesis, as mentioned above, the dealloying of $Cu_{75}Pt_{25}$ was conducted by Prof. Stephan Landgraf at the TU Graz Institute of Physical and Theoretical Chemistry (samples np-Pt R3-R5, see table 3.1). The resistance tuning measurements were performed on loose platelets after dealloying, which required extraordinarily cautious handling due to the extreme brittleness of the nanoporous metals and lead to a mechanical failure of several samples during preliminary testing. The contacting method used for these platelets is sketched in figure 3.7A. The np-Pt platelets were laid on the bottom of a Petri dish and contacted from above by five Pt wire springs of separately adjustable lengths, guided towards the sample surface through thin glass pipes.

In this geometry, denoted as 'lying, springs' in table 3.1, the primary oxide condition

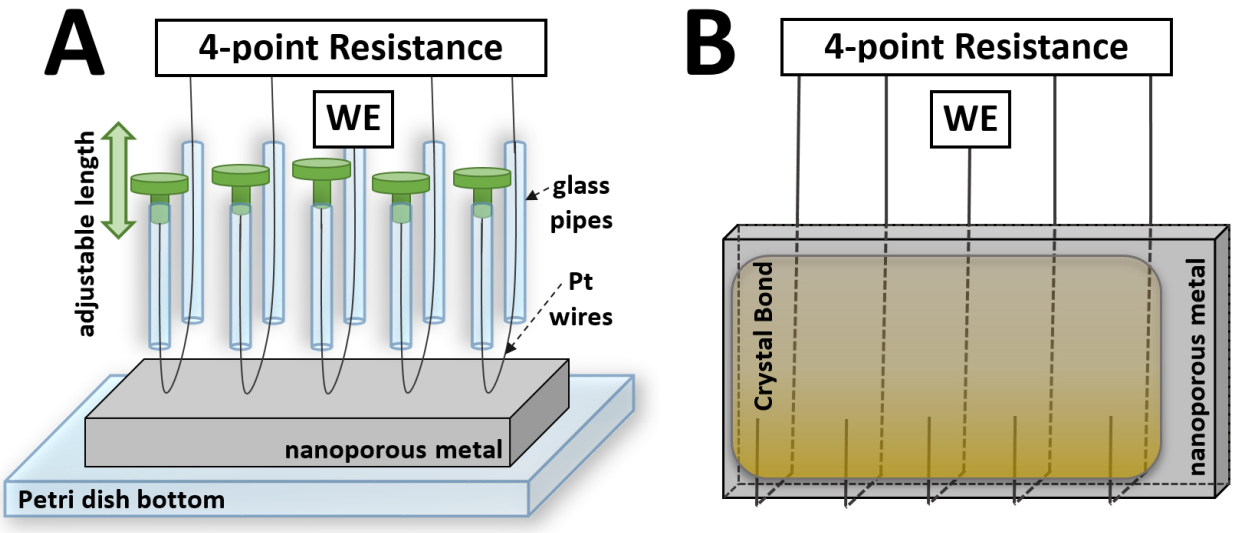

Figure 3.7: Resistometry setups for nanoporous samples produced by dealloying. A: Contacts attached after dealloying (samples np-Pt R3-R5) by placing five adjustable Pt wire springs on the surface of the lying sample. B: Contacts attached prior to any electrochemical treatment by clenching five well annealed wires around the sample platelet and immersing the hanging sample into the electrolyte.

of freshly dealloyed platinum samples with its characteristic sign inversion could be investigated, however, reducing the samples lead to severe sample damages and/or contact losses. Therefore, a different setup was required for investigations of the metallic state of nanoporous platinum. This could be realised by moving the dealloying process into our own laboratory and attaching the required contacts to the sample prior to any electrochemical treatment.

In this improved setup, denoted as 'hanging' in table 3.1, five well annealed, flattened wires, consisting of the more noble element of the master alloy, were clenched around the master alloy in line, as sketched in figure 3.7B. Connecting the samples in such a way provided a sufficient electrical contact for all measurements on ductile gold. For nanoporous platinum and palladium, the wires had to be fixed additionally by a droplet of glue (Crystal Bond 509, Aremco), covering one face of the alloy stripe as shown in the image. This bonding layer provided both an enhanced electrical contact as well as a certain mechanical stabilization of the brittle material. To set up the electrochemical cell, the sample was immersed into the electrolyte while hanging on the wires, by which any mechanical constraints on the sample were minimized.

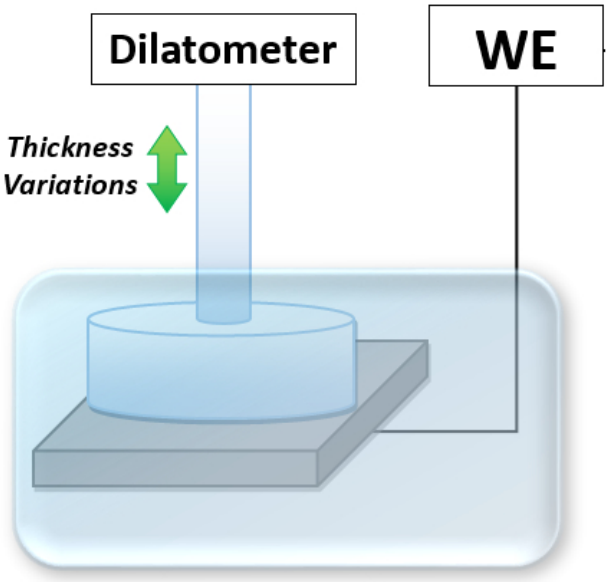

Figure 3.8: Experimental setup for monitoring the actuation behavior of nanoporous samples in a Linseis LV75 vertical dilatometer. The sample platelet is placed under the dilatometer's pushrod and contacted to the potentiostat from below using a flattened, well annealed wire.

Dilatometry

For the dilatometric measurements a Linseis LV75 vertical dilatometer was adjusted for operating with an electrochemical cell in the framework of this thesis. In the used setup, which is sketched in figure 3.8, a square shaped sample platelet with dimensions of approximately 5×5 mm^2 is placed under the dilatometer's pushrod, which applies a constant pressure of 100 mN. The sample is contacted from below by a well annealed, flattened wire, consisting of the more noble element present in the master alloy, which serves as working electrode contact to an Autolab PGSTAT204 potentiostat (Metrohm). Like in the improved resistometry setup, again all connections are set up prior to any electrochemical treatment and a minimum of mechanical manipulations is performed once a sample platelet is dealloyed. During the following experiments the electrical contact as well as the brittle sample are stabilized by the slight constant pressure of the pushrod.

For electrochemical measurements the entire sample platform can be immersed into a beaker filled with electrolyte, which can be raised from below using a laboratory scissor jack.

The accuracy of the dilatometric measurements recorded in this setup is limited by room temperature variations rather than by the inherent resolution of the measuring device, which is, for example, clearly visible by an oscillation overlaying the length change curve shown in figure 4.12. This limiation makes quantitative evaluations of the actuation behavior difficult, particularly upon double layer(-like) charging where the variations are very small (see figures 4.14 and 4.18). The quality of future measurements is expected to be enhanced significantly by a new improved air conditioning system, which is presently beeing installed in the dilatometry laboratory.

3.3 List of Samples

An overview of all samples included in this thesis is given in table 3.1. The compacted nanopowder samples, which were produced as described in section 3.2, are represented by one pellet for each of the elements (Pt and Pd), denoted by the prefix 'nc' (samples nc-Pt and nc-Pd). For the dealloyed nanoporous metals, which were used in the majority of experiments in this work, a set of platelets is presented under the prefix 'np'. Samples used for resistometry/dilatometry are tagged by the notation R/D respectively.

During preliminary testing numerous nanoporous metal samples were used. For the purpose of clarity and comprehensibility the measurements presented in the following chapter 4 were however limited to a minimum number of samples necessary to exemplarily show the most essential results.

Table 3.1: List of samples used in this thesis.

Compacted Nanopowders				
Name	**Material**	**Mass m**	**Contacting Method**	**Figures**
nc-Pt	commercial Pt Black	104 mg	PTFE groove	4.3, 4.4, 4.5, 4.6, 4.7, 4.8, 4.9, 5.5
nc-Pd	inert gas condensation	90 mg	PTFE groove	4.30
Dealloyed Platelets				
Name	**Master Alloy**	**Initial Mass m_0**	**Contacting Method**	**Figures**
np-Au R1	$Ag_{73}Au_{27}$	86 mg	hanging, free	4.1, 4.31, 4.32, 5.2, 5.2, 5.4
np-Pt R1	$Cu_{75}Pt_{25}$	52 mg	hanging, glued	4.2, 5.4
np-Pt R2	$Cu_{75}Pt_{25}$	163 mg	hanging, glued	4.10, 4.11, 4.13, 4.15, 4.16, 4.17, 4.24, 5.5
np-Pt R3	$Cu_{75}Pt_{25}$	132 mg	lying, springs	4.19
np-Pt R4	$Cu_{75}Pt_{25}$	97 mg	lying, springs	4.20, 4.22
np-Pt R5	$Cu_{75}Pt_{25}$	116 mg	lying, springs	4.21, 4.23
np-Pt D1	$Cu_{75}Pt_{25}$	30 mg	dilatometer	4.12, 4.14, 4.18, 4.25
np-Pd R1	$Co_{88}Pd_{12}$	84 mg	hanging, glued	4.2, 5.4
np-Pd R2	$Co_{88}Pd_{12}$	100 mg	hanging, glued	4.26, 4.27
np-Pd D1	$Co_{88}Pd_{12}$	87 mg	dilatometer	4.26, 4.28
np-Pd D2	$Co_{88}Pd_{12}$	58 mg	dilatometer	4.27
np-Pd D3	$Co_{88}Pd_{12}$	43 mg	dilatometer	4.29

4 | Experimental Results

The key results obtained in the framework of this thesis can roughly be divided in two major topics: on the one hand studies of the dealloying process itself, which will be presented in section 4.1, and on the other hand property-tuning experiments for different nanoporous metals obtained by dealloying as well as for reference materials produced by compacting nanopowders, collected in section 4.2. Section 4.3 is a collection of further results for dealloyed samples, obtained during this thesis by techniques other than resistometry and dilatometry. Besides detailed morphological characterizations by SEM and TEM, particular interest was laid on investigations of the primary oxide inherent to freshly dealloyed samples.

4.1 Resistometry during Dealloying

The system studied most intensively during this thesis with regards to the resistance increase upon dealloying was np-Au etched from an Ag-Au master alloy, which is also the most common dealloying-system in the literature [4]. All measurements on nanoporous gold included in this chapter were recorded and already presented in the framework of a master thesis conducted by Michael Seidl, which I had the pleasure to co-supervise during my dissertation. Figure 4.1 exemplarily shows a measurement for a $Ag_{73}Au_{27}$ platelet (np-Au R1), dealloyed in a 0.1 molar aqueous solution of silver nitrate ($AgNO_3$), which was chosen as the electrolyte in order to avoid free corrosion as described in chapter 3.1.

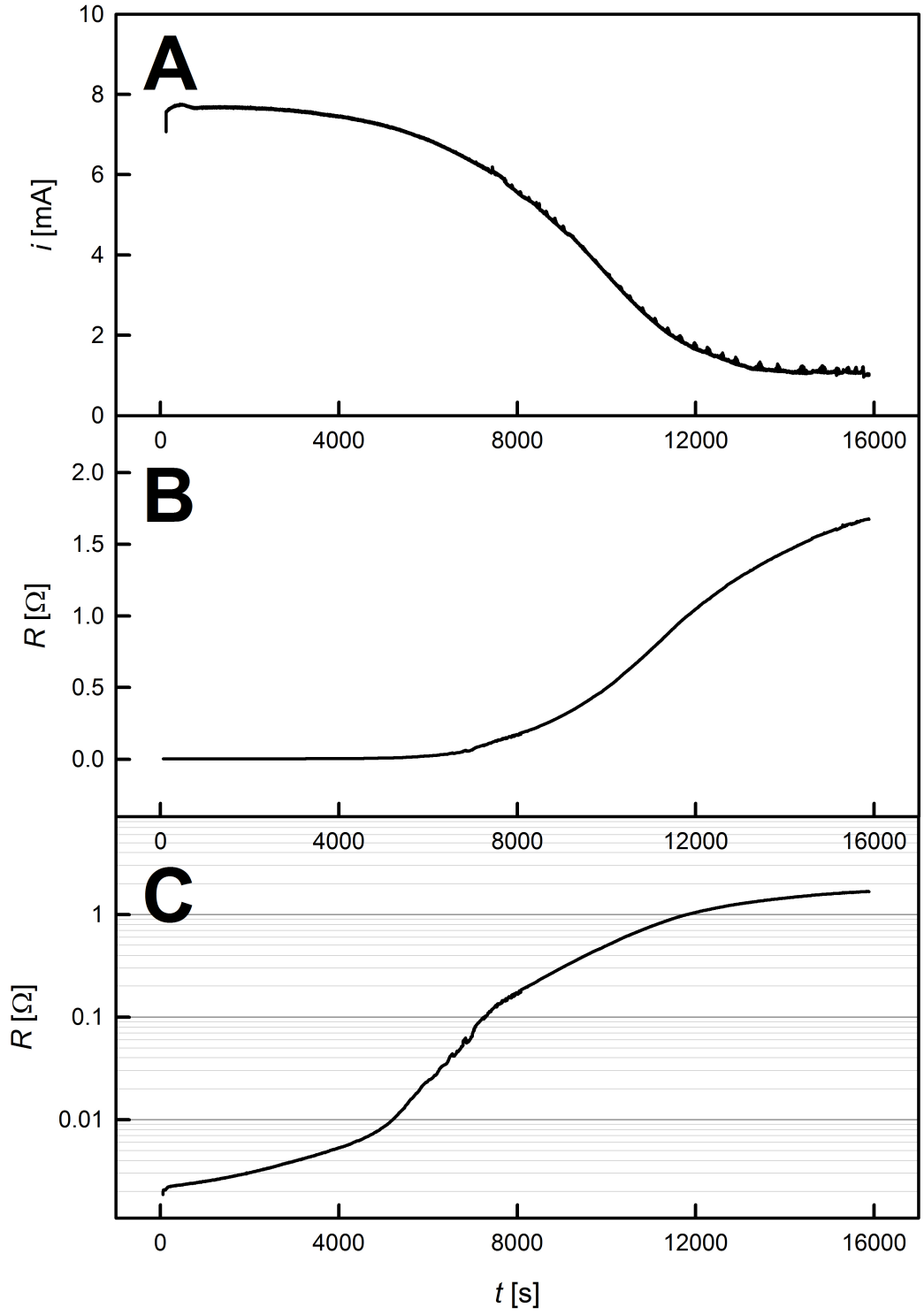

Figure 4.1: Current i recorded during dealloying a $Ag_{73}Au_{27}$ master alloy at $U_{Ag/AgCl}$ = +1300mV in 0.1 M $AgNO_3$ aqueous solution with the concomitant increase of the resistance R in linear (B) and logarithmic (C) scale.

	master alloy	m_0 [mg]	electrolyte	$U_{Ag/AgCl}$ [mV]	CE	Q_F [As]
np-Au R1	$Ag_{73}Au_{27}$	86	0.1 M $AgNO_3$	+1300	C	74
np-Pd R1	$Co_{88}Pd_{12}$	84	0.1 M H_2SO_4	+550	Pd	227
np-Pt R1	$Cu_{75}Pt_{25}$	52	1.0 M H_2SO_4	+1075	Pt	104

Table 4.1: Master alloy compositions, initial sample masses m_0, electrolytes, dealloying potentials $U_{Ag/AgCl}$ measured versus the Ag/AgCl reference (Radiometer Analytical), counter electrodes (CE) and recorded charge transfers Q_F for the dealloying experiments presented in this section.

The dealloying current i is plotted as a function of time in figure 4.1A, starting at values of about 8 mA and fading out when the sample is depleted of the sacrificial element Ag. For detailed dealloying parameters see table 4.1. Concomitantly to dissolving silver from the master alloy, which results in the desired nanoporosity, also oxygen is transferred to the sample during the dealloying experiment. Both processes are associated with a charge transfer of the same (positive) sign, which therefore in the measurement adds up to a total charge transfer Q_F, amounting to about 74 As in the present experiment. While the nanoporous structure is formed, the resistance of the sample (figure 4.1B) remains very low for a long time before it starts to increase strongly, in the present case at about $t = 8000$ s. The extent of this increase becomes better visible when the curve is plotted in log-scale as presented in figure 4.1C, showing the resistance rising by three orders of magnitude.

Similar measurements were also performed during the formation of nanoporous palladium and platinum, which is shown in figure 4.2. The dealloying parameters are also listed in table 4.1. As clearly visible in figure 4.2, the resistance curves are not as smooth as that recorded for nanoporous gold (figure 4.1). This indicates that, in spite of fixing the wires on the sample surface with glue as described in chapter 3, Pt and Pd show a higher proneness to contact issues due to their lower nobility and ductility, causing increased oxidation and mechanical disconnections. However, the observed resistance variations exhibit remarkable similarity for all metals, each showing a resistance increase by about three orders of magnitude.

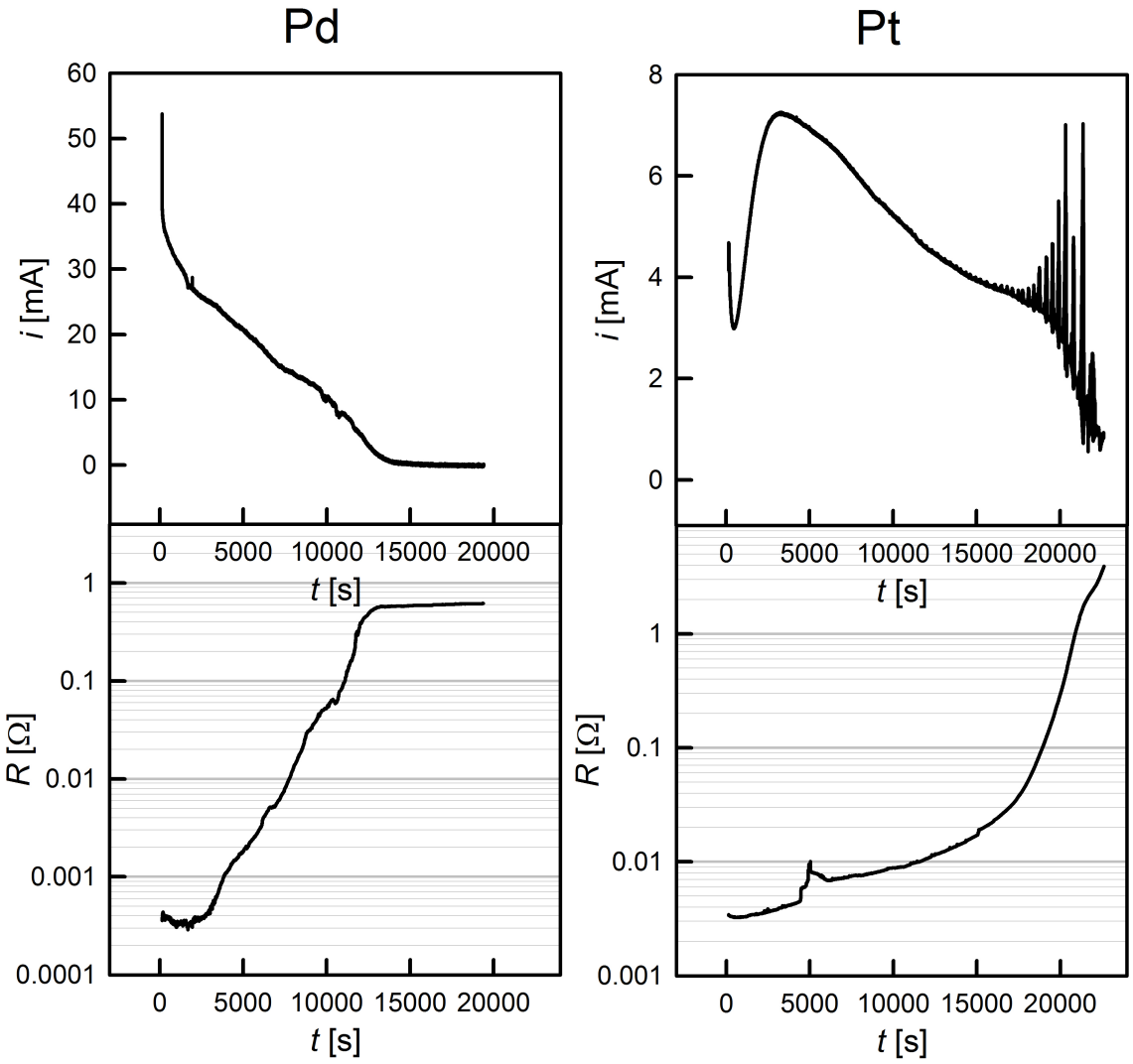

Figure 4.2: Dealloying currents i and concomitant increase of the resistances R recorded during the evolution of np-Pd (left) and np-Pt (right) by dealloying $Co_{88}Pd_{12}$ at $U_{Ag/AgCl} = +550$mV in 0.1 M H_2SO_4 and $Cu_{75}Pt_{25}$ at $U_{Ag/AgCl} = +1075$mV in 1 M H_2SO_4 respectively.

4.2 Tunable Properties

The focus of property tuning experiments in this thesis lies on electrochemically induced resistance variations of nanoporous metals produced by dealloying. The results are supported by dilatometry as well as by measurements on compacted nanopowder samples (section 4.2.1). The majority of experiments was conducted on nanoporous platinum, which is presented in section 4.2.2. In the subsequent sections 4.2.3 and 4.2.4 property tuning of nanoporous

palladium and gold is presented. Besides well-reduced (metallic) samples, also the peculiar behavior of freshly dealloyed samples, covered by the so-called primary oxide, is investigated for all mentioned nanoporous metals.

4.2.1 Platinum Black

The tunable properties of porous nanophase Pt will be introduced in this section, using as an example commercial Platinum Black, compacted into pellets, which will be referred to as nc-Pt in the following. The results obtained for this material were published in the Beilstein Journal of Nanotechnology, thematic series *Advances in Nanomaterials*, which is listed as reference [32]. Comparative measurements regarding the tunability of the magnetic moment of Platinum Black, which are presented in the mentioned article yet not included in this thesis, were performed by my colleague Stefan Topolovec. Even though confirmed by experiments with various samples, all measurements shown in this section were recorded for one 104 mg nanopowder pellet, compacted into a PTFE groove as described in section 3.2.

A typical cyclic voltammogram for Platinum Black, which will be referred to as overview in the following, is shown as grey curve in figure 4.3. The CV was recorded at potentials $U_{Ag/AgCl}$ between −1050 mV and +600 mV, limited by avoiding strong gas evolution. The surface area of the sample can be determined from the hydrogen desorption in the cyclic voltammogram as described in reference [112]: the desorption of one monolayer of hydrogen, as assumed to take place in the CV, is associated with a charge transfer of 210 μC/cm^2. Applied to the present sample this corresponds to an electrochemically active surface area of about 5 m^2/g.

The colored CV curves in figure 4.3 characterize the potential regions, which were investigated in detail with respect to charging-induced variations of the electrical resistance. These CVs are located in the double layer and oxygen-governed regime (above $U_{Ag/AgCl}$=−555 mV) and are shown in steady state. The pink curve shows a featureless double layer CV, recorded at potentials between −555 mV and −355 mV. The CV between −465 mV and −35 mV

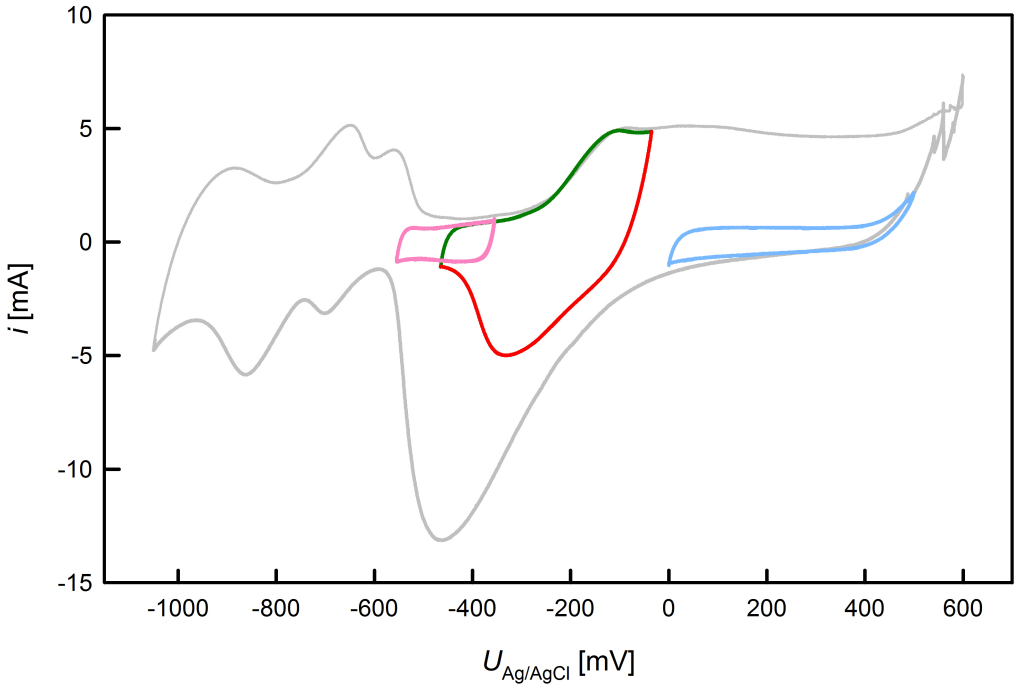

Figure 4.3: Steady state cyclic voltammograms of a compacted Platinum Black sample in 1 M KOH aqueous solution, recorded at a scan rate of 0.5 mV/s in different potential ranges from −1050 mV to +600 mV (overview, gray), −555 mV to -355 mV (double layer, pink), −465 mV to −35 mV (ad-/desorption, green/red) and 0 mV to +500 mV (oxidized, blue).

characterizes the formation (anodic direction, green line) and subsequent removal (cathodic direction, red line) of a thin oxygen layer to an extent of less than one oxygen atom per Pt surface atom [113]. The blue CV curve in the higher potential regime (0 mV to +500 mV) corresponds to the state of further strong oxygen adsorption.

The overview CV is plotted again as a red curve in figure 4.4, along with the concomitant resistance variation (blue curve). While only small resistance variations can be generated by hydrogen adsorption and double layer charging, a significantly higher tunability up to about 15 % with a pronounced hysteresis in the resistance-potential-characteristics can be observed in the oxygen regime. The R-variation with the imposed charge is however hysteresis-free, which is shown for this measurement in figure 4.5. This indicates a direct relation of R to oxygen adsorption/desorption, which will be studied in the following.

The CV between −465 mV and −35 mV (green and red in figure 4.3) is shown in more

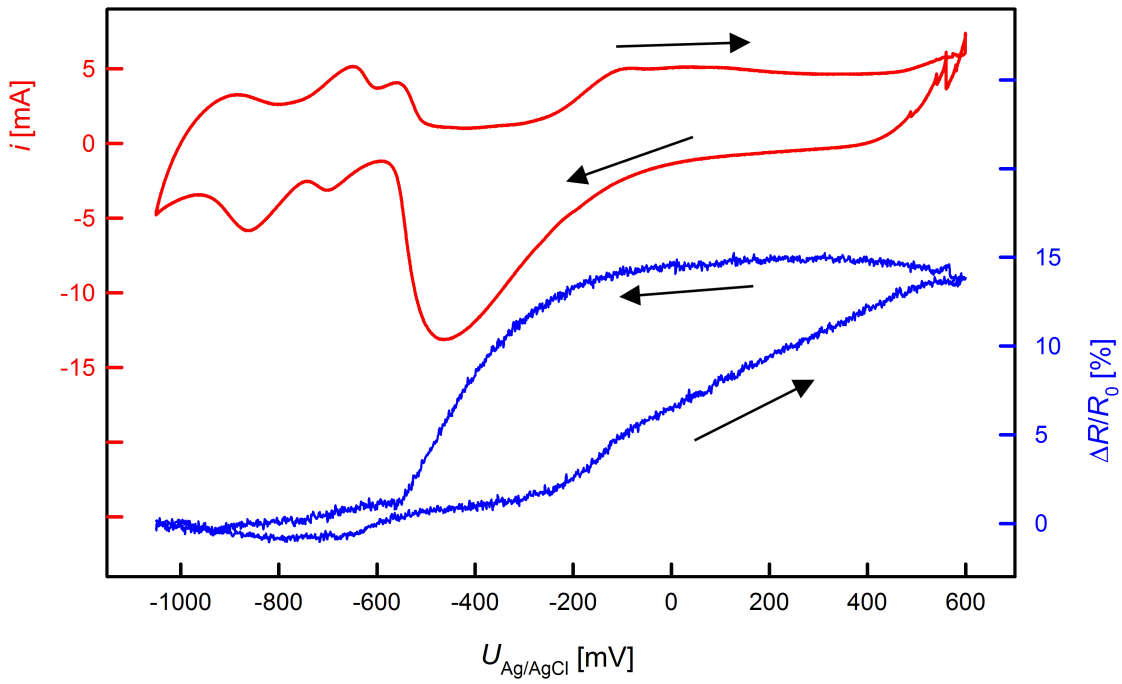

Figure 4.4: Relative variation $\Delta R/R_0$ of the electrical resistance of compacted Platinum Black upon CV in 1 M KOH with a scan rate of 0.5 mV/s between −1050 mV and +600 mV, limited by avoiding hydrogen and oxygen evolution. The reference value R_0 refers to the sample resistance in the double layer region. Current i (red) and $\Delta R/R_0$ (blue) are plotted as a function of potential $U_{Ag/AgCl}$ versus the commercial Ag/AgCl reference.

detail in figure 4.6 along with the corresponding variation of the electrical resistance. The green- and red-colored data in both curves again indicate the anodic and cathodic scan direction, respectively. Two subsequent voltammetric cycles are plotted for both signals, which can hardly be discerned, illustrating the good reversibility of the R-measurements in the steady-state CV.

The electrical resistance R increases upon positive charging, exhibiting a total variation $\Delta R/R_0$ of about 6 % in this potential range (figure 4.6). As already seen in figure 4.4, the variation of R with the potential $U_{Ag/AgCl}$ exhibits a pronounced hysteresis. The high sensitivity of R with respect to superficial oxygen adsorption is yet visible better here in this more detailed view: the resistance steeply increases/decreases right where oxygen adsorption/desorption takes place in the CV. Taking a closer look at the high potential edge,

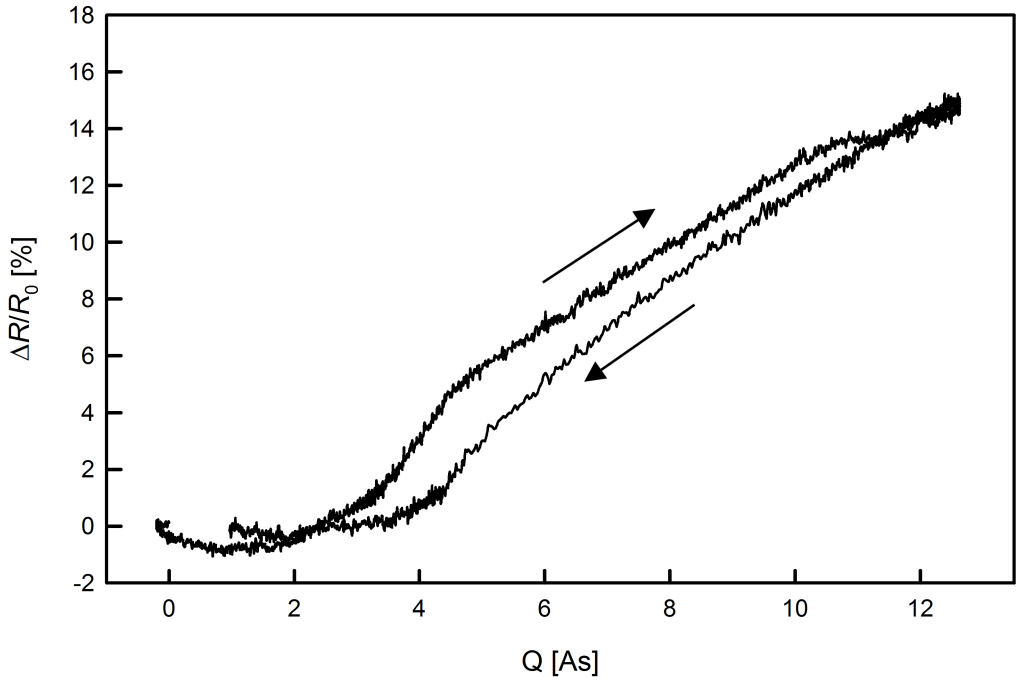

Figure 4.5: Relative variation of the resistance $\Delta R/R_0$ of compacted Platinum Black upon CV-cycling in 1 M KOH at potentials $U_{Ag/AgCl}$ between -1050 mV and $+600$ mV with a scan rate of 0.5 mV/s, plotted as a function of the imposed charge Q.

a further increase in R can be observed when the scan direction is reversed (start of red-colored curve) as long as the charging current i is still positive. When i finally changes its sign at about -75 mV, the resistance also starts to decrease. Thus the resistance variation is proportional to the transferred charge, which is demonstrated by the green and red curve in figure 4.7, representing the R-Q-plot of this experiment: plotting the resistance variation as a function of the imposed charge results in a hysteresis-free curve.

The pink curve in figure 4.7 shows the resistance variation upon double layer charging at potentials $U_{Ag/AgCl}$ between -555 mV and -355 mV. In the double layer regime, associated with a featureless CV (shown as pink curve in figure 4.3), the charging currents and thus transferred charges are small compared to chemisorption. In this regime the resistance exhibits a hysteresis-free variation with applied potential $U_{Ag/AgCl}$ (not shown) as well as imposed charge Q. Along with a charge transfer of 0.3 As, a resistance variation of about 0.8 % can be observed.

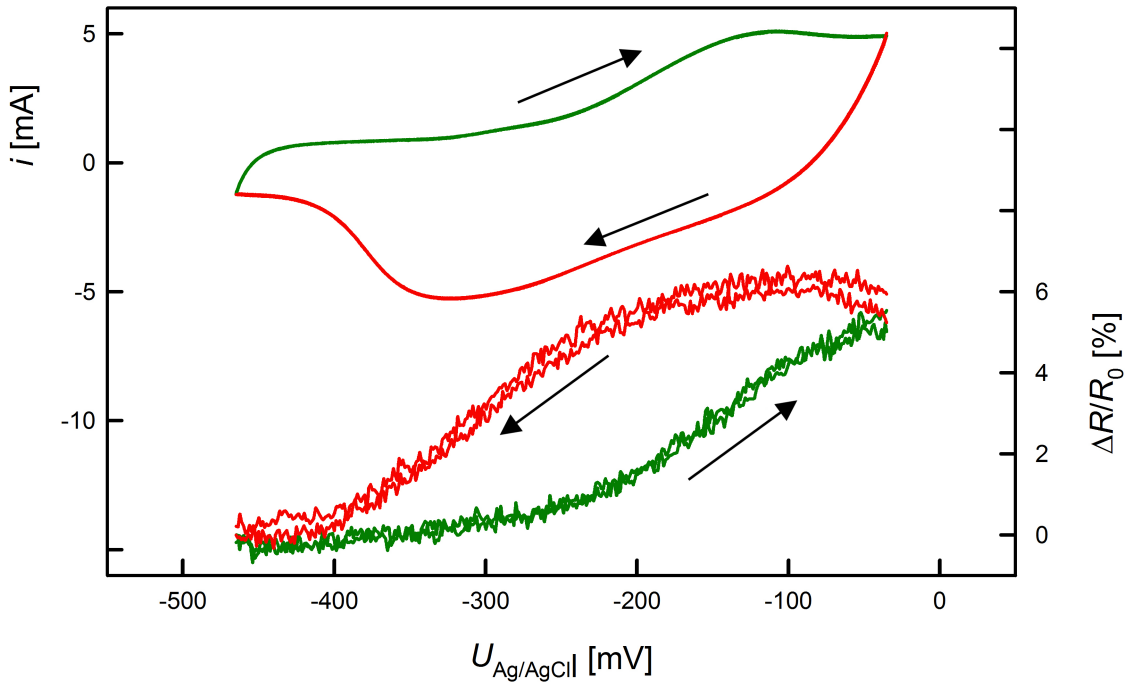

Figure 4.6: Current i and relative variation of the resistance $\Delta R/R_0$ of compacted Platinum Black upon CV-cycling in 1 M KOH at potentials $U_{Ag/AgCl}$ between -465 mV and -35 mV with a scan rate of 0.5 mV/s. Cathodic scan is indicated by red, anodic scan by green lines. To demostrate the good reversibility two CV cycles are shown in each curve.

From the R-Q-plots, the charge coeficcients $(\Delta R/R_0)/\Delta Q$ of the respective regimes can be deduced, which characterize the sensitivity of R to imposed charge. The linear regressions of the R-Q-characteristics for both regimes are plotted as dashed lines in figure 4.7, showing the chemisorption regime in black and double layer cycling in pink. For both regimes similar slopes and thus charge coefficients are observed, which are listed in table 4.2.

The charge-dependence of R is also nicely illustrated by figure 4.8, where the potential range of oxygen ad- and desorption (potentials $U_{Ag/AgCl}$ between -465 mV and -35 mV) is

Table 4.2: Charge coefficients $[(\Delta R/R_0)/\Delta Q]$ determined upon CV cycling in different regimes.

	$\frac{\Delta R/R_0}{\Delta Q}$ $[\%\cdot(\mathrm{As/g})^{-1}]$
double layer	0.25
ad-/desorption	0.27

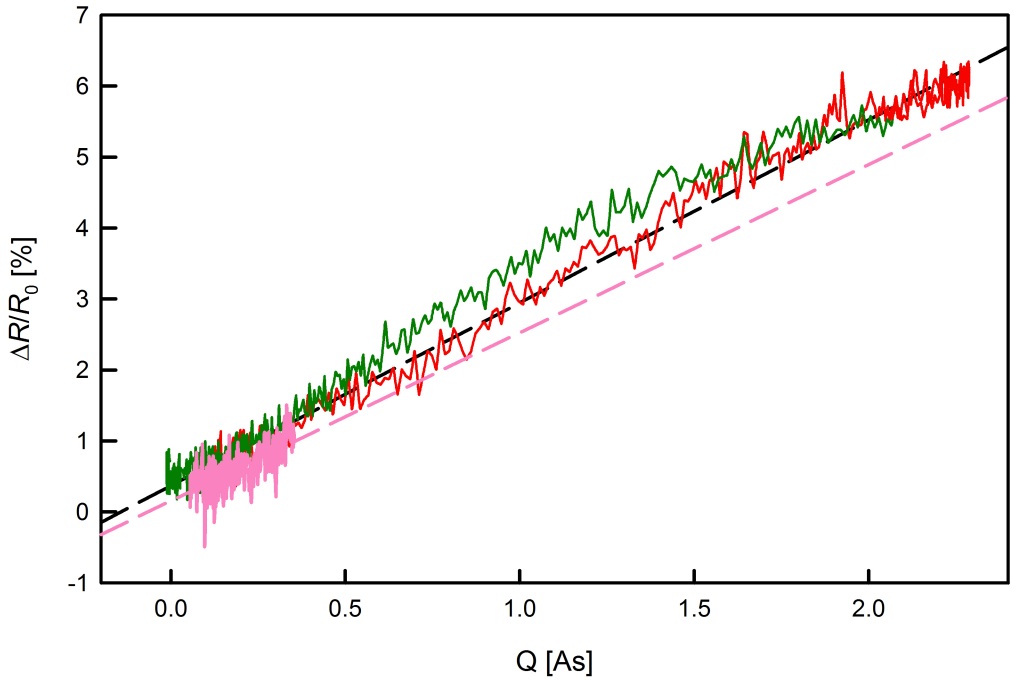

Figure 4.7: Resistance variation $\Delta R/R_0$ of compacted Platinum Black as function of charge Q, imposed upon cyclic voltammetry in different windows of potential $U_{Ag/AgCl}$. The green and red curve show oxygen ad- and desorption sorption at potentials between −465 mV and −35 mV, the pink curve shows double layer charging between −555 mV to −355 mV. Dashed lines show linear regressions of the curves.

scanned by CVs with different rates: while the curves plotted as a function of the applied potential $U_{Ag/AgCl}$ (figure 4.8A) strongly depend on the scan rate, exhibiting higher currents and a much larger hysteresis for the faster scan, the $\Delta R/R_0$-Q curves perfectly resemble each other, showing no hysteresis and similar slopes.

The dependence of $\Delta R/R_0$ on the imposed charge was also investigated using the electrochemical method of chronoamperometry (CA), where a correction of the leak current is possible, allowing for a higher accuracy of charge determination. Two different potential regimes were investigated, which were illustrated as colored cyclic voltammograms in figure 4.3. The regime between −465 mV and −35 mV (green/red), which is identical to that investigated in the CV-mode studies above (figures 4.6 and 4.8), characterizes adsorption and desorption, whereas the regime between 0 mV and +500 mV corresponds to pseudocapacitive charging in the steady state of strong oxygen adsorption (blue).

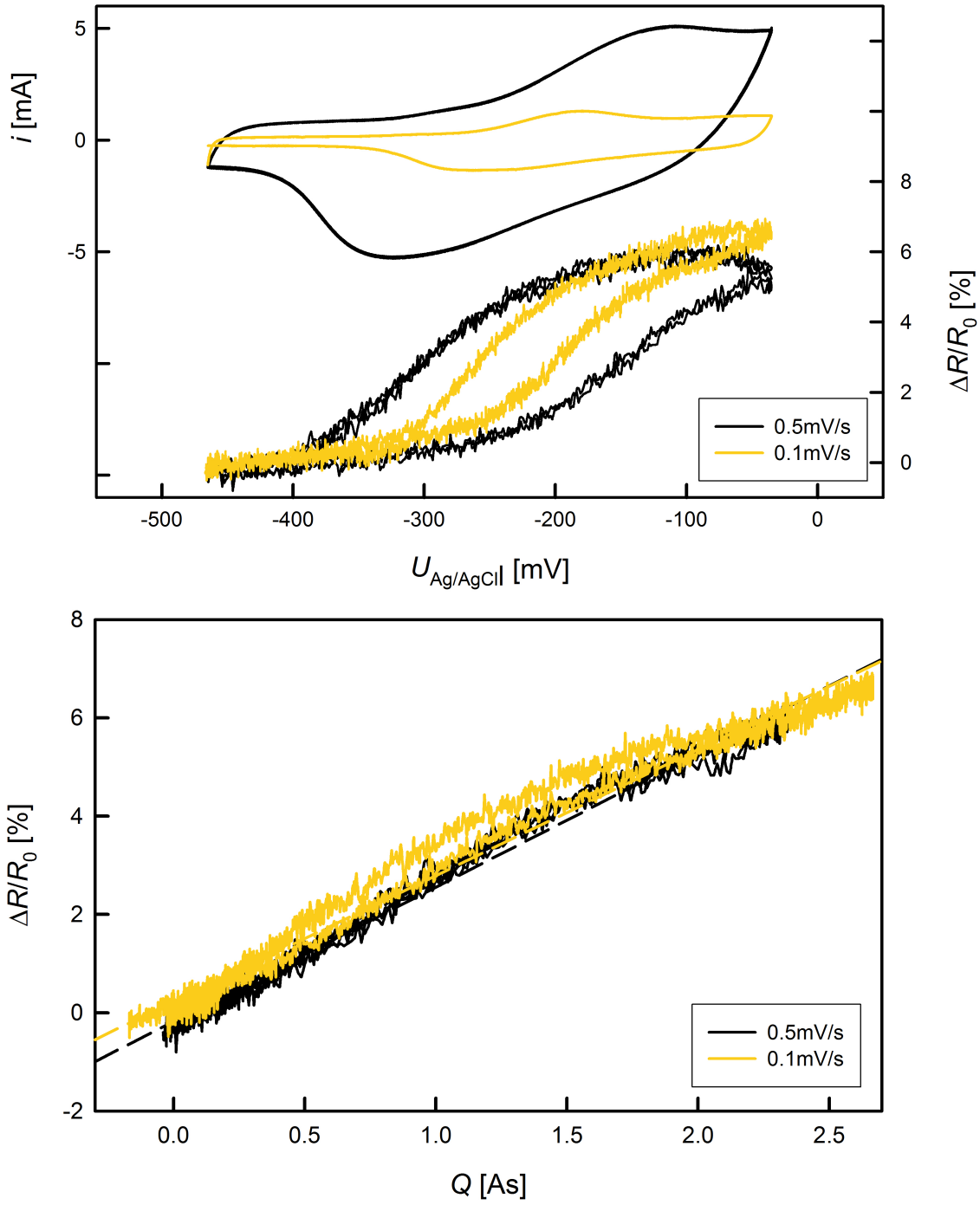

Figure 4.8: Cyclic voltammetry of compacted Platinum Black in 1 M KOH at potentials $U_{Ag/AgCl}$ between -465 mV and -35 mV, recorded at scan rates of 0.5 mV/s (black) and 0.1 mV/s (yellow). A: Current i and relative variation of the resistance $\Delta R/R_0$ as a function of applied potential $U_{Ag/AgCl}$. B: Relative variation of the resistance $\Delta R/R_0$ plotted as a function of the imposed charge Q.

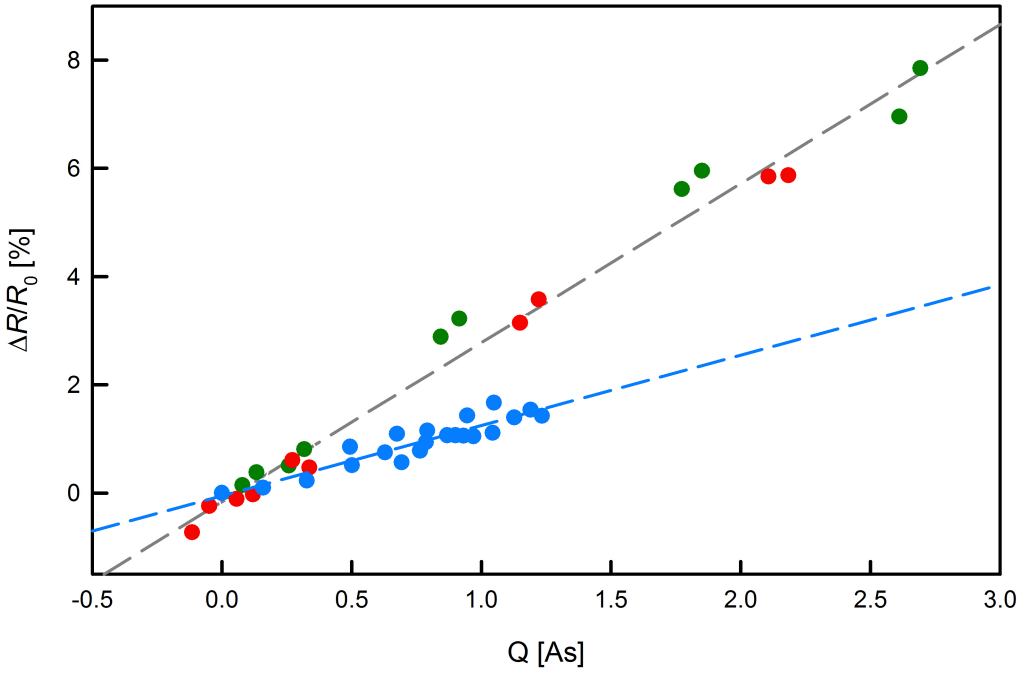

Figure 4.9: Resistance variation of compacted Platinum Black upon adsorption (green), desorption (red) and pseudocapacitive charging in the regime of strong oxygen adsorption (blue) in 1 M KOH. $\Delta R/R_0$ is plotted as a function of charge, transferred in CA steps of 60 minutes each with step intervals of 86 mV (green/red) or 100 mV (blue).

In each potential region, CA measurements were performed in consecutive step intervals of 86 mV (green/red) or 100 mV (blue). After an equilibration time of 60 minutes at a given potential, the transferred charge ΔQ per sample mass, relative to the first measurement point in the respective regime, was determined from the monitored charging current and the electrical resistance was measured. The data $\Delta R/R_0$ in dependence of ΔQ obtained in this way are presented in figure 4.9, the corresponding charge coefficients are listed in table 4.3.

Table 4.3: Charge coefficients $[(\Delta R/R_0)/\Delta Q]$ determined upon CA cycling in different regimes.

	$\frac{\Delta R/R_0}{\Delta Q}$ $[\%\cdot(\mathrm{As/g})^{-1}]$
ad-/desorption	0.31
oxidized	0.14

Also in figure 4.9 the CA sequence was repeated twice for both chemical regimes in order to show the good reversibility of the $\Delta R/R_0$ variations. The measurements in the regime of ad-/desorption allow for a comparison of the CA- (see figure 4.9) and CV-mode (see figure 4.6), which yield similar, high charge coefficients, both indicating a strong sensitivity of R to the surface modifications. In the regime of strong oxygen adsorption (blue), besides a significantly smaller total variation of $\Delta R/R_0$, also the relative dependence on ΔQ is significantly weaker.

4.2.2 Nanoporous Platinum

By far the material most intesively studied in this thesis is nanoporous platinum produced by dealloying (np-Pt). Besides etching experiments (shown above in figure 4.2) detailed resistometric and dilatometric studies were conducted on np-Pt both in well reduced (metallic) state and in oxidized conditions. The findings presented in the following were partially published in two articles, which are listed as references [30] and [33] in this thesis.

Figure 4.10 shows the R-variation of a well-reduced np-Pt sample (np-Pt R2, see chapter 3.3) during CV cycling in 1 M KOH with a scan rate of 0.1 mV/s at potentials $U_{Ag/AgCl}$ between -1050 mV and $+450$ mV. Following the procedure described in section 3.1, from the charge flow associated with hydrogen desorption, corrected for double layer charging, an electrochemically active surface area of 2.5 m^2 was calculated. Assuming that the np-Pt material is free of residual copper, this corresponds to a surface-to-mass ratio of about 30 m^2/g.

Qualitatively the charging-induced resistance variation behaves similar to that presented above for compacted Platinum Black (compare figure 4.4): only small resistance variations are observed upon hydrogen adsorption and double layer charging. In the oxygen regime the resistance varies significantly stronger with a hysteresis in the R-U-characteristics (see figure 4.10A). The R-Q-plot shown in figure 4.10B is again hysteresis-free. From a quantitative point of view, however, the relative variation $\Delta R/R_0$, which amounts to about 58 %, exceeds

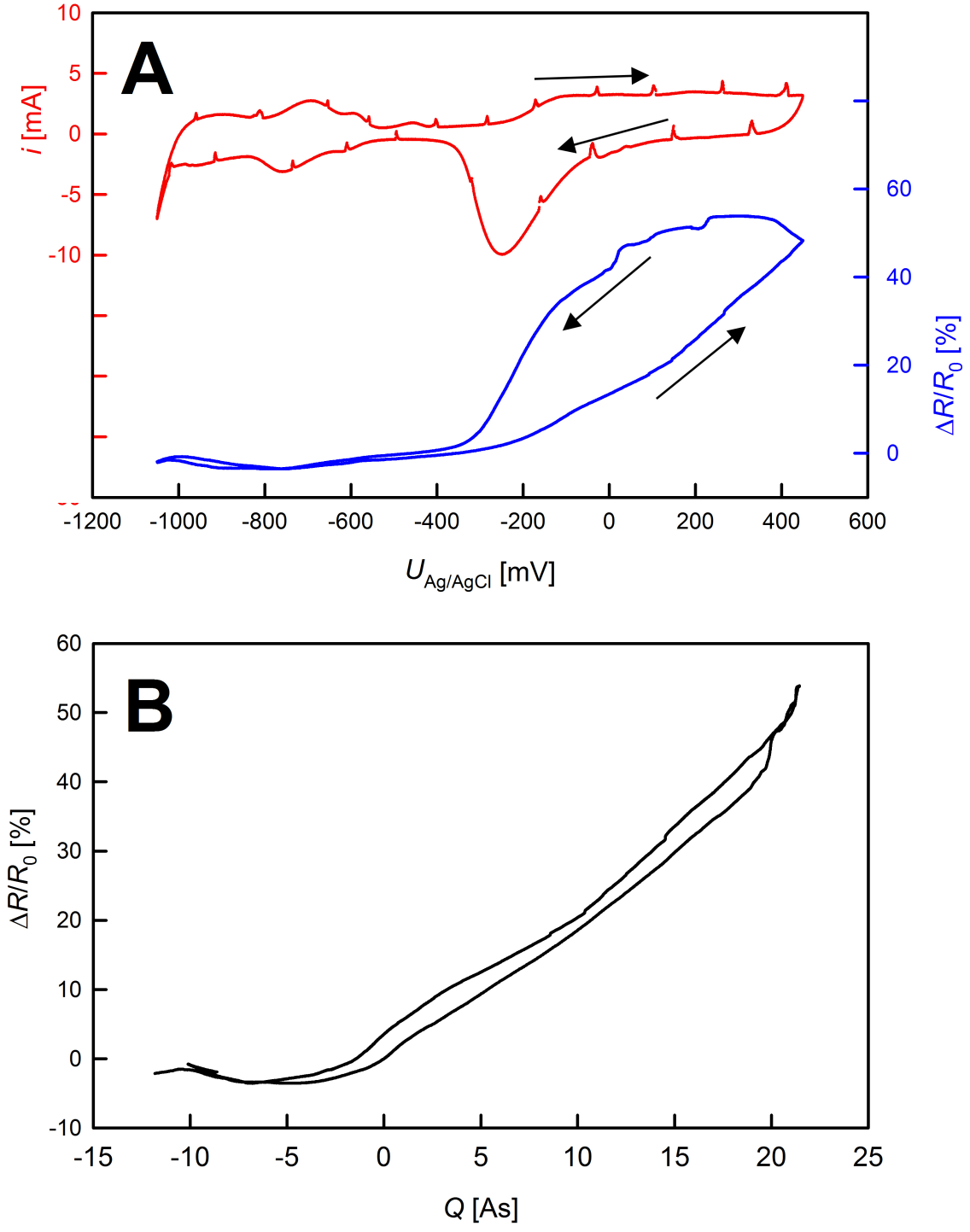

Figure 4.10: Relative variation $\Delta R/R_0$ of the electrical resistance of well-reduced np-Pt R2 upon CV in 1 M KOH with a scan rate of 0.1 mV/s between −1050 mV and +450 mV, limited by avoiding hydrogen and oxygen evolution. The reference value R_0 refers to the sample resistance in the double layer region at −450 mV. (A) Current i (red) and $\Delta R/R_0$ (blue) as a function of $U_{Ag/AgCl}$. (B) Presentation of $\Delta R/R_0$ data in relation to imposed charge Q.

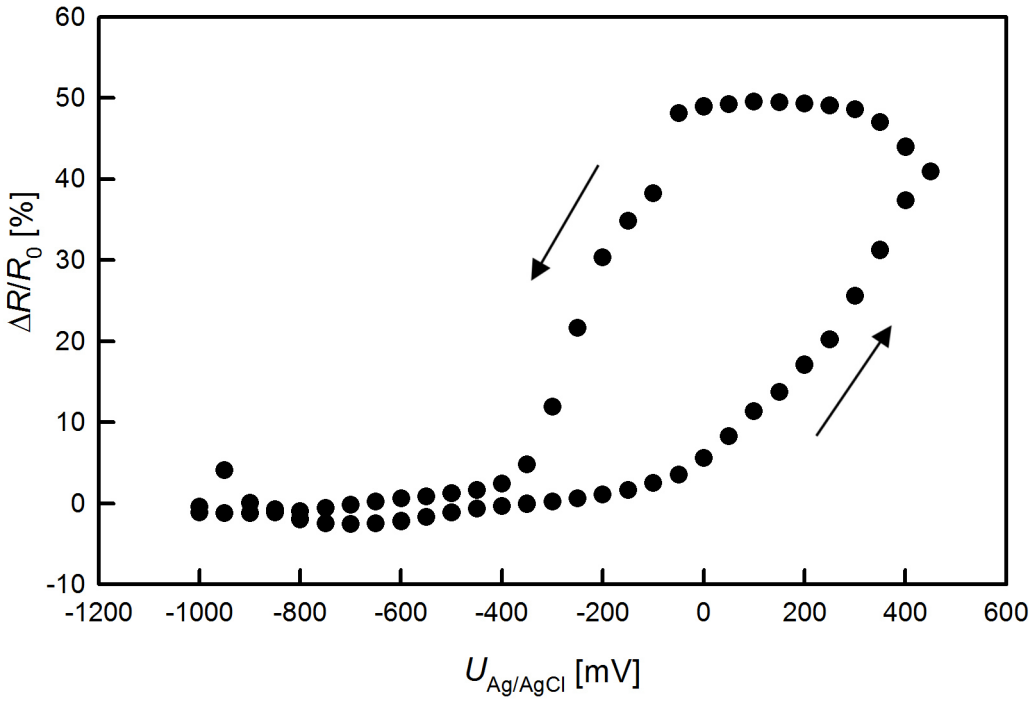

Figure 4.11: Relative variation $\Delta R/R_0$ of the resistance of np-Pt R2 upon chronoamperometric charging steps in 1 M KOH at potentials $U_{Ag/AgCl}$ with a step time of 60 min and a step width of 50 mV between −1000 mV and +450 mV. R values are measured at the end of each potential step. The reference value R_0 refers to the open circuit potential before the charging procedure.

that observed for Platinum Black in the same potential range by about a factor of five. This is due to the extremely high surface-to-volume ratio of the samples produced by dealloying.

In order to confirm the validity of the measured data by excluding any possible influence of the potentiostat's charging current on the resistance measurements, the R-variation was also studied using a chronoamperometric charging program. The potential of the nanoporous sample was varied in CA steps with a step time of 60 min and a step width of 50 mV between −1000 mV and +450 mV. Data points of the resistance were then taken at the end of each 60 min charging step when the charging current had faded away. The results of this control measurement, shown in figure 4.11, are in perfect agreement with the data acquired by cyclic voltammetry.

The observed property tunability of np-Pt upon electrochemical charging is further sup-

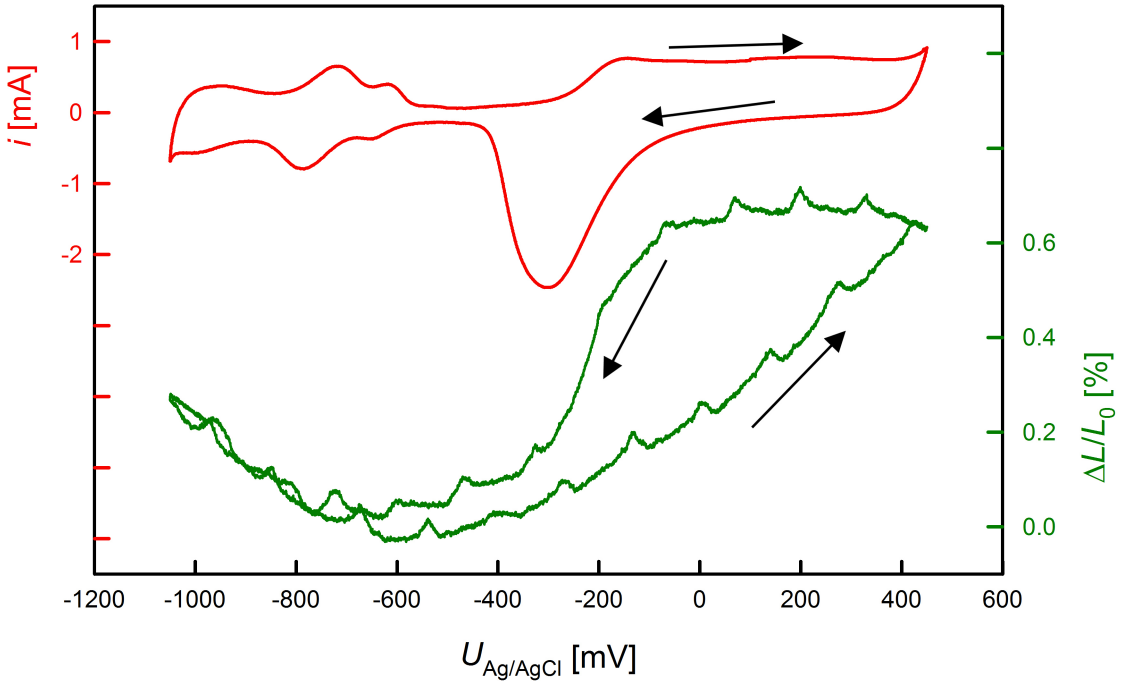

Figure 4.12: Relative thickness variation $\Delta L/L_0$ of np-Pt D1 upon CV in 1 M KOH with a scan rate of 0.1 mV/s between −1050 mV and +450 mV, limited by avoiding hydrogen and oxygen evolution. The reference value L_0 refers to the sample thickness in the double layer region at −450 mV. Current i (red) and $\Delta L/L_0$ (green) are plotted as a function of $U_{Ag/AgCl}$.

ported by dilatometric measurements. An overview CV of sample np-Pt D1 with the concomitant length changes is plotted in figure 4.12. The similarities between variations in sample thickness and resistance are impressive (compare figure 4.10A): the np-Pt platelet exhibits its lowest expansion in the double layer region. Upon adsorption thickness increases up to about 0.3 % and 0.7 % were recorded in the hydrogen and oxygen regime respectively.

The dilatometric curve (plotted green in figure 4.12) exhibits slight oscillations with a periodicity repeated in intervals of approximately 140 mV, which corresponds to a period of about 20 minutes. For the acutation measurements a direct influence of the measuring instruments (potentiostat and dilatometer) on each other, as it is the case during resistometry, can be excluded. The oscillating signal overlaying the charging-induced length change curve stems from sample expansion caused by room temperature variations and reflects the cycle

of the air conditioning system. As clearly visible, the length changes due to electrochemical charging by far exceed those due to temperature. Therefore the room temperature variations have no significant influence on the experimental results, however the observed oscillations demostrate the sensitivity of the measurement.

Since the property variations are rather small in the double layer regime and therefore hardly visible in the overview CVs presented above, the potential region between −510 mV and −360 mV versus the Ag/AgCl reference electrode was studied separately in more detail, which is presented in figures 4.13 and 4.14 for resistometry and dilatometry respectively. In the double layer CV, both properties increase upon positive charging, showing a linear variation both with potential $U_{Ag/AgCl}$ and with the imposed charge, as expected owing to the capacitive nature of charging in this regime.

The electrical resistance (figure 4.13) shows a relative variation $\Delta R/R_0$ of about 1 %, achieved for an imposed charge of about 0.5 As. For a reliable charge determination, the spikes in the current curve, which are caused by four point current pulses, had to be corrected by a linear approximation, which is shown as a dashed line in the CV-plot. The sample thickness varies only by about 0.04 % in this potential regime (figure 4.14). The strong signal noise of $\Delta L/L_0$ indicates the limit of the measurement resolution, nevertheless, also here an increase upon positive charging is clearly visible.

Sample np-Pt R2 was also studied with regards to aging in reduced state, which is shown in figure 4.15. In this plot the sample resistance in the double layer regime (blue) as well as the resistance tunability (black) are shown as a function of time t_a in days after the first reduction of the as-dealloyed condition (primary oxide), during which the sample was subjected to various charging treatments.

The plotted values were determined during identical CV runs performed at the given aging times for the purpose of electrochemical activation. All cyclic voltammograms were recorded in 1 M KOH with a scan rate of 1 mV/s in the potential range between −1050 mV and +450 mV, where hydrogen and oxygen evolution is avoided. The values R_{DL} were taken in the double layer regime at a potential $U_{Ag/AgCl}$ of −450 mV. The black data points

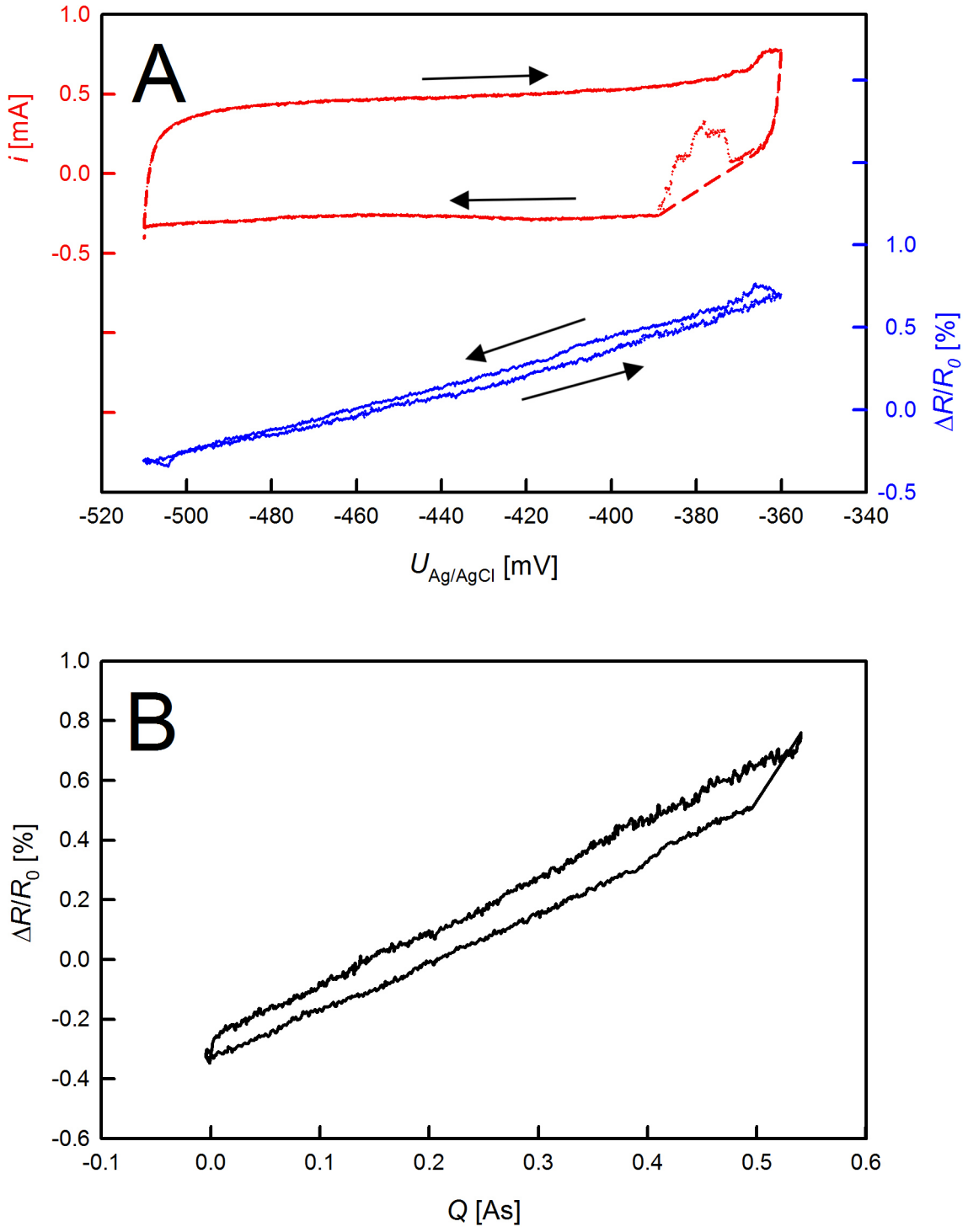

Figure 4.13: Relative variation $\Delta R/R_0$ of the electrical resistance of np-Pt R2 upon CV in the double-layer regime between -510 mV and -360 mV, measured with a scan rate of 0.1 mV/s. The reference value R_0 refers to the sample resistance at -450 mV. (A) Current i (red) and $\Delta R/R_0$ (blue) as a function of potential $U_{Ag/AgCl}$. For charge determinations, the spikes in the CV caused by four point current pulses, are corrected by a linear approximation (dashed line). (B) Presentation of $\Delta R/R_0$ data in relation to the imposed charge Q.

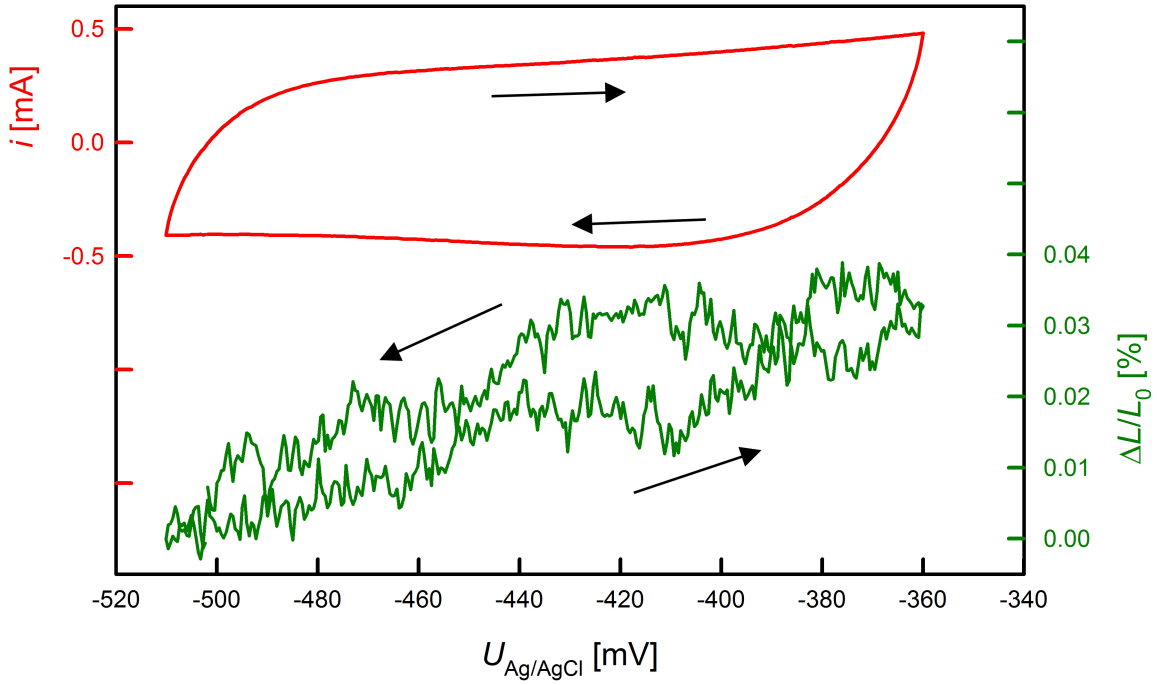

Figure 4.14: Relative thickness variation $\Delta L/L_0$ of np-Pt D1 upon CV in the double-layer regime between −510 mV and −360 mV, measured with a scan rate of 0.1 mV/s. The reference value L_0 refers to the sample thickness at the lower potetial edge (−510 mV). Current i (red) and $\Delta L/L_0$ (green) are plotted as a function of $U_{Ag/AgCl}$.

$\Delta R_{+450}/R_{DL}$ give the relative increase in sample resistance between the reference point in the double layer regime and the upper potential edge of the activation CV. As the sample ages, both quantities tend to decrease, which will be discussed below in chapter 5.2.

Primary Oxide

As already mentioned, all experiments shown above for np-Pt were recorded for a well-reduced, metallic sample. This however does not represent the as-prepared condition of a dealloyed sample. This initial state is characterized by a strongly bound primary oxide, which, once removed by electrochemical reduction, cannot be entirely restored. Detailed studies of this freshly dealloyed condition, associated with particular physical properties [29, 33, 46] will be presented in the following.

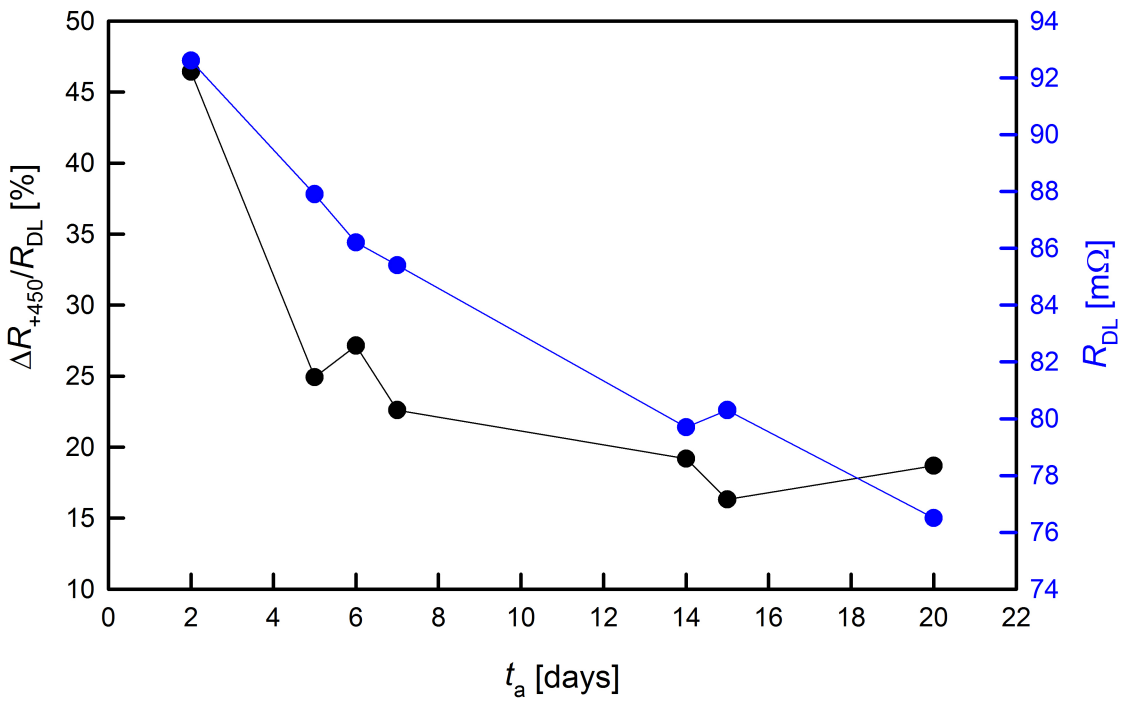

Figure 4.15: Resistance behavior of np-Pt R2 upon cyclic voltammetry, performed in 1 M KOH with a scan rate of 1 mV/s at potentials $U_{Ag/AgCl}$ between −1050 mV and +450 mV as a function of sample age t_a after the first reduction of the as-dealloyed state. The resistance variation $\Delta R_{+450}/R_{DL}$ between the double layer regime (−450 mV) and the upper potential edge (+450 mV) is shown in black, the absolute value of the sample resistance in the double layer regime R_{DL} is plotted in blue.

Figure 4.16 shows a cyclic voltammogram of the sample np-Pt R2 measured in 1 M KOH at potentials $U_{Ag/AgCl}$ between −1050 mV and +450 mV with a scan rate of 0.1 mV/s. The sample was in as-dealloyed conditon (with primary oxide) before this measurement. During the first cycle (red) starting from the upper potential limit of +450 mV, reduction of the strongly bound primary oxide occurs as signified by a prominent peak at about −550 mV. The reduction is also visible by a change in the sample's optical appearance: while samples in as-dealloyed condition are dull and dark, they regain metallic gloss when the primary oxide is stripped. Subsequent cycles of the CV are in good agreement with typical cyclic voltammograms of polycrystalline Pt well known from the textbook literature. The noisy behavior of the current i in the oxygen regime indicates temporary contact losses that could yet be resolved by continuous cycling. To avoid any sample damage, the resistance variation

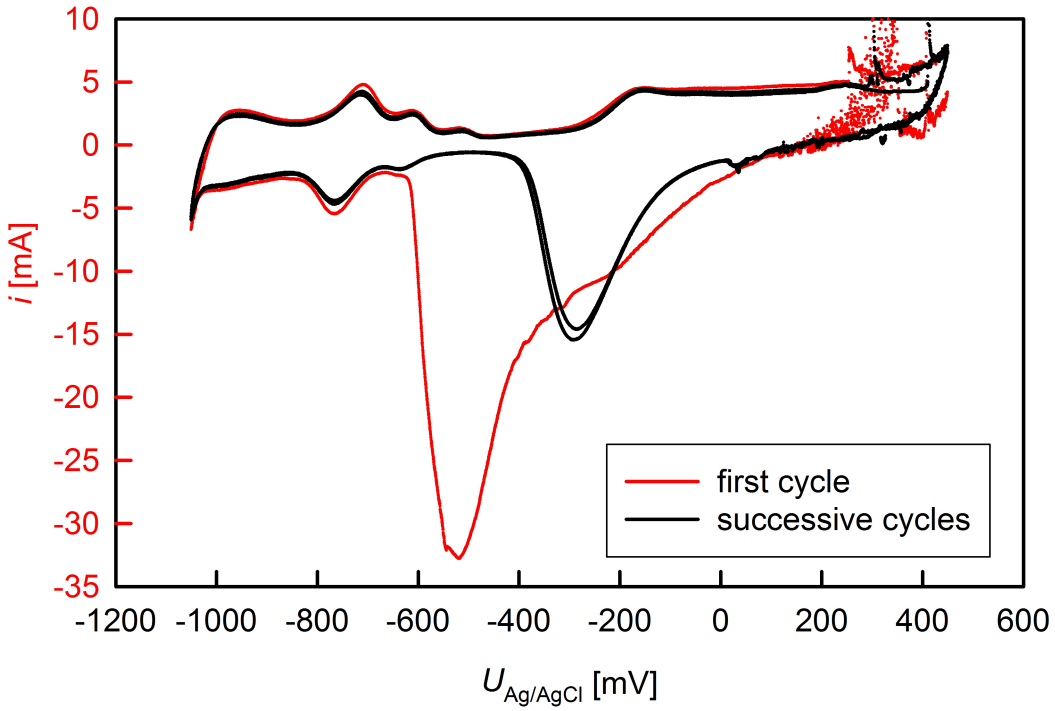

Figure 4.16: CV of np-Pt R2 in as-dealloyed condition with a scan rate of 0.1 mV/s in 1 M KOH aqueous solution between +450 mV and −1050 mV, limited by avoiding oxygen and hydrogen evolution. Current i is plotted as a function of $U_{Ag/AgCl}$. The first cycle (red) strongly differs from successive cycles (black) because of the irreversible removal of the strongly bound primary oxide.

was not monitored simultaneously to charging during this experiment, however, resistance measurements performed at open circuit potential before and after the CV reveal a resistance decrease by more than a factor of 10 due to removing the primary oxide.

When cycling a nanoporous platinum sample in as-dealloyed condition in a potential range where the primary oxide is retained (pseudocapacitive charging of the primary oxide), the observed property variations strongly differ from those presented above for well-reduced np-Pt (see figure 4.17 for sample np-Pt R2). At potentials $U_{Ag/AgCl}$ between +50 mV and +450 mV the electrical resistance varies by about 5 % relative to the resistance R_0 at open circuit potential in the primary oxidized condition (figure 4.17A). The variation exhibits a sign inversion with an instantaneous resistance minimum at the lower potential edge and a delayed resistance minimum at the upper potential edge, and resistance maxima in be-

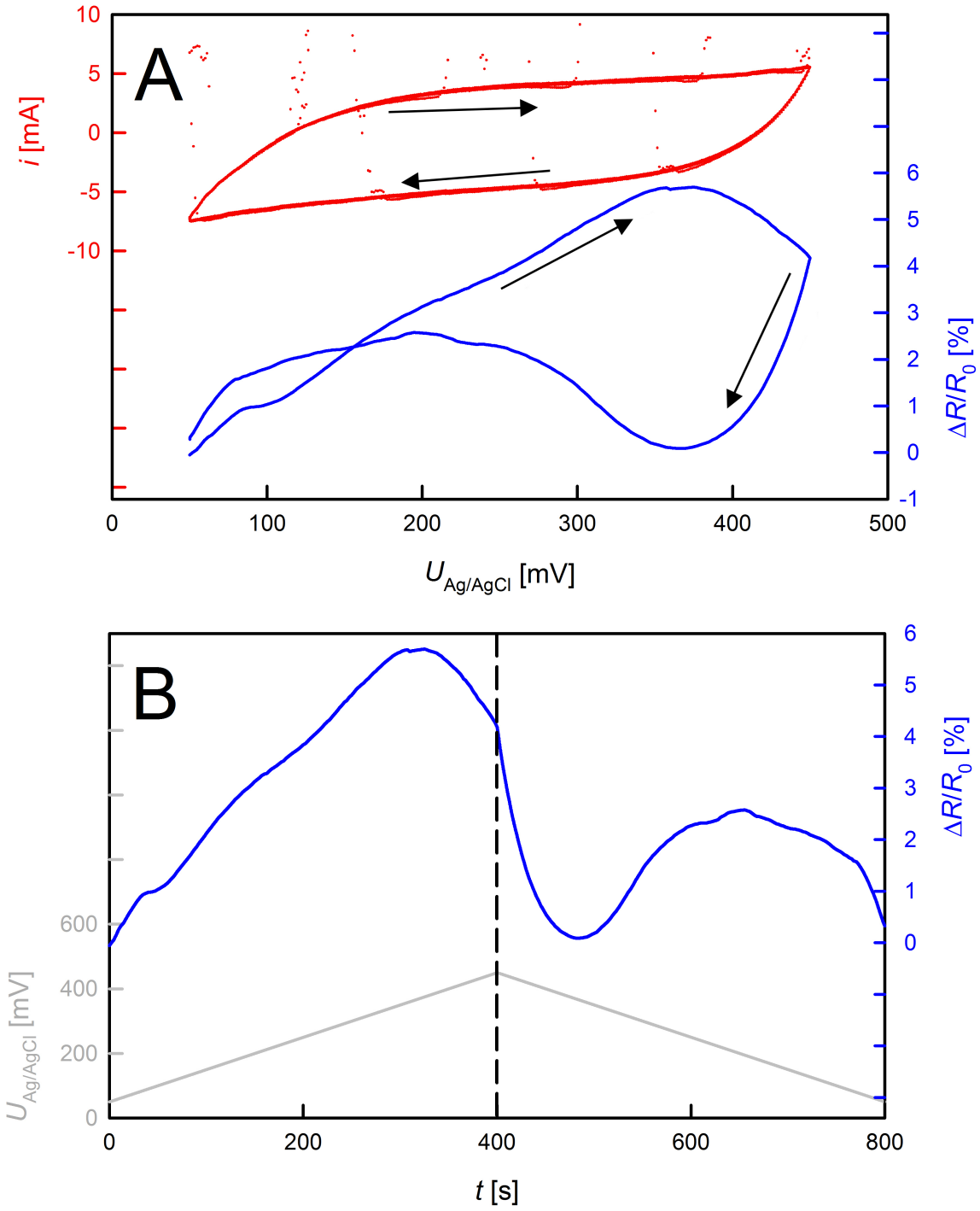

Figure 4.17: Relative variation $\Delta R/R_0$ of the electrical resistance of the primary-oxide-covered sample np-Pt R2 in the as-dealloyed state upon CV in 1 M KOH. The potential $U_{Ag/AgCl}$ is varied with a scan rate of 1 mV/s in the range between +50 mV and +450 mV, where the primary oxide is retained. The reference value R_0 refers to the open circuit potential before the charging procedure. (A) Current i (red) and $\Delta R/R_0$ (blue) as a function of $U_{Ag/AgCl}$. (B) Variation of $\Delta R/R_0$ (blue) and $U_{Ag/AgCl}$ (gray) with time.

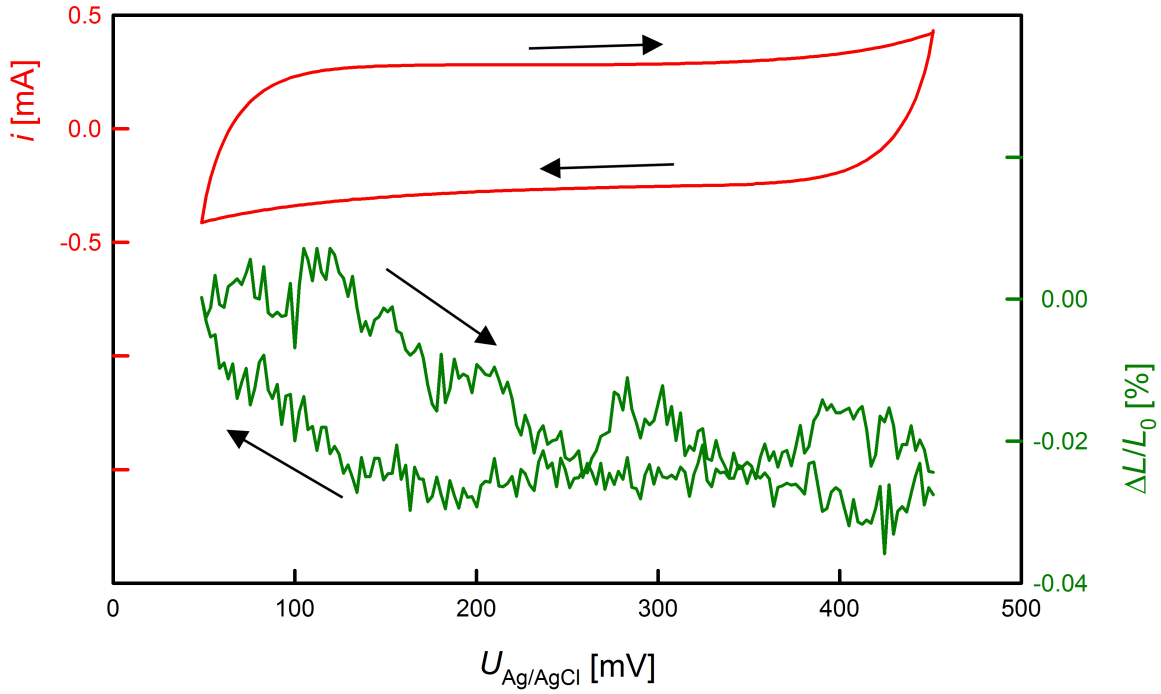

Figure 4.18: Relative thickness variation $\Delta L/L_0$ of the primary-oxide-covered sample np-Pt D1 upon CV between +50 mV and +450 mV, where the primary oxide is retained, investigated with a scan rate of 1 mV/s. The reference value L_0 refers to the sample thickness at open circuit potential before the charging procedure. Current i (red) and $\Delta L/L_0$ (green) are plotted as a function of $U_{Ag/AgCl}$.

tween (figure 4.17B). The potential at which the sign inversion occurs slightly differs from sample to sample, indicating that it sensitively depends on the oxygen adsorption and/or oxidation during dealloying. Moreover, the variation of R is also dependent on the direction of scanning: Upon cathodic scan, the transition between the regions of opposite sign slope occurs at lower potentials and also the total variation of R is reduced, as shown by a reduced maximum.

Also the charging-induced thickness variations in as-dealloyed condition, which are presented in figure 4.18, significantly differ from those in the double layer regime (shown in figure 4.14). In both cases the variations $\Delta L/L_0$ are very small, however an opposite sign behavior is observed: upon positive charging, the sample expands in the double layer regime, while a contraction is recorded for the primary oxide.

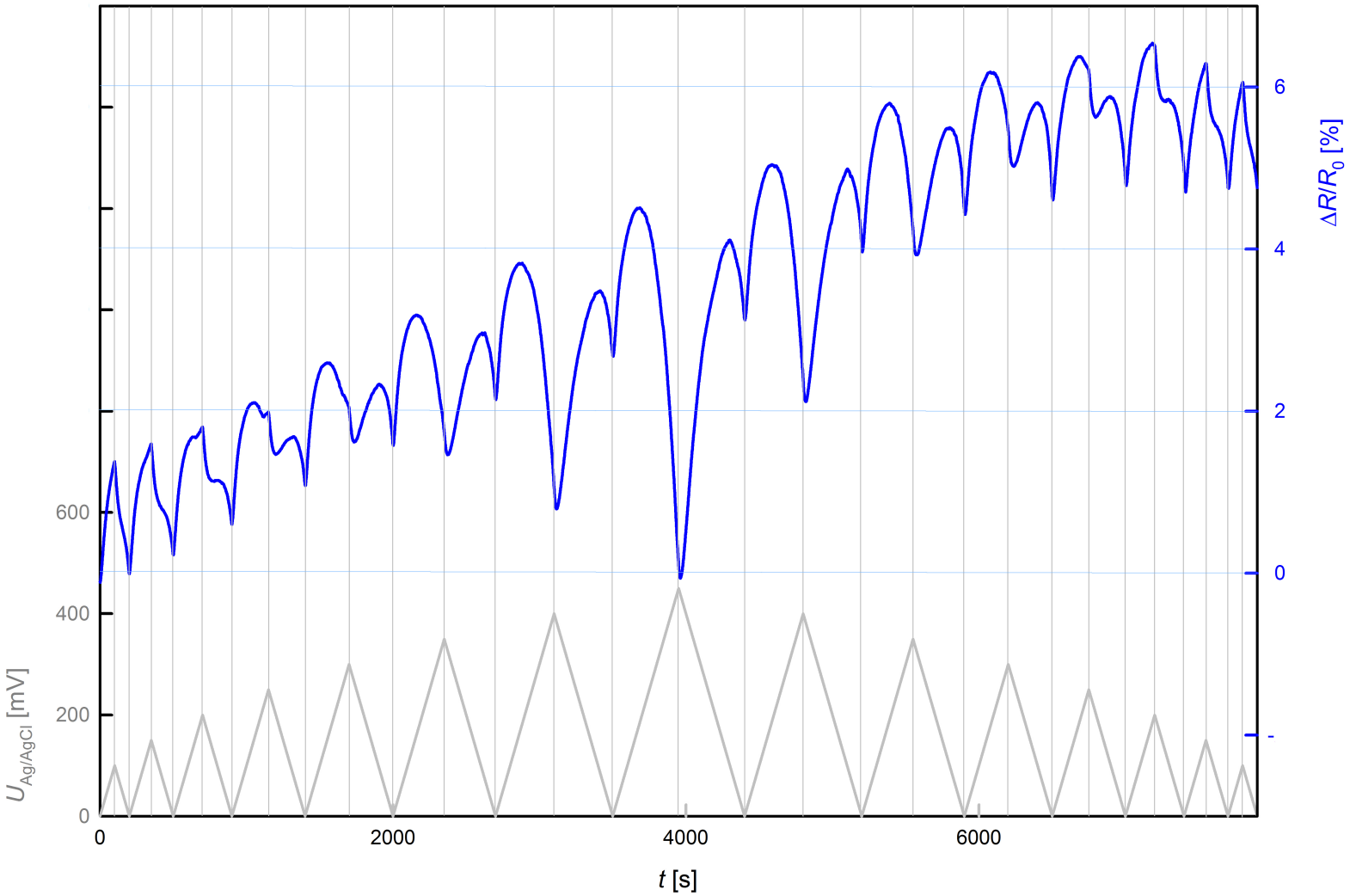

Figure 4.19: Charging sequence for sample np-Pt R3 in the primary oxide regime. Cyclic voltammograms are performed in 1 M KOH at a scan rate of 1mV/s, as lower CV limit always 0 mV is used, the upper CV limit is varied between 100 mV and 450 mV in steps of 50 mV. Applied potential $U_{Ag/AgCl}$ (gray) and resistance variation $\Delta R/R_0$ (blue) are plotted as a function of time.

Figure 4.19 shows a charging sequence performed for sample np-Pt R3 in the primary oxide regime: cyclic voltammograms are performed in 1 M KOH at a scan rate of 1mV/s with a constant lower potential limit of 0 mV and a varying upper potential limit. While in the narrow (low) potential ranges, only the resistance behavior with positive charge coefficient is visible, the opposite sign behavior at higher potentials appears more and more pronounced as the potential range of the CVs increases. When the applied potential ranges decrease again (at longer times), also the initial resistance behavior is reproduced. Superimposed to this reversible resistance behavior a slight upward drift of the sample resistance is observed, which occurs most likely due to further oxidation of the sample in this potential regime as well as possible slight sample damages, reducing the active conductor cross section of the sample.

The resistance behavior at both potential edges of the primary oxide regime was investigated in more detail in figure 4.20. In both regimes similar magnitudes of resistance variations are obtained, however also in this experiment, they oppose each other in sign. Moreover, while the resistance variation in the low potential regime (left) quasi instantaneously changes sign when the CV scan direction is reversed, it exhibits a certain delay at higher potentials (right), which might be an indicator for a different (chemical) nature of the property variation in the different regimes.

The rather sluggish response of R to potential variations becomes even more evident, when CVs are performed with different scan rates, as presented in figure 4.21. While the positive-sign variations at the lower potential edge (upper images) show similar behavior, regardless of the used scan rate, or, upon closer inspection, even a slight onset of the decreasing-R-process for the slowest scan, a significant scan-rate-dependence is observed at higher potentials (lower images): for the slowest scan, the resistance variation is nearly in phase with the applied potential, with increasing scan rate, however, $\Delta R/R_0$ is increasingly lagging behind the applied potential. Moreover, the amplitude of the variation of R strongly decreases with increasing scan rate, by almost a factor of 4 between the fastest and slowest scan plotted in figure 4.21.

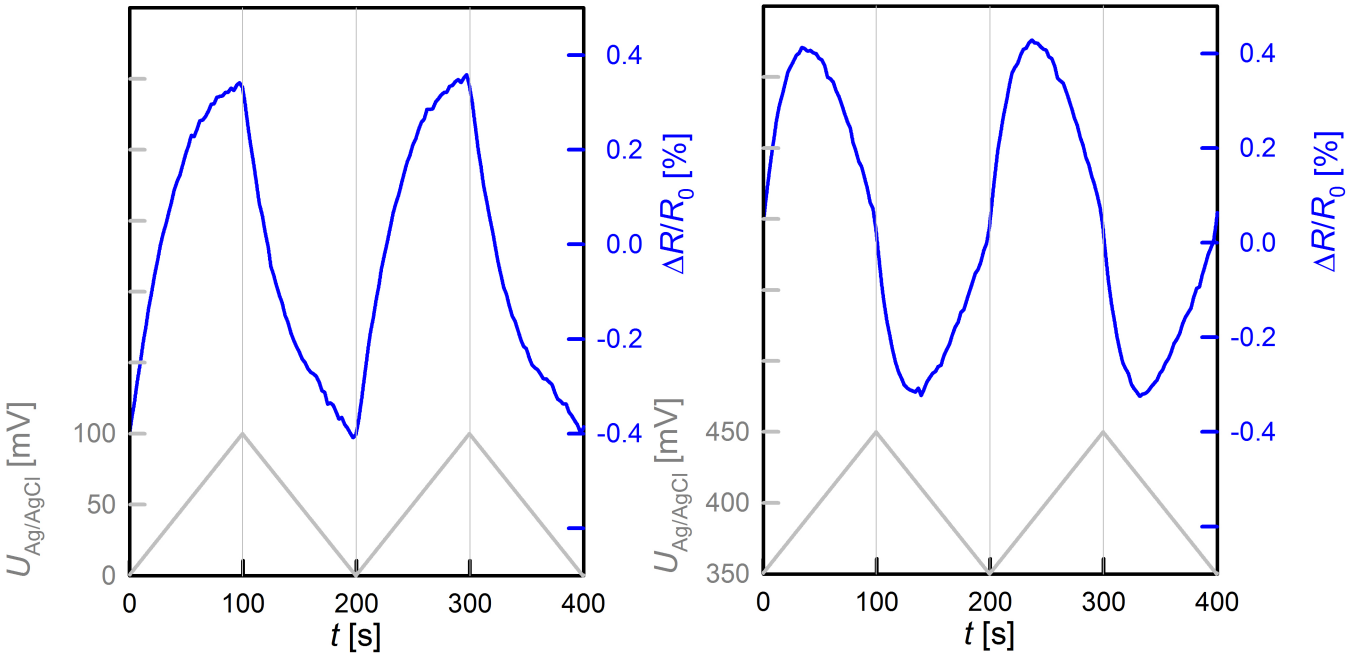

Figure 4.20: Detailed investigation of the CV behavior of npPt R4 near the edges of the primary oxide regime. The sample is cycled in 1 M KOH with a scan rate of 1 mV/s. At lower potentials between 0 mV and 100 mV (left) as well as at higher potentials between 350 mV and 450 mV (right) exhibiting opposite sign of the charge coefficients of the electrical resistance. Applied potential $U_{Ag/AgCl}$ (gray) and resistance variation $\Delta R/R_0$ (blue) are plotted as a function of time.

The resistance behavior in the primary oxide condition, characterized by reversible resistance variations with a positive charge coefficient at lower potentials and a negative charge coefficient at higher potentials (see figure 4.20), can reproducably be switched in sign by scanning from one regime to the other, which is illustrated in figure 4.22. Also visible in this plot, recorded over a longer measurement time, is a slight but constant increase in sample resistance upon scanning. Again, the most likely explanation for this drift lies in the ongoing oxidation in this high potential (anodic) charging regime. This oxidation does not only cause the observed drift in the overall resistance of the sample but also results in certain aging effects regarding the sign inversion behavior, which is shown for sample np-Pt R5 in figure 4.23.

In the initial state the resistance tunability of np-Pt R5 (topmost curve, dash-dotted)

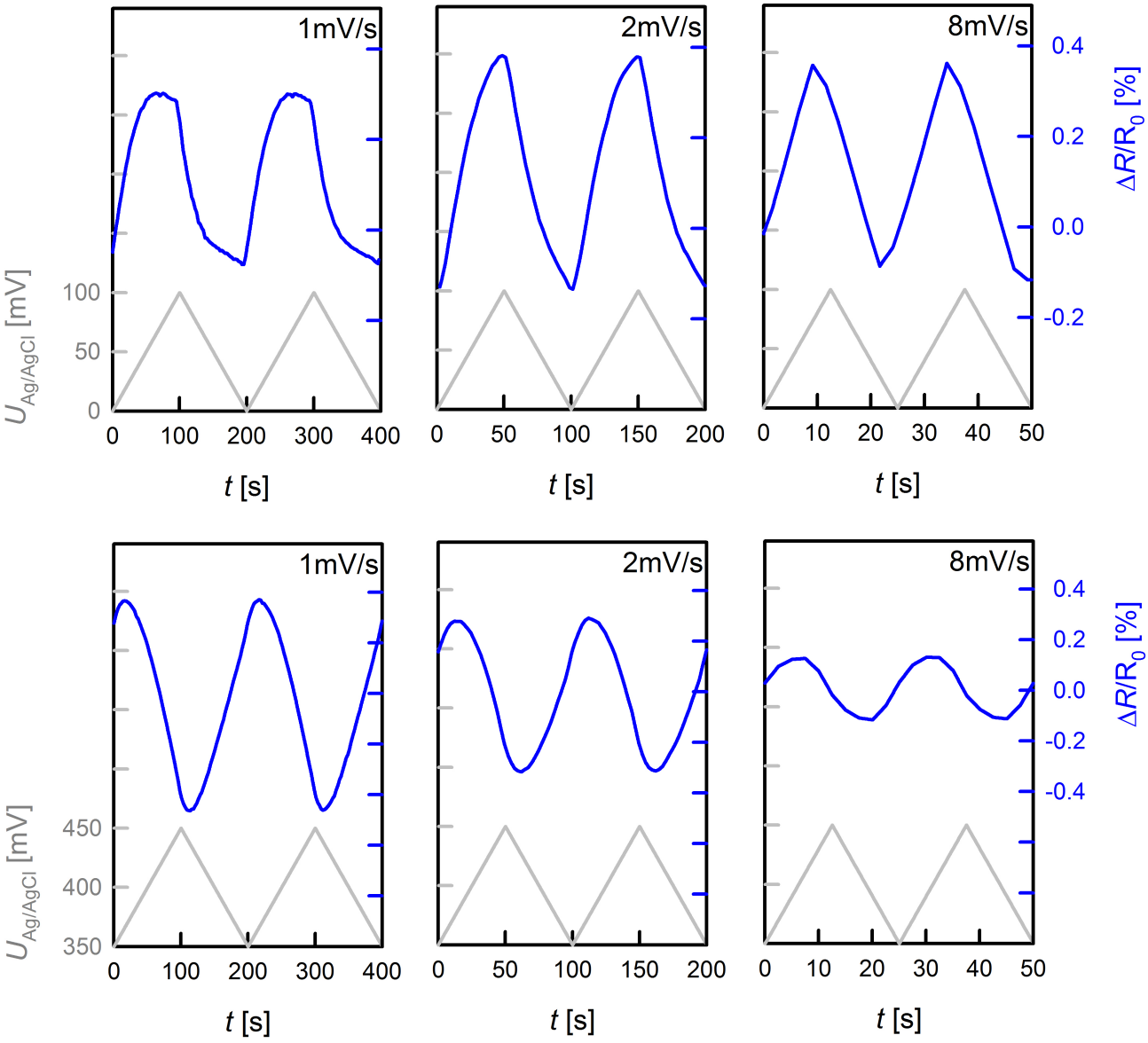

Figure 4.21: Resistance variation $\Delta R/R_0$ of np-Pt R5 upon cyclic voltammetry in 1 M KOH with different scan rates near the lower (0 mV - 100 mV, upper images) and higher (350 mV - 450 mV, lower images) potential edge of the primary oxide regime. Applied potential $U_{Ag/AgCl}$ (gray) and resistance variation $\Delta R/R_0$ (blue) are plotted as a function of time.

resembles that presented previously: The variation exhibits a sign inversion with resistance minima near the CV's reversal points. The resistance maxima in between are rather weakly pronounced in the case of np-Pt R5 (similar to sample np-Pt R2, compare figure 4.17), especially upon negative scan only visible as a small hump. After aging caused by various

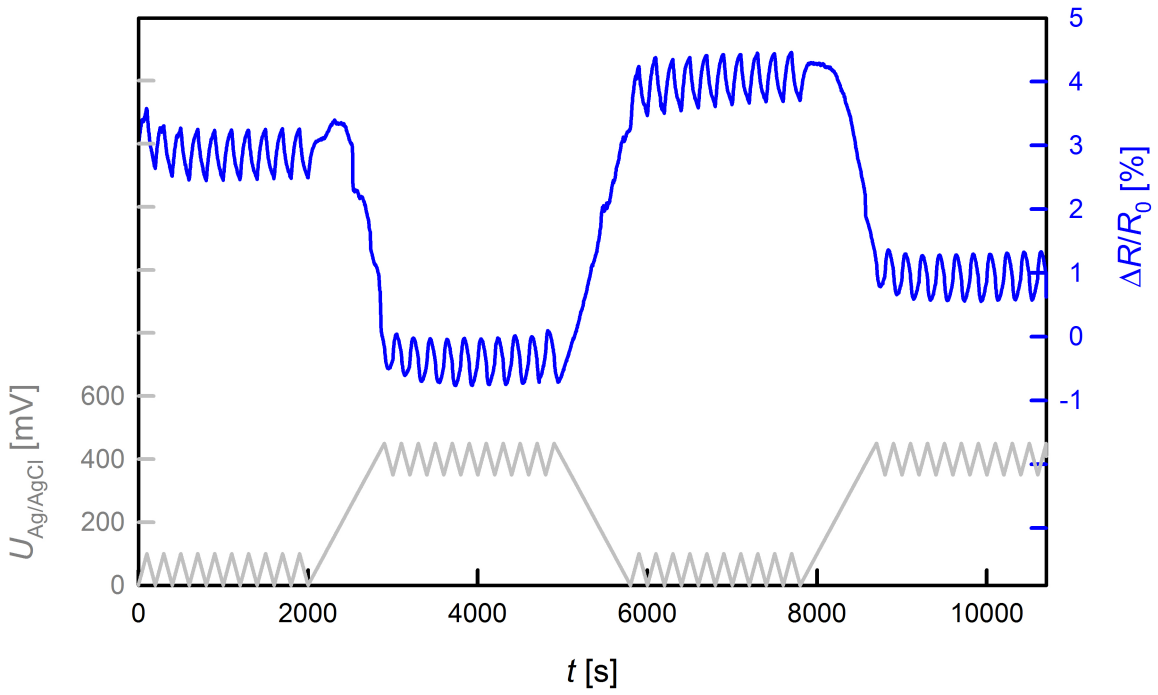

Figure 4.22: Resistance variation $\Delta R/R_0$ of np-Pt R4 upon charging procedures in 1 M KOH, recorded with a scan rate of 1 mV/s in different potential ranges in the primary oxide regime. The R-behavior is reversibly switched between positive and negative sign of charge coefficient.

cycling procedures in the primary oxide regime at potentials $U_{Ag/AgCl}$ between 0 mV and +450 mV, this hump completely disappears (middle curve, dashed). Obviously, in this aged condition, the variation of R in the entire scan range resembles that typical for the upper potential edge of a freshly dealloyed sample, namely a negative charge coefficiant of R and thus a resistance decrease (increase) with increasing (decreasing) potential.

The aging effect clearly demonstrates that the transition to a negative charge coefficient is related to the oxidation of the sample, which increases upon prolonged exposure to high potentials. This becomes even more obvious by the fact, that the initial $\Delta R/R_0$ behavior can be recovered (bottom curve), when the oxygen is partially removed (without damaging the sample) by keeping the sample at a low negative voltage of -50 mV for several hours.

A different kind of regeneration can also be achieved for samples in well-reduced condition: the fundamentally different behavior of the primary oxide can be restored, when a

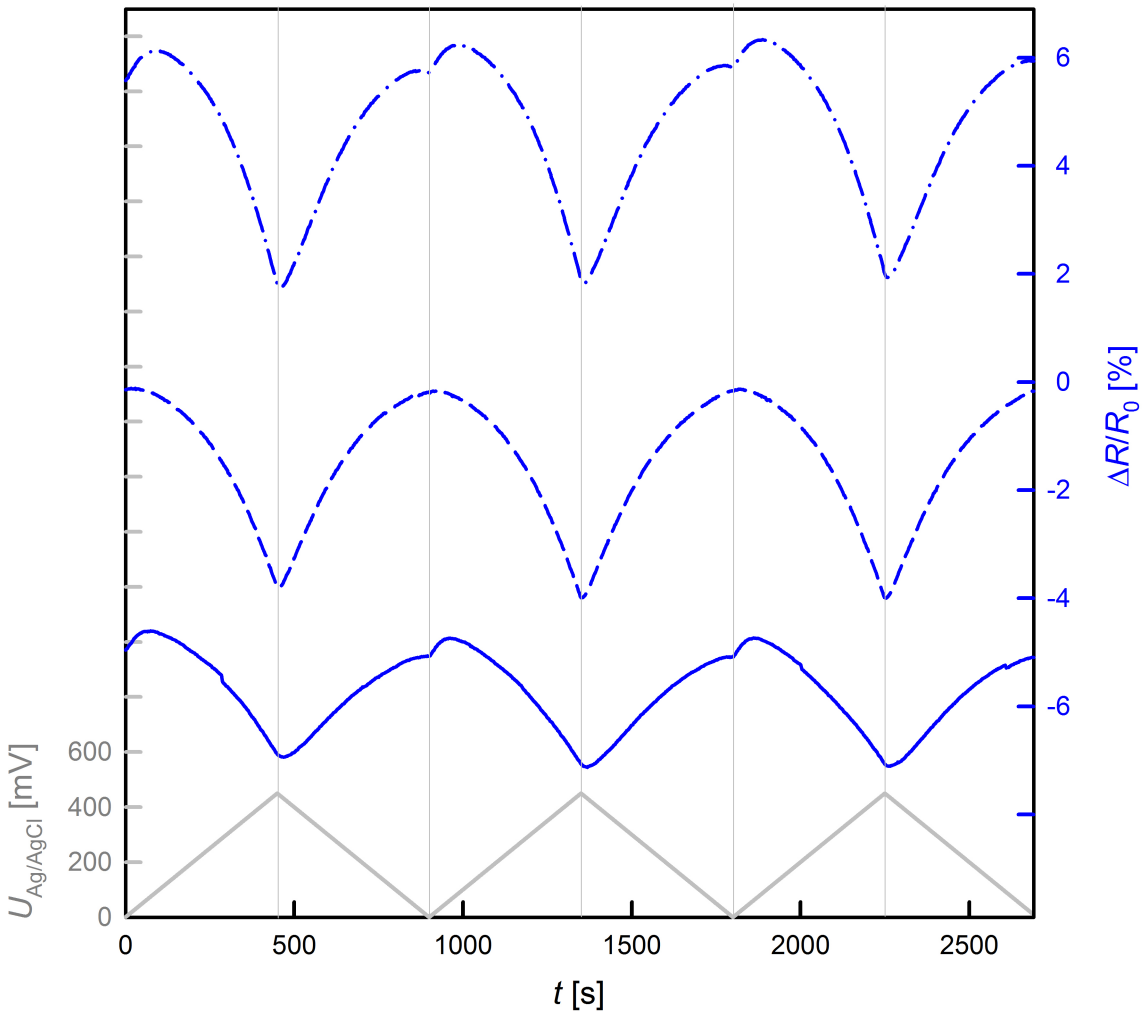

Figure 4.23: Aging behavior of the $\Delta R/R_0$-variation upon cyclic voltammetry in 1 M KOH with a scan rate of 1 mV/s between 0 mV and +450 mV shown for np-Pt R5. Applied potential $U_{Ag/AgCl}$ (gray) and resistance variation curves $\Delta R/R_0$ (blue) are plotted as a function of time. $\Delta R/R_0$ curves present: freshly dealloyed condition (top, dash-dotted); aged sample after various charging between 0 mV and +450 mV (middle, dashed); regeneration of initial state after keeping at −50 mV for several hours (bottom, solid).

previously reduced sample is held at strongly oxidizing potentials for a long time. Figure 4.24 shows the resistance variations of sample np-Pt R2, which had undergone a removal of the primary oxide and a subsequent oxidation treatment by holding the sample at a potential $U_{Ag/AgCl}$=+450 mV for 12 hours. From the charge flow of about 28 As, which was measured during this anodic charging procedure, a transfer of 0.7 oxygen species per platinum atom

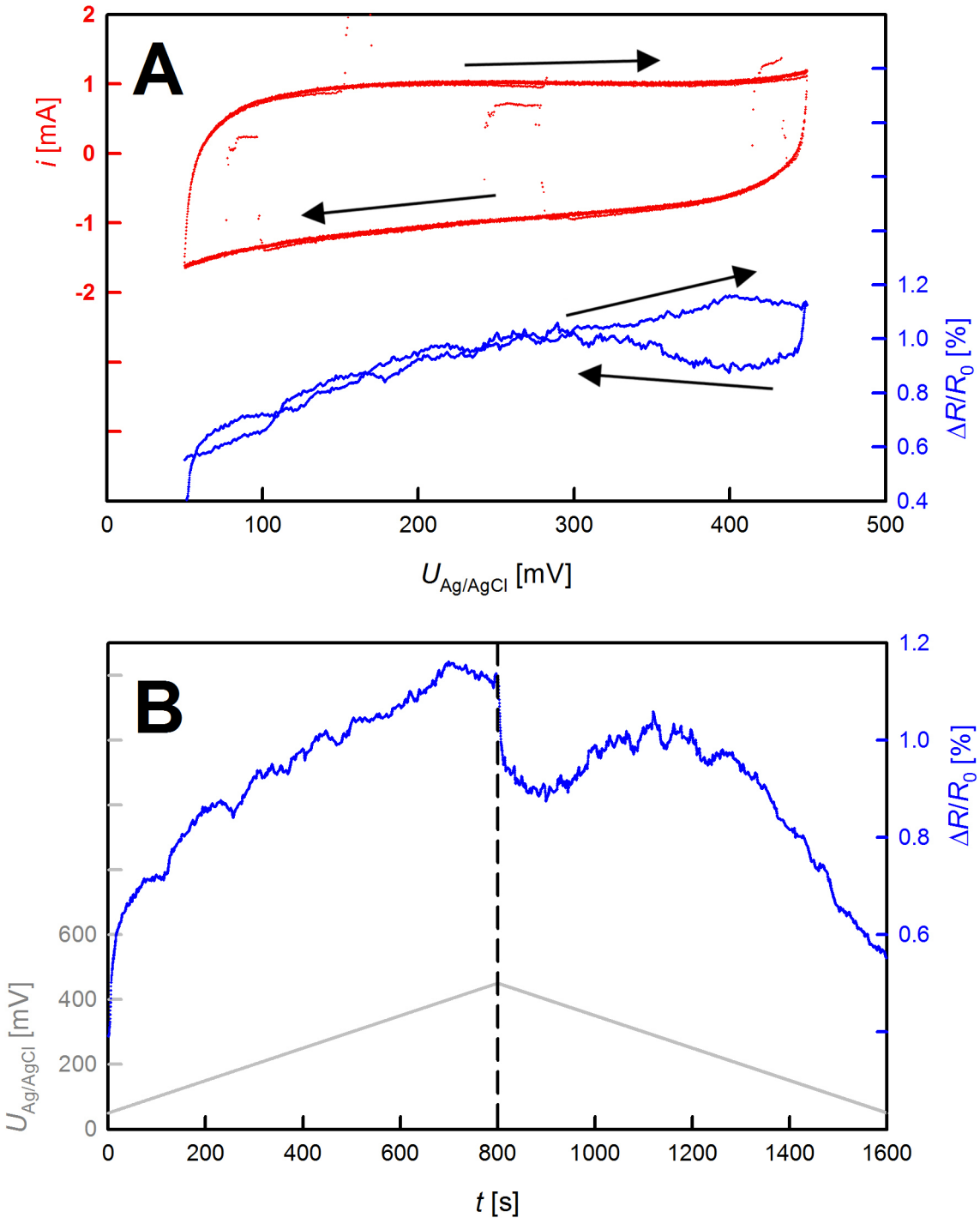

Figure 4.24: Resistance variation $\Delta R/R_0$ of np-Pt R2 after re-oxidation for 12 h at +450 mV in 1 M KOH (following primary oxide reduction). CV is restricted to the potential regime (+50 mV to +450 mV) in which oxygen desorption is avoided (scan rate of 0.1 mV/s). The reference value R_0 refers to the sample resistance after re-oxidation. (A) Current i (red) and $\Delta R/R_0$ as a function of potential $U_{Ag/AgCl}$. (B) Variation of $\Delta R/R_0$ and $U_{Ag/AgCl}$ as a function of time.

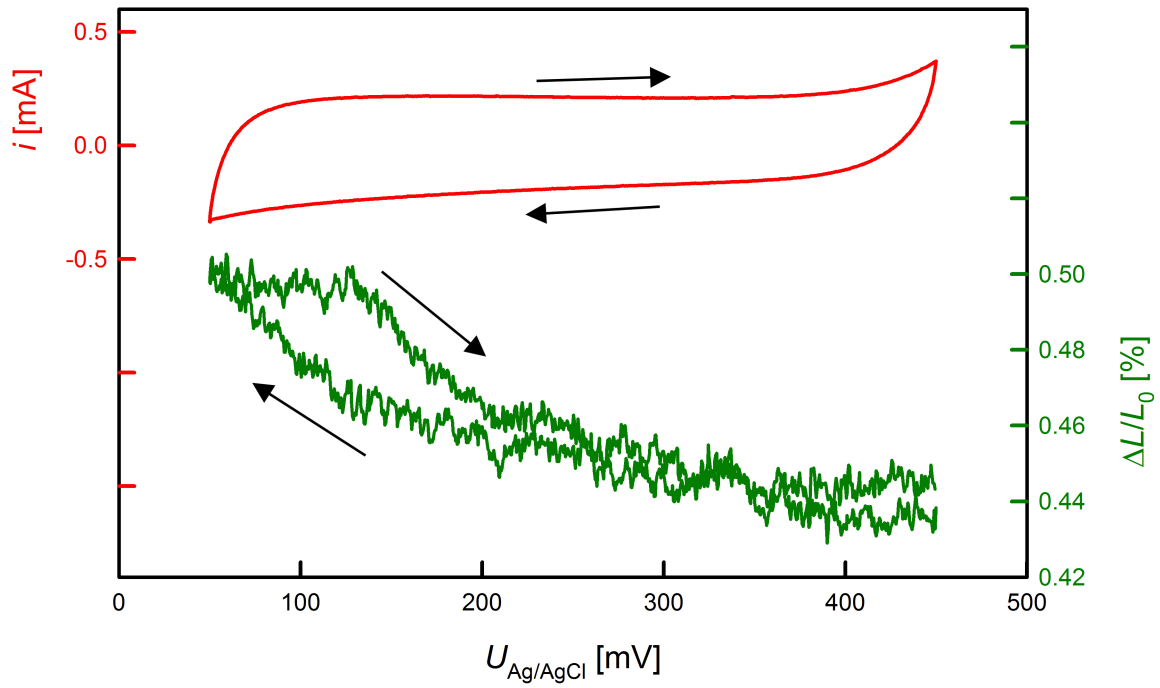

Figure 4.25: Thickness variations $\Delta L/L_0$ of np- Pt D1 after re-oxidation for 12 h at +450 mV in 1 M KOH (following primary oxide reduction). CV is restricted to the potential regime (+50 mV to +450 mV) above which oxygen desorption is avoided (scan rate of 0.1 mV/s). Current i (red) and $\Delta L/L_0$ are plotted as a function of applied potential $U_{Ag/AgCl}$.

can be approximated.

After the re-oxidation process, a resistance about twice as high was measured at open circuit potential. Obviously, both the degree of oxidation and the associated resistance increase do not reach the condition of a freshly dealloyed sample. Nevertheless, the particular charging-induced resistance variation (CV range between +50 mV and +450 mV) with the characteristic sign inversion of $\Delta R/R_0$ could be recovered by the oxidation treatment (compare figures 4.24 and 4.17).

Such a re-oxidation also restores the charging-induced thickness-variations, characteristic for the as-dealloyed state presented above in figure 4.18. Sample npPt D1 was subjected to primary oxide reduction and re-oxidation similar to np-Pt R2. After this procedure, the sample exhibited an actuation behavior similar to the primary oxide, thus a thickness

decrease (increase) upon increasing (decreasing) potential as shown in figure 4.25.

4.2.3 Palladium

Following the successful experiments on platinum, investigations were also conducted on dealloying and tunable properties of nanoporous palladium (np-Pd), which is particularly interesting due to palladium's ability to absorb hydrogen into the bulk. The essential findings were published in the Beilstein Journal of Nanotechnology, thematic series *Advances in Nanomaterials II*, which is listed as reference [31] in this thesis.

An overview over the property variations of well-reduced nanoporous palladium is given in figure 4.26. In the presented cyclic voltammograms (CV current shown in subplot A), performed in 1 M KOH with a scan rate of 1 mV/s between -1000 mV and +400 mV versus the reference electrode, a potential range again chosen in order to avoid strong gas evolution, the variations of resistance (B) and sample thickness (C) of np-Pd were recorded as a function of applied potential $U_{Ag/AgCl}$.

In the double layer and oxygen regime (potentials between −1000 mV and +400 mV) the property variations are similar to the observations presented above. The hydrogen regime, situated at potentials between −1000 mV and −550 mV, however, is associated with stronger property variations than observed for platinum due to Pd's ability of H-absorption into the bulk: resistance variations $\Delta R/R_0$ of approximately 7 % and a thickness increase $\Delta L/L_0$ of about 0.5 % are observed in this potential range.

The hydrogen regime was investigated in more detail by cyclic voltammetry at a very slow scan rate of 0.1 mV/s. Figure 4.27 shows the relative variations of electrical resistance and sample thickness as functions of the imposed charge Q, determined by continuously integrating the charging current, corrected for minor leakages by subtracting a constant factor determined from the cycle-to-cycle offset. Resistance and length changes reveal remarkable similarities, both exhibiting two regions of different slope, attributed to hydrogen adsorption followed by hydrogen absorption at higher imposed charges.

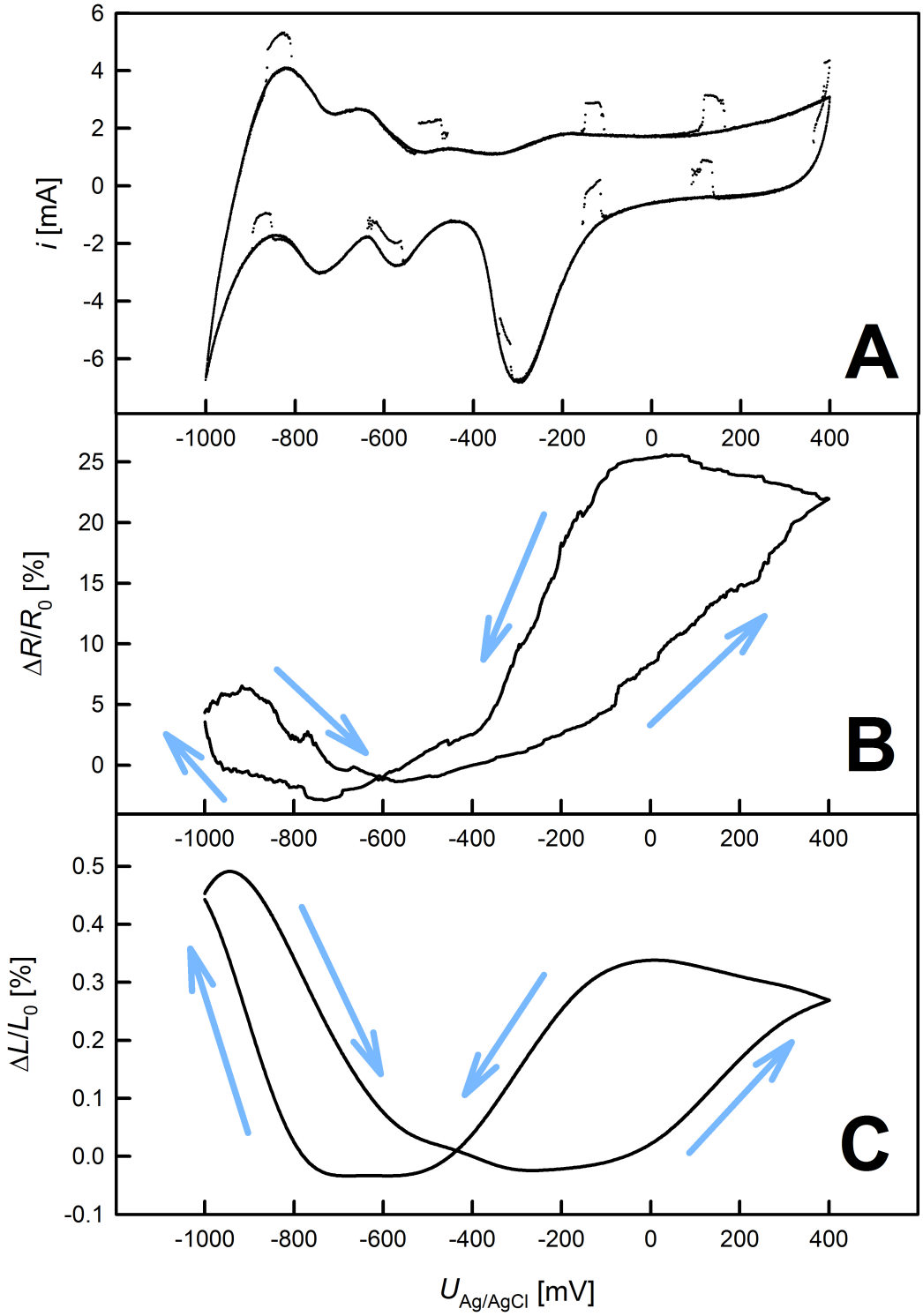

Figure 4.26: Cyclic voltammetry of np-Pd in 1 M KOH aqueous solution, recorded with a scan rate of 1 mV/s between potentials $U_{Ag/AgCl}$ of −1000 mV and +400 mV, shown for sample np-Pd R2 (A), with concommitant relative variations in electrical resistance of np-Pd R2 (B) and sample thickness of np-Pd D1 (C).

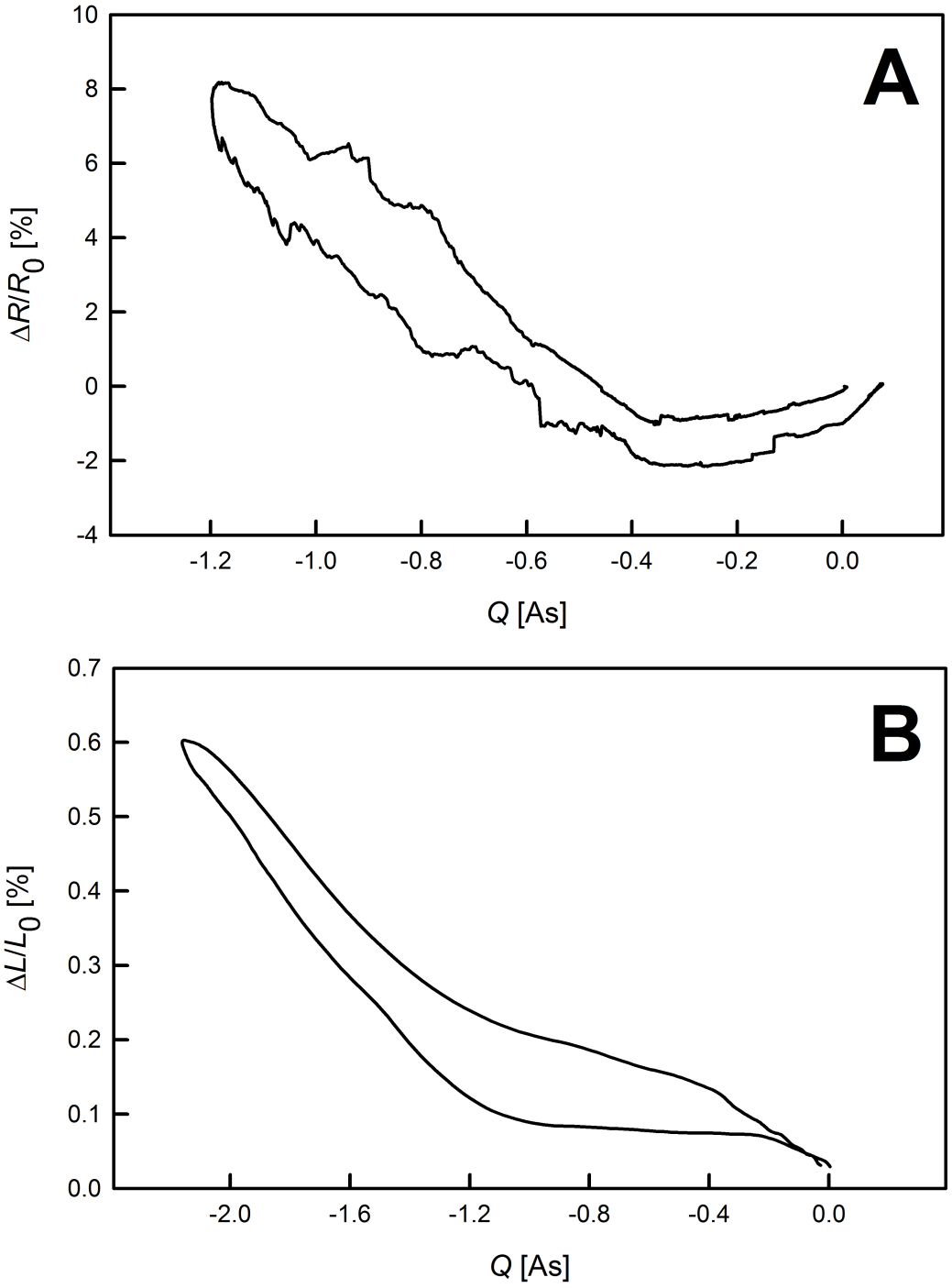

Figure 4.27: Charge dependence of relative electrical resistance of np-Pd R2 (A) and sample thickness of np-Pd D2 (B) upon cyclic voltammetry in the hydrogen regime, performed in 1 M KOH with a slow scan rate of 0.1 mV/s at potentials $U_{Ag/AgCl}$ between −1000 mV and −550 mV.

Table 4.4: Dilatometrically monitoring hydrogen absorption upon voltage-controlled charging procedures at quoted voltages $U_{Ag/AgCl}$ or current-controlled charging at quoted currents, resulting in a final H/Pd atomic ratio c_f associated with a final thickness increase $(\Delta L)_f/L_0$.

parameters	time [min]	c_f	$(\Delta L)_f/L_0$ [%]
−900 mV	60	0.12	0.49
	120	0.11	0.42
−950 mV	60	0.14	0.54
	120	0.14	0.55
−1000 mV	60	0.35	2.90
	120	0.45	4.05
−1050 mV	60	0.51	4.71
	120	0.57	5.11
−5 mA	60	0.58	5.35
−2 mA	150	0.58	5.06

Since extraordinarily strong actuation properties were reported quite recently for np-Pd produced by free corrosion [96], the dilatometric measurements were extended to higher hydrogen concentrations by employing different charging parameters, which are listed in table 4.4. Before each loading experiment, the sample was activated by a CV similar to figure 4.26. Hydrogen was absorbed either voltage-controlled at constant potentials $U_{Ag/AgCl}$ between −900 mV and −1050 mV, or current-controlled by applying a constant current, and in both cases subsequently desorbed at a constant potential of −400 mV for 120 min. The stored amount of hydrogen was determined by integrating the current recorded upon discharging.

The length changes measured along with the hydrogen charging are plotted in figure 4.28. Upon charging to a H/Pd atomic ratio of almost 60 %, a thickness increase of about 5 % was observed, representing the highest electrochemically induced actuation reported for a dealloyed material so far.

Like already presented above for nanoporous platinum, also freshly dealloyed np-Pd possesses a primary oxide, thus an as-dealloyed condition with peculiar properties, that strongly differ from those presented above for well-reduced np-Pd samples (figures 4.26 to 4.28). Due to serious contacting issues with primary oxidized Pd, unfortunately no valid resistance tunig

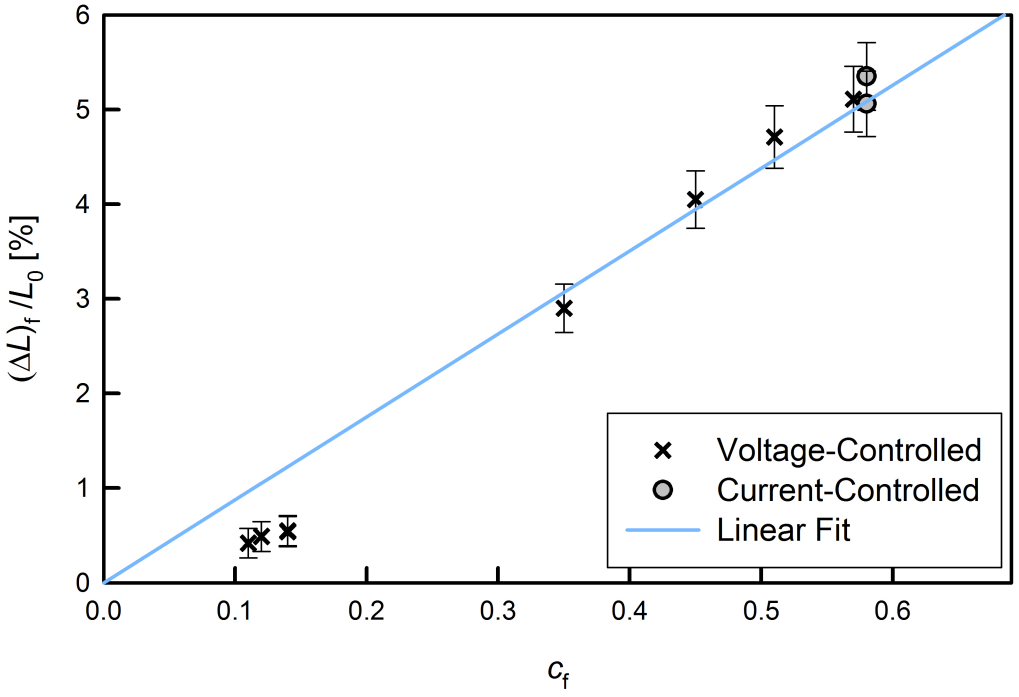

Figure 4.28: Thickness variations $(\Delta L)_f/L_0$ of sample np-Pd D1 upon loading experiments up to different final hydrogen concentrations, characterized by a final H/Pd atomic ratio c_f (see table 4.4)

data of samples in as-dealloyed condition could be collected in this work, since resistometric measurements, as described above, require 5 electrical contacts attached to the sample which could not be maintained connected stable during the experiments. Therefore the characterization of the primary oxide had to be restricted to dilatometric measurements, which is presented for sample np-Pd D3 as a cyclic voltammogram performed in 1 M KOH, shown in figure 4.29. While the applied potential $U_{Ag/AgCl}$ is varied with a scan rate of 1 mV/s between −100 mV and +400 mV, representing the regime of pseudocapacitively charging the primary oxide, avoiding oxygen desorption, the sample thickness changes with a negative charge coefficient. This contraction (expansion) of the sample upon positive (negative) scan again represents an opposite sign behavior compared to the well reduced condition (compare figures 4.26 and 4.29), similar to the observations for np-Pt presented above in section 4.2.2.

For comparison, resistance tuning experiments were also performed with palladium nano-

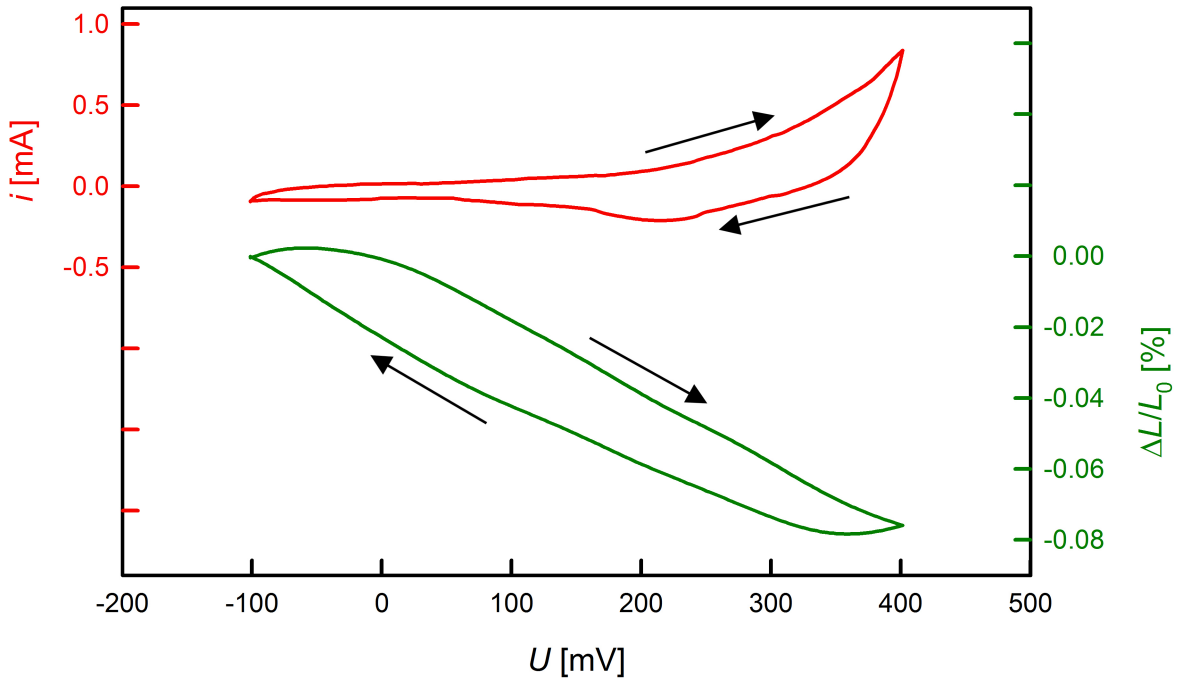

Figure 4.29: Relative thickness variation $\Delta L/L_0$ of the primary-oxide-covered sample np-Pd D3 upon CV between -100 mV and $+400$ mV, where the primary oxide is retained, measured with a scan rate of 1 mV/s. The reference value L_0 refers to the sample thickness at the lower potential edge. Current i (red) and $\Delta L/L_0$ (green) are plotted as a function of $U_{Ag/AgCl}$.

powder, produced by inert gas condensation. Figure 4.30 shows a cyclic voltammogram (red) in 1 M KOH aqueous solution, which was recorded for a 90 mg nanopowder pellet nc-Pd after compaction into a PTFE groove as described in section 3.2. The measurement was performed with a scan rate of 1 mV/s at potentials $U_{Ag/AgCl}$ between -900 mV and $+400$ mV. The concomitant resistance variations, plotted as a blue curve in figure 4.30, are qualitatively of simliar shape as those obtained for np-Pd (compare figure 4.26), however of significantly lower magnitude (reduced by about a factor of 2). This superior tunability of np-Pd as well as the higher observed currents, relative to the sample mass, can both be attributed to the extraordinarily high surface-to-volume ratio of nanoporous palladium produced by dealloying.

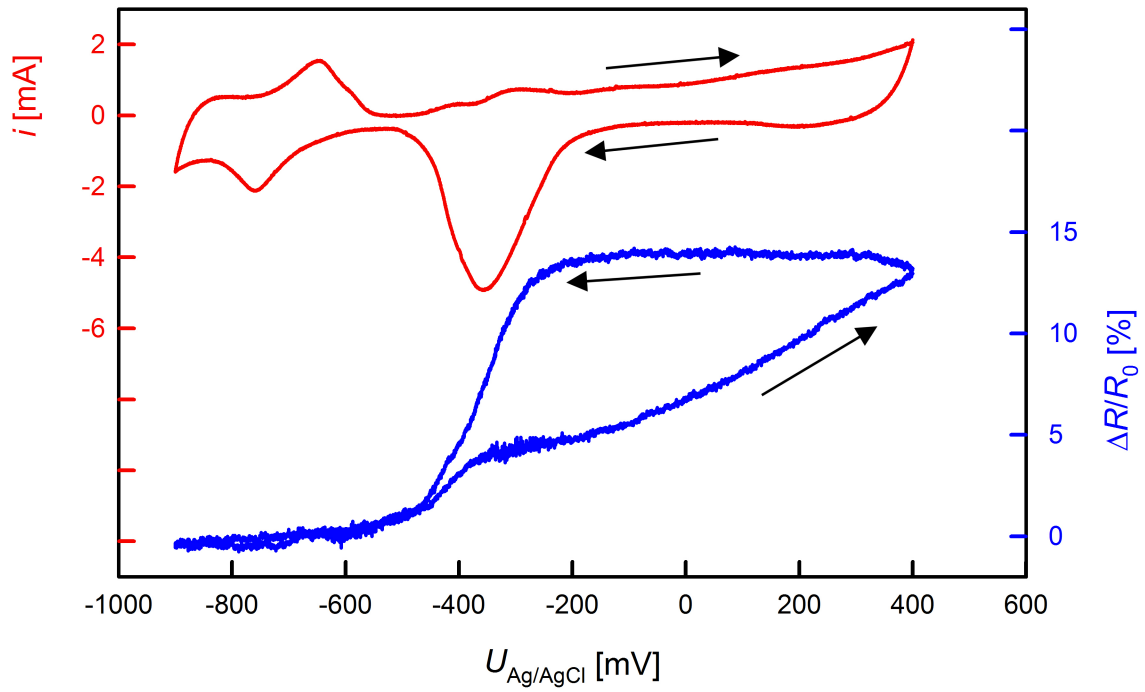

Figure 4.30: Resistance variation $\Delta R/R_0$ of sample nc-Pd upon CV at potentials $U_{Ag/AgCl}$ between -900 mV and $+400$ mV, investigated with a scan rate of 1 mV/s. The reference value R_0 refers to the sample resistance in the double layer regime at -550 mV. Current i (red) and $\Delta R/R_0$ (blue) are plotted as a function of $U_{Ag/AgCl}$.

4.2.4 Gold

As already mentioned above, during my work I had the opportunity to co-supervise experiments on nanoporous gold, which were conducted in the master thesis of Michael Seidl. Even though the focus of his master thesis was placed on the dealloying process itself, and in particular the resistance increase of samples during selective etching, also interesting results regarding the tunable resistance of nanoporous gold could be obtained with the dealloyed gold nanostructures. All measurements presented here were performed with one single nanoporous gold platelet, indexed as np-Au R1, with an initial mass of 86 mg.

Figure 4.31 shows a cyclic voltammetry curve, recorded with a scan rate of 1 mV/s in 1 M KOH aqueous solution. The potential range was limited to -400 mV up to $+800$ mV, in order to avoid gas evolution. Also for this system, the first CV cycle, plotted as a red curve,

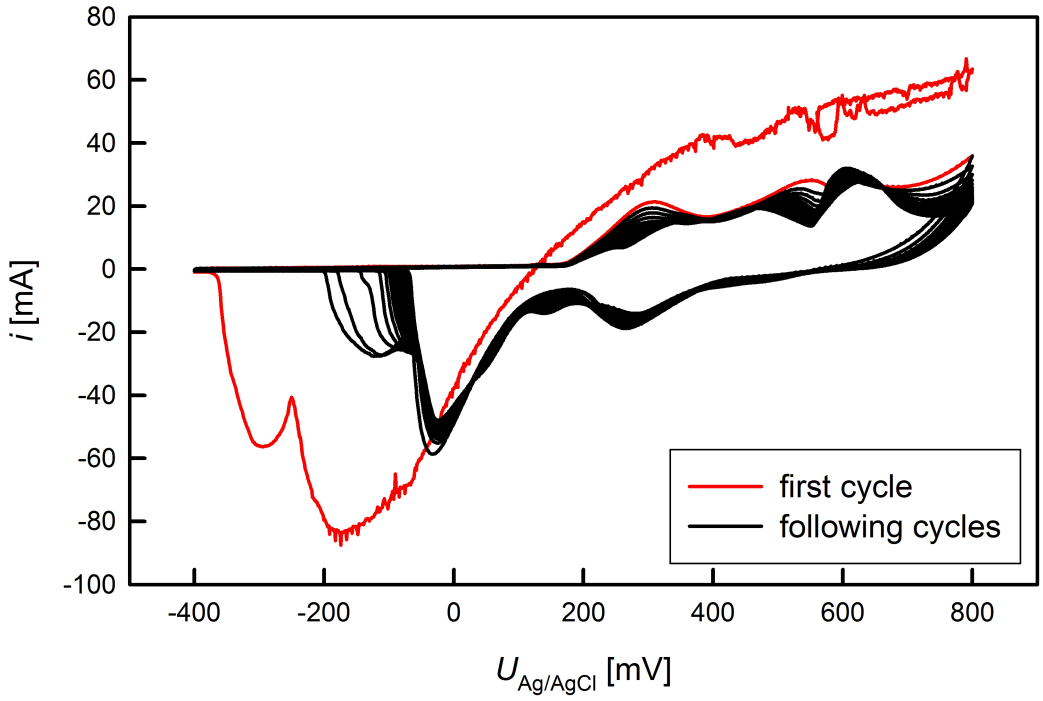

Figure 4.31: Cyclic voltammetry of freshly dealloyed sample np-Au R1, performed with a scan rate of 1 mV/s in 1 M KOH solution. The current i is plotted as a function of $U_{Ag/AgCl}$. In the first cycle (red) stripping of the strongly bound primary oxide can be observed, in the following cycles (black) the curve approaches steady state.

strongly differs from the following ones, exhibiting a stronger oxygen desorption peak which is shifted to more negative potentials. Again, this behavior can be assigned to the reduction of a primary oxide, formed during the dealloying process. During the following five cycles, which are plotted in black, the CV approaches a steady state.

Monitoring the sample resistance during a steady state cyclic voltammogram with this parameters gives the behavior presented in figure 4.32. The resistance exhibits an extraordinarily strong variation up to almost 90 % upon oxygen adsorption and desorption, representing the highest value achieved for a dealloyed metal so far. At the same time it also shows a drift towards higher overall values, which arises most likely due to a slight degradation with damages emerging in the fragile nanoporous network. The excellent tunability observed here for nanoporous gold should be considered a preliminary result and has not yet been subject

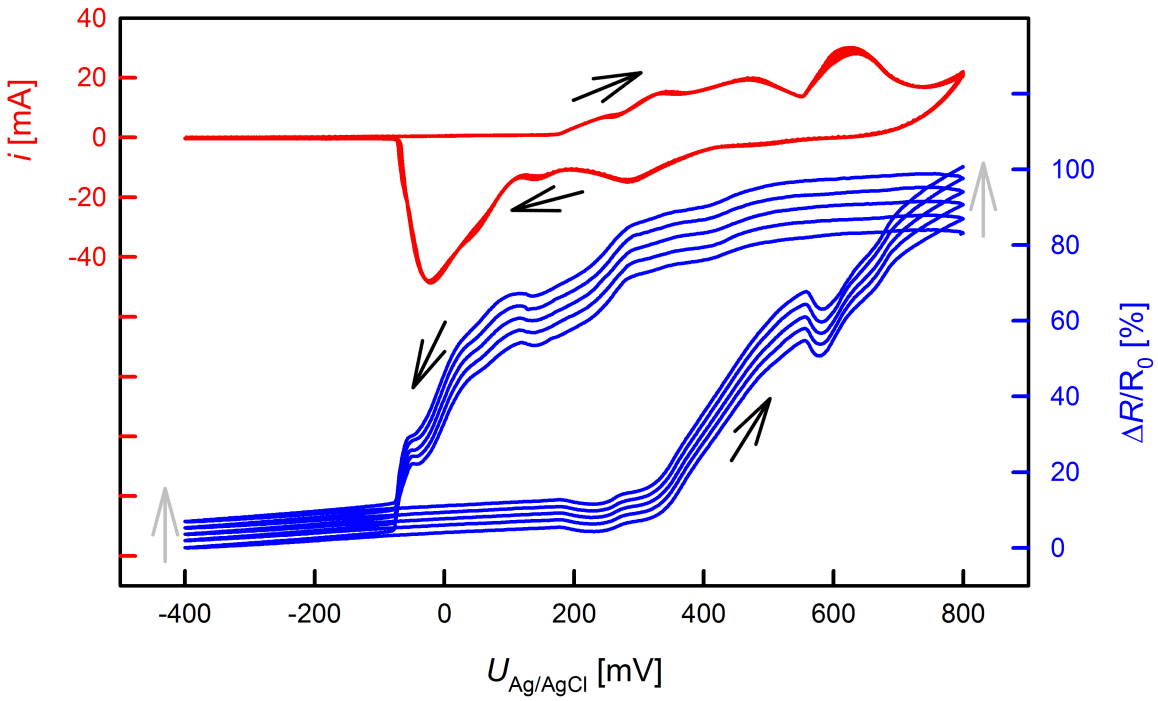

Figure 4.32: Steady state CV (red) and concomitant resistance variations $\Delta R/R_0$ (blue) of sample np-Au R1, measured in 1 M KOH aqueous solution with a scan rate of 1 mV/s at potentials $U_{Ag/AgCl}$ limited to the range −400 mV and +800 mV, in order to avoid gas evolution. R_0 refers to the sample resistance at the lower potential edge.

of detailed investigations. The high sensitivity to charging may arise due to the very small specific resistance of gold, however also an influence of residual silver from the dealloying process cannot be excluded completely at this point (see chapter 5.2). Systematic studies of the $\Delta R/R_0$ variations on this promising system should be performed in the future.

4.3 Structural and Chemical Characterization of np-Pt

This section is a collection of further investigations, performed on nanoporous platinum in order to obtain a more detailed characterization of the sample material. Most of them represent electron microscopical images (SEM and TEM) of different sample conditions, partially complemented by EDX analysis. In addition XPS as well as XRD measurements, both performed to study the primary oxide of np-Pt, will be presented.

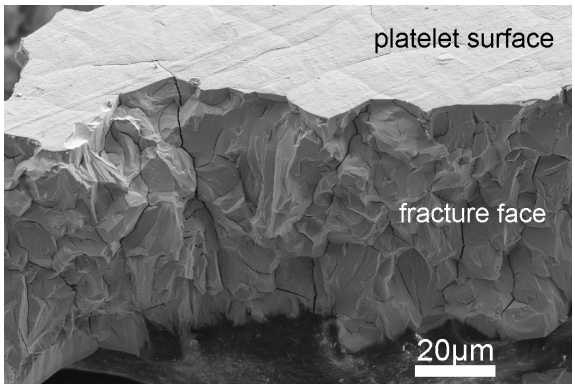

Figure 4.33: Overview SEM micrograph of a fractured np-Pt sample platelet in as-dealloyed condition, mounted on electrically conductive adhesive tape.

All SEM micrographs presented in the following figures were recorded by Prof. Peter Pölt at the FELMI-ZFE. Figure 4.33 shows as overview a low magnification image of a fractured np-Pt platelet in as-dealloyed condition (covered by primary oxide). For microscopy the sample was mounted on electrically conductive adhesive tape. While the surface of the platelet looks rather smooth, the extreme brittleness of the sample material is clearly illustrated by the multiply faceted fracture face. Deep cracks, running through the sample, appear where the grain boundaries used to be located in the master alloy.

Figures 4.34 and 4.35 present more details for this freshly dealloyed sample. Facing the platelet surface with a more direct angle and higher magnification, the cracks representing the grain boundaries can also be recognized at the surface, which is shown in figure 4.34 (left). Several pores in a size range of tens of nanometers are visible, which yet cannot account for

Table 4.5: EDX analysis of np-Pt in as-dealloyed condition (primary oxide), performed at different spots of the sample. The relative amounts of oxygen, copper and platinum are given in atomic percent.

element	platelet surface (Figure 4.34) c [at%]	fracture face (Figure 4.35) c [at%]
O	49.8	45.7
Cu	7.4	7.4
Pt	42.8	46.9

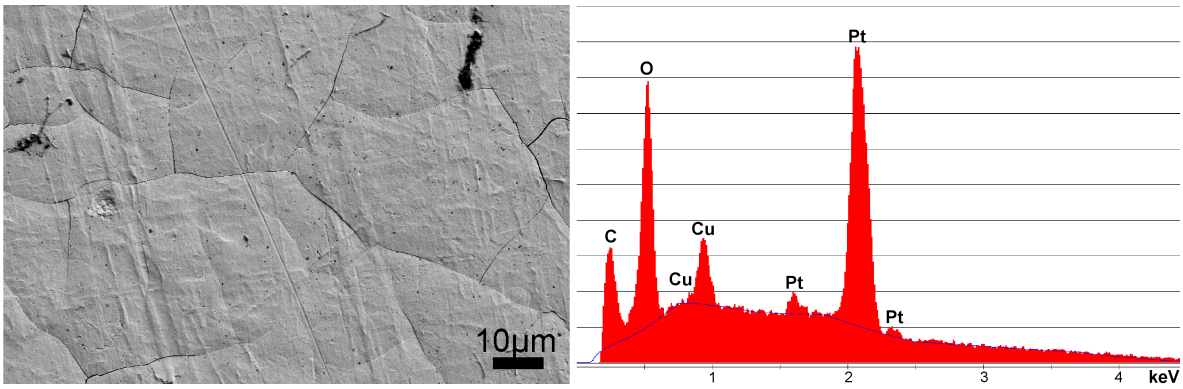

Figure 4.34: SEM micrograph (left) and EDX spectrum (right) taken on the surface of an np-Pt platelet in as-dealloyed condition.

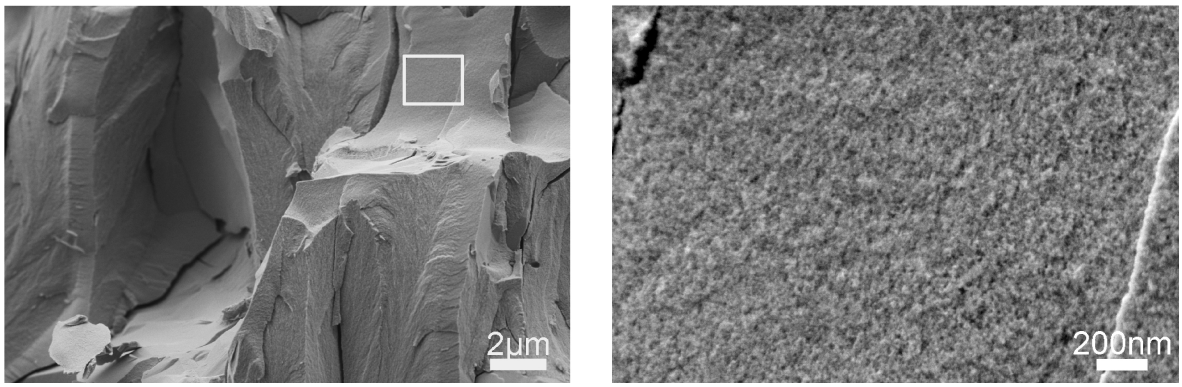

Figure 4.35: SEM micrographs of the fracture face of an np-Pt platelet in as-dealloyed condition. The highlighted area in the left micrograph is shown in higher magnification on the right.

the extraordinary high surface to volume ratio of the samples determined electrochemically. However no evidence for fine porosity can be found in SEM images of the sample surface. An EDX spectrum of the sample surface area shown in the micrograph is plotted on the right side of figure 4.34. The corresponding relative atomic ratios of platinum, oxygen and copper are listed in table 4.5, showing a high degree of oxidation amounting to a value of about one oxygen species per platinum atom as well as a small amount of residual copper, which wasn't removed successfully during the dealloying process.

Very similar EDX data, which are also listed in table 4.5 were collected at the fracture face (spectrum not shown), confirming a good homogeneity of the successfully etched sample in final condition. The micrograph of the corresponding fracture face area is presented in

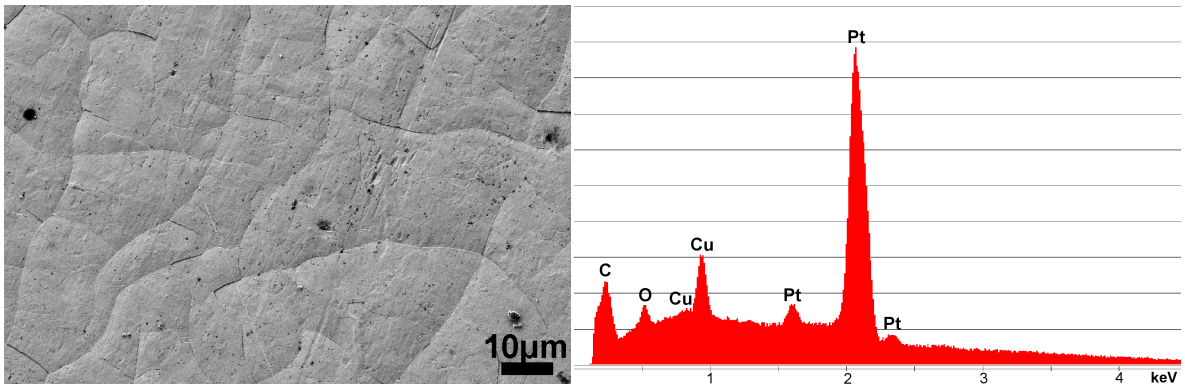

Figure 4.36: SEM micrograph (left) and EDX spectrum (right) taken on the surface of a well-reduced np-Pt platelet.

figure 4.35 (left). At high magnifications, as shown on the right side of figure 4.35, the fracture face appears rough and possibly porous, however no estimation of structural sizes can be given based on the present SEM images due to the limited resolution.

Figure 4.36 shows the micrograph of a well-reduced sample surface, taken at the same magnification as used for the primary oxidized sample in figure 4.34. Comparing the images of the two sample surfaces in different conditions, they look very simliar, however, the cracks appear deeper and in a higher number for the well-reduced sample, indicating the material suffered further damages due to the electrochemical reduction process. The EDX spectrum of the well-reduced sample on the other hand reveals more significant differences compared to the primary oxide: While the platinum and copper signals as well as the carbon impurities are similar in both measurements, the oxygen peak, which is strongly pronounced for the as-dealloyed sample, almost vanished in this spectrum recorded at the well-reduced surface.

Due to the fine porosity of nanoporous platinum, detailed structural investigations, and in particular a determination of the ligament and pore sizes, require TEM studies of the sample material, which were performed by Dr. Mihaela Albu at the FELMI-ZFE. Figures 4.37 and 4.38 show TEM images of np-Pt samples in primary oxide and well-reduced condition respectively. Both samples were prepared for microscopy by grinding the brittle np-Pt platelets into a fine powder which was then applied to a copper grid. Since the samples in both images reveal similar features, the reduction of the stabilizing primary oxide does ob-

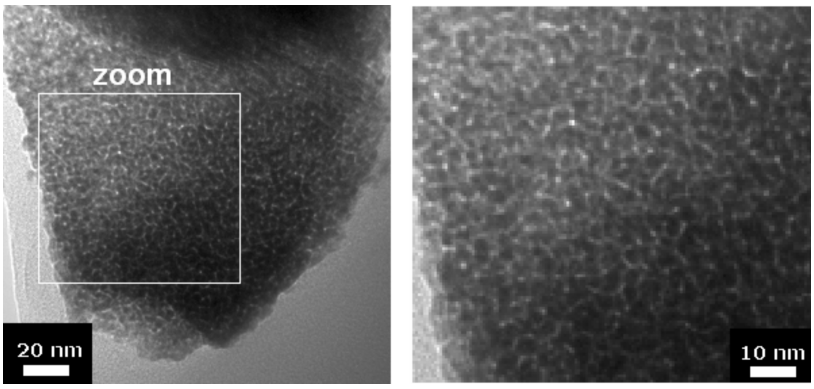

Figure 4.37: TEM micrographs of np-Pt in as-dealloyed condition, prepared for microscopy by grinding. The highlighted area in the left micrograph is shown in higher magnification on the right.

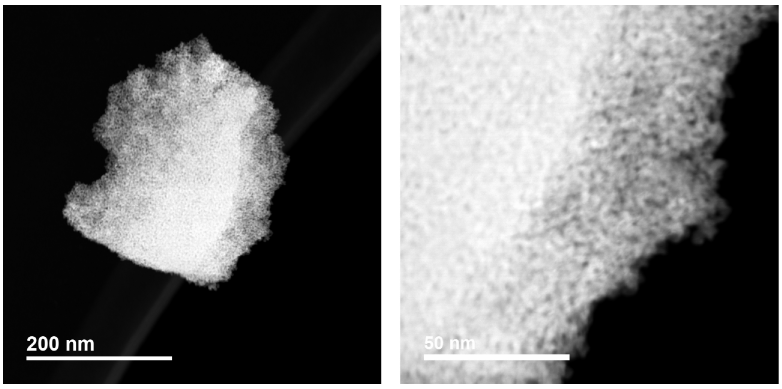

Figure 4.38: TEM micrographs of well-reduced np-Pt in different magnifications. The sample was prepared for microscopy by grinding.

viously not lead to significant alterations of the structural sizes in the nanoporous network, which is probably due to the high melting point and therefore limited diffusivity of platinum.

An enhanced resolution can be obtained by an alternative method of sample preparation: Figure 4.39 shows two micrographs that were taken from a well-reduced nanoporous platinum sample which had beed embedded in epoxy resin and subsequently been cut in slices of suitable thickness by a microtome. The TEM investigations reveal pore sizes in the range of 1-2 nm and ligament diameters of 3-5 nm.

The np-Pt sample embedded in epoxy resin was also subjected to EDX analysis, which is presented in figure 4.40 and table 4.6. Even though the analysis presented here is by far more detailed, the major findings are well in line with the EDX data collected during SEM

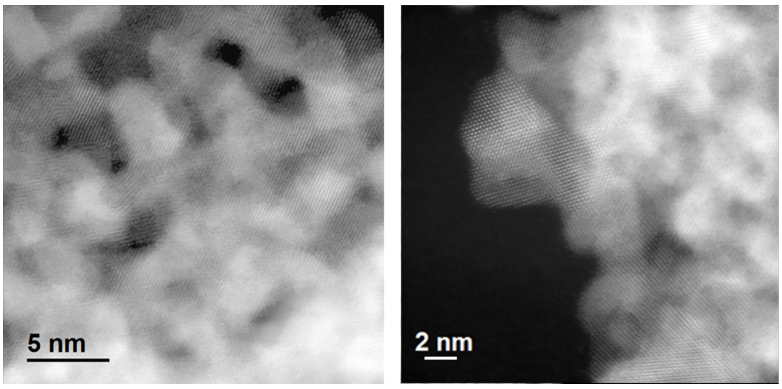

Figure 4.39: TEM micrographs of well-reduced np-Pt, embedded in epoxy resin, prepared for microscopy by microtome cutting.

Table 4.6: EDX analysis of well-reduced np-Pt, embedded in epoxy resin, prepared for microscopy by microtome cutting. The relative amounts of copper and platinum in the structure are given in atomic percent.

element	c [at%]
Cu	11.7
Pt	88.3

measurements for samples in primary oxide condition (see figure 4.35 and table 4.5), showing a small but clearly detectable amount of residual copper in the nanoporous structure.

For a selected ligament, which is highlighted by a green frame in the TEM image in figure 4.40, an EDX map was recorded. Below the micrograph, the elemental maps for the relative Pt (left) and Cu (right) concentrations are shown as two square-shaped pixel-areas. Each pixel represents an EDX measurement point, the gray-scales give the relative concentration of the respective element from 0 % (black) to 100 % (white). Both elements appear to be distributed uniformly over the entire ligament diameter, which is in clear contrast to results presented for nanoporous gold in the literature [13], where a strong enrichment of the more noble component was found near the ligament surfaces. The reason for this difference might lie in the very small ligament size of np-Pt.

When nanoporous samples are subjected to heat treatment, the enhanced diffusivity of the atoms leads to a coarsening of the nonequilibrium structure produced by dealloying. As

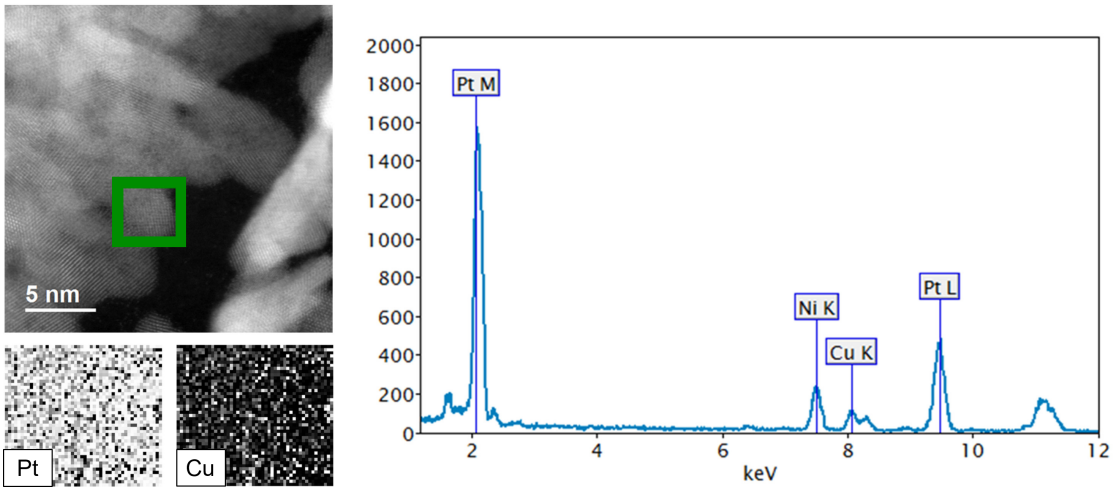

Figure 4.40: Left: TEM micrograph of well-reduced np-Pt, embedded in epoxy resin, prepared for microscopy by microtome cutting. The squares below show EDX maps scanning for platinum (left) and copper (right) in the highlighted area. Right: Averaged EDX spectrum of the highlighted area.

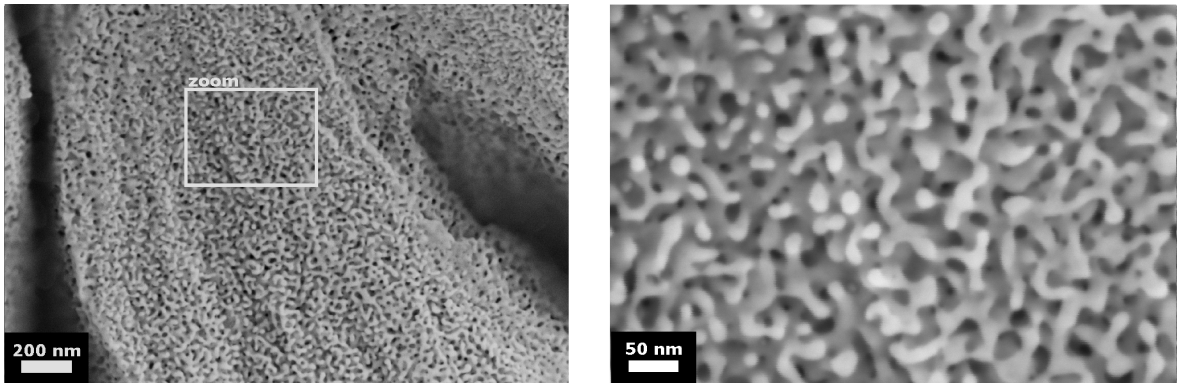

Figure 4.41: SEM micrographs of a coarsened np-Pt sample revealing the high amount of free volume in the nanostructure. The highlighted area in the left micrograph is shown in higher magnification on the right.

a consequence, the structure can then easily be resolved also by SEM, clearly showing the high amount of free pore volumes in the dealloyed material, which is shown in figure 4.41[1].

As a further characterization of the primary oxide condition, np-Pt samples in as-dealloyed and well-reduced state were subjected to XRD- and XPS-analysis which is shown in figures 4.42 and 4.43. In primary oxide condition np-Pt appears x-ray amorphous, exhibiting no distinct peaks, which is confirmed by two independent scans (black and red) in

[1]shown for a sample exposed to elevated temperatures due to spontaneous heat release under uncontrolled conditions

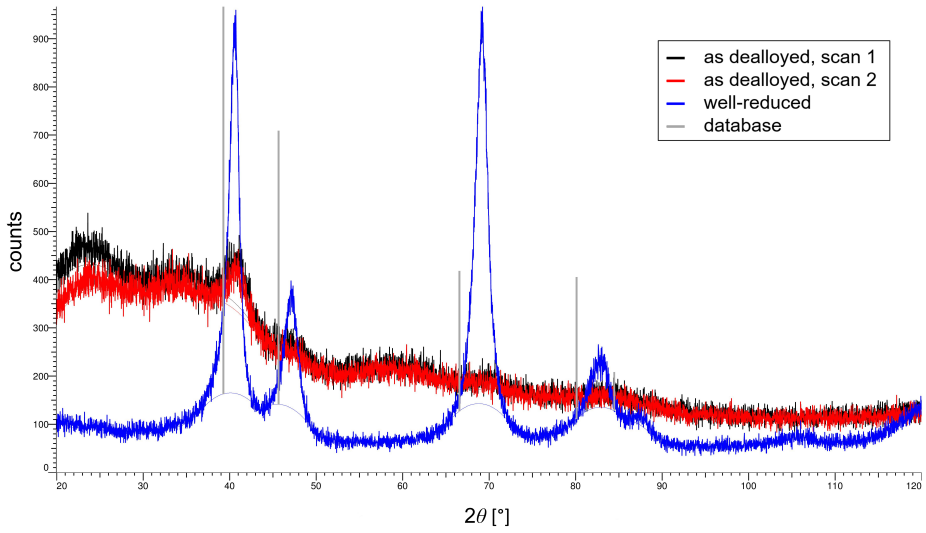

Figure 4.42: XRD analysis of np-Pt in different conditions. The black and red curve show two independet measurements of one np-Pt sample, both showing an x-ray amorphous behavior. The peaks emerging in the blue curve, showing the same sample after electrochemical reduction, are slightly shifted compared to the database spectrum of Pt (gray).

figure 4.42. XRD measurements after stripping the primary oxide off the sample indicate a rearrangement of the Pt structure: In the spectrum (blue), peaks emerge which show a clear correlation to the database values for platinum (gray). The obvious misfit between measured and database peak positions arises most likely due to the distorted shape of dealloyed platelets, especially after stripping the primary oxide, and also due to an unavoidable misfit upon mounting the brittle samples on the holder without applying pressure.

Also XPS spectra, which were recorded by Samantha Zimnik at the Technical University of Munich (FRM II), indicate the presence of a primary oxide (rather than an oxygen adsorbate): An overview spectrum of Pt is given in figure 4.43 for a reference sample (Pt foil). The nature of the present oxygen species can be determined from the O1s peak around 955 eV. Here no quantitative evaluation is given. However, while the O1s peaks recorded for the Pt foil (black) and the well-reduced np-Pt (blue) look very similar, both beeing assigned to adsorbed O-contamination, the O1s peak of the primary oxide (red), marked by a red dashed line, is stronger and shifted to the right, indicating a different nature of binding.

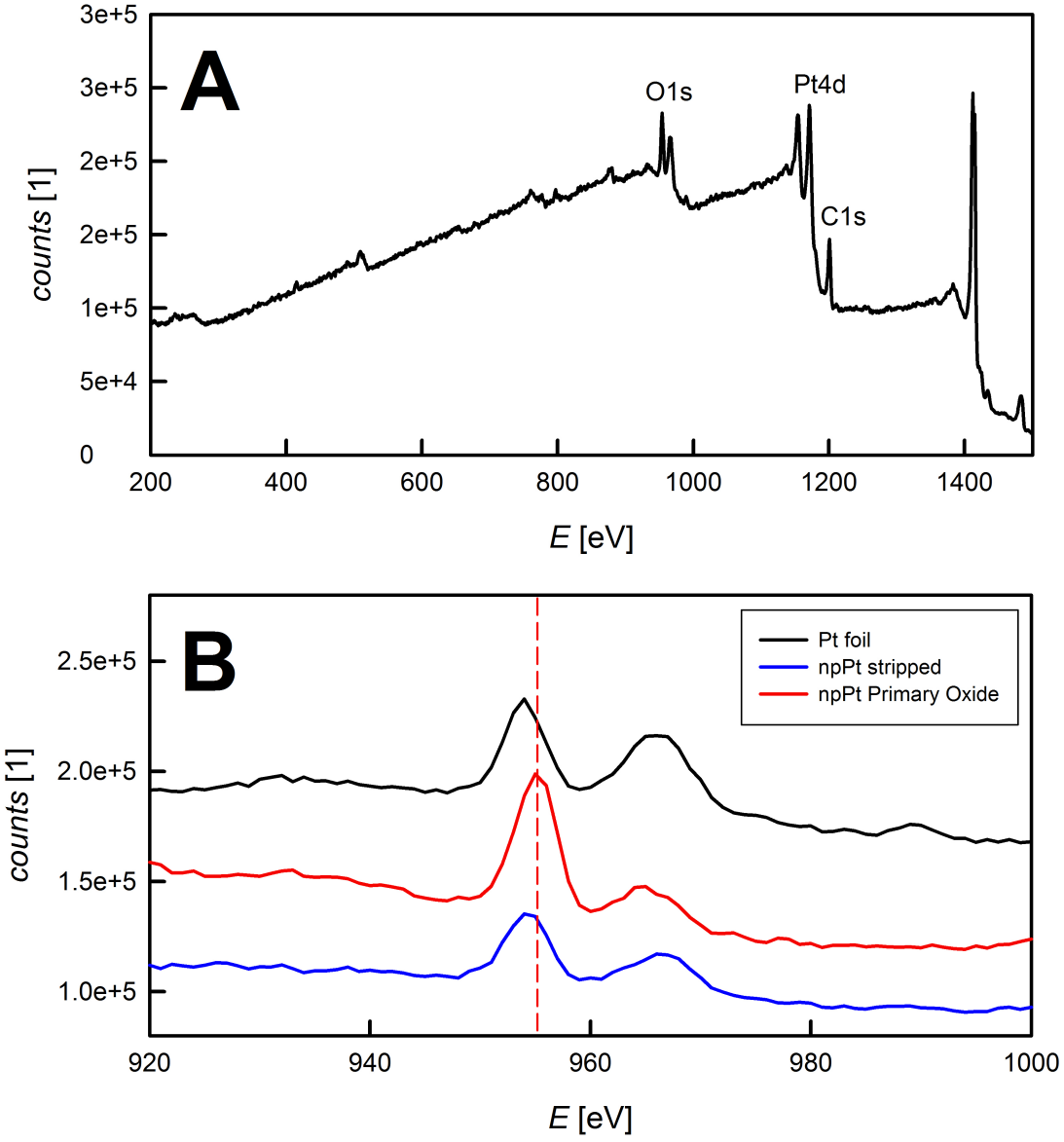

Figure 4.43: XPS study of the primary oxide of np-Pt. A: Overview XPS-spectrum of platinum, recorded for a Pt foil. B: Detailed investigation of the O1s peak for np-Pt in primary oxide (red) and stripped (blue) condition, compared to the Pt foil (black, shown in A) as reference value.

5 | Discussion

5.1 Resistometrical Model for Dealloying

Based on the experimental resistometry data, recorded during the formation of nanoporous gold, platinum and palladium (see chapter 4.1), a simple model capable of connecting the resistance increase and the dealloying charge flow was developed in the framework of this thesis.

During a dealloying experiment, the master alloy cross section decreases at the expense of the emerging porous network, which is illustrated in figure 5.1. The most simple attempt to describe the resistance of a sample during this process would be a parallel circuit of the master alloy backbone (index m) and the porous structure (index p), each characterized by the resistance

$$R_i = \rho_i \frac{l}{A_i} \qquad i : (m, p) \tag{5.1}$$

for a sample with the length l and cross-section A_i.

The experimental data presented in section 4.1 (figures 4.1 and 4.2) show, that the resistances of the samples increases by about three orders of magnitude during dealloying. Assuming no changes in external dimensions due to dealloying, the specific resistances ρ_i of the alloy and the porous structure differ by three orders of magnitude as well. Therefore, a parallel circuit of R_m and R_p, describing the overall sample resistance $R_{||}$, is dominated by

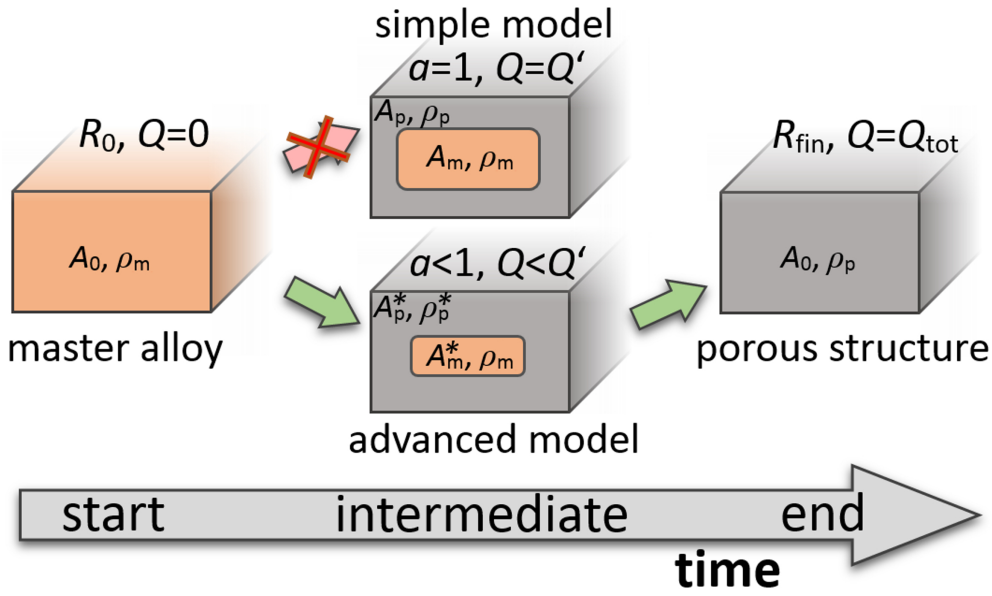

Figure 5.1: Illustration of the dealloying process of a sample with an initial cross section A_0 and resistance R_0. The sample platelet is presented in cross section view, with the notations used for the model. During the etching process the master alloy backbone (orange) shrinks in favor of the porous structure (gray), intermediate states are shown according to the simple and advanced approach discussed in the text. In final condition, associated with a charge flow Q_F and a resistance R_F, the entire cross section is porous.

the master alloy backbone over a wide range of the experiment:

$$\frac{1}{R_{||}} = \frac{1}{R_m} + \frac{1}{R_p} = \frac{1}{l}\left(\frac{A_m}{\rho_m} + \frac{A_p}{\rho_p}\right) \approx \frac{A_m}{l \cdot \rho_m}. \tag{5.2}$$

If we assume that the etching front propagates into the master alloy with an initial cross section A_0, leaving behind the nanoporous structure in its final state, the cross sections A_p and A_m at a given time during the etching process should simply be related to the charge Q' transferred up to this time, if slight volume shrinkages [114] due to dealloying are neglected, i.e.:

$$\frac{A_p}{A_0} = \frac{Q'}{Q_{tot}} \quad ; \quad \frac{A_m}{A_0} = 1 - \frac{Q'}{Q_{tot}}. \tag{5.3}$$

By using the resistances R_0 and R_{fin}, measured at the beginning/end of the etching process, in equation (5.1), the specific resistances can be substituted by $\rho_{m/p} \cdot l = R_{0/fin} \cdot A_0$,

leading to an expression of (5.2) which uses only measurement parameters:

$$R_{||}(Q') = \frac{R_0 R_{fin}}{R_0 \frac{Q'}{Q_{tot}} + R_{fin}(1 - \frac{Q'}{Q_{tot}})} \approx \frac{R_0}{(1 - \frac{Q'}{Q_{tot}})}. \tag{5.4}$$

In the approximation made on the right, the sample overall resistance is exclusively given by that of the master alloy backbone, which is valid as long as the conductance in the porous structure is negligible compared to the backbone.

Figure 5.2 shows the predicted resistance increase (red, dashed) according to equation (5.4) without using the approximation in comparison to the data recorded experimentally (black, solid) for np-Au R1 (the experimental resistometry data were already shown above, see figure 4.1). Obviously the simple model underestimates the resistance increase measured experimentally during the dealloying process, which occurs irrespective of whether the approximation is made or not.

Since the observed increase in sample resistance is entirely determined by the shrinkage of the alloy cross-section, the discrepancy emerging between prediction and measured data indicates, that the etching front proceeds through the sample faster than assumed in the simple model. This is however only possible, if there is a significant, ongoing faradaic transformation process taking place in the porous structure behind the etching front. This finding agrees with previous ex-situ electron microscopy studies by means of which the progress of a narrow etching front (referred to as 'primary' or 'bulk dealloying') could be distinguished from further etching processes in the porous network (referred to as 'secondary' or 'ligament dealloying') [45]. Thus, the recorded resistance increase is exclusively governed by the primary dealloying step, which is associated with a decrease in the master alloy cross section.

This means that the assumption of a simple proportionality between charge flow and relative porous cross section made in equation (5.3) is invalid. In fact, as also illustrated in figure 5.1, at a given time during dealloying the transferred charge Q is smaller than the charge Q' that would be necessary to generate the final porous condition in A_p. The ratio of these charges

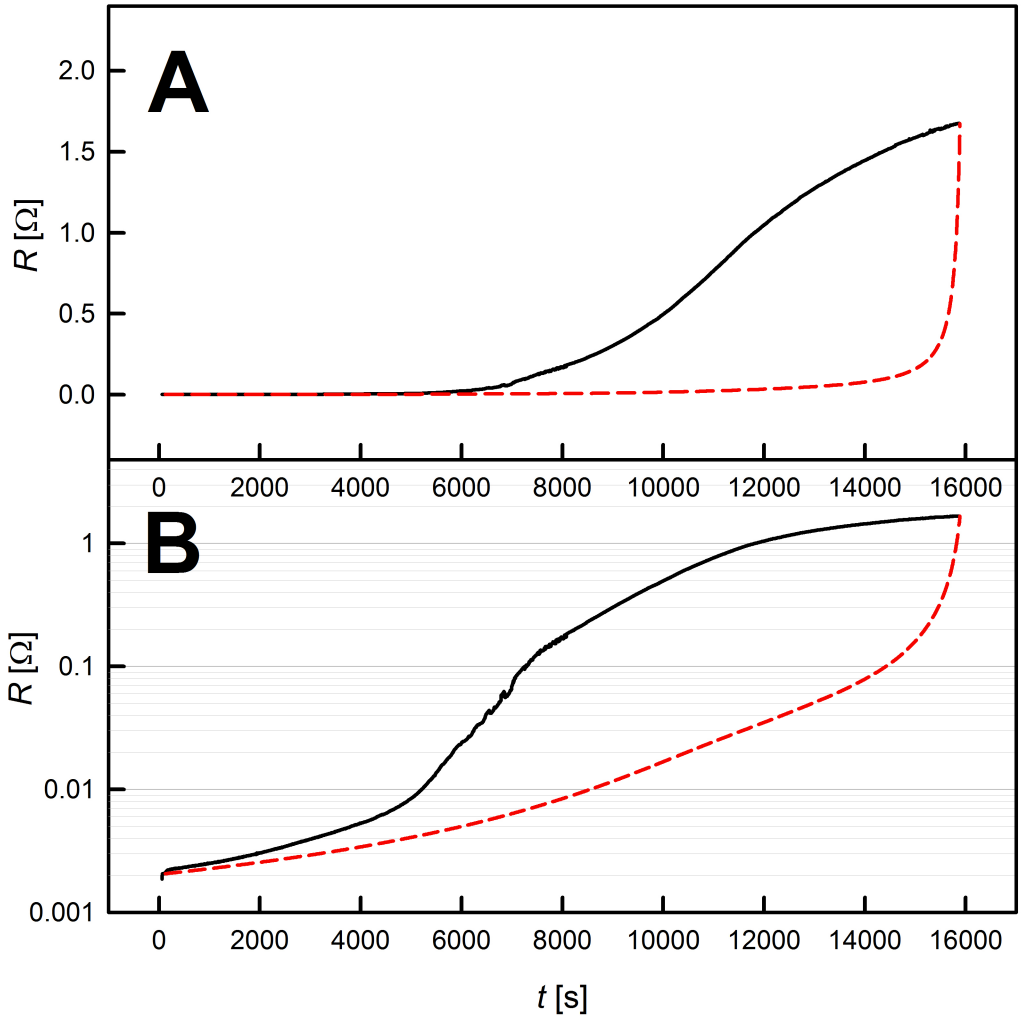

Figure 5.2: Comparison of the resistance increase predicted by the simple parallel circuit model in equation (5.4) (red dashed lines) with experimental dealloying data recorded for a $Ag_{73}Au_{27}$ master alloy (sample np-Au R1) in 0.1 M $AgNO_3$ solution (black curves) in linear (A) and logarithmic (B) scale.

$$a = \frac{Q}{Q'} = \frac{Q}{Q_{tot}\frac{A_p}{A_0}} = \frac{Q}{Q_{tot}(1 - \frac{R_0}{R})} \tag{5.5}$$

gives an average value to what extent the nanoporous network has reached its final condition, which in the following will be referred to as degree of dealloying. Given a simple proportionality of A_p with charge transfer, the degree of dealloying would equal 100 % during the entire etching process. Figure 5.3 shows the actual behavior: a increases steeply at the

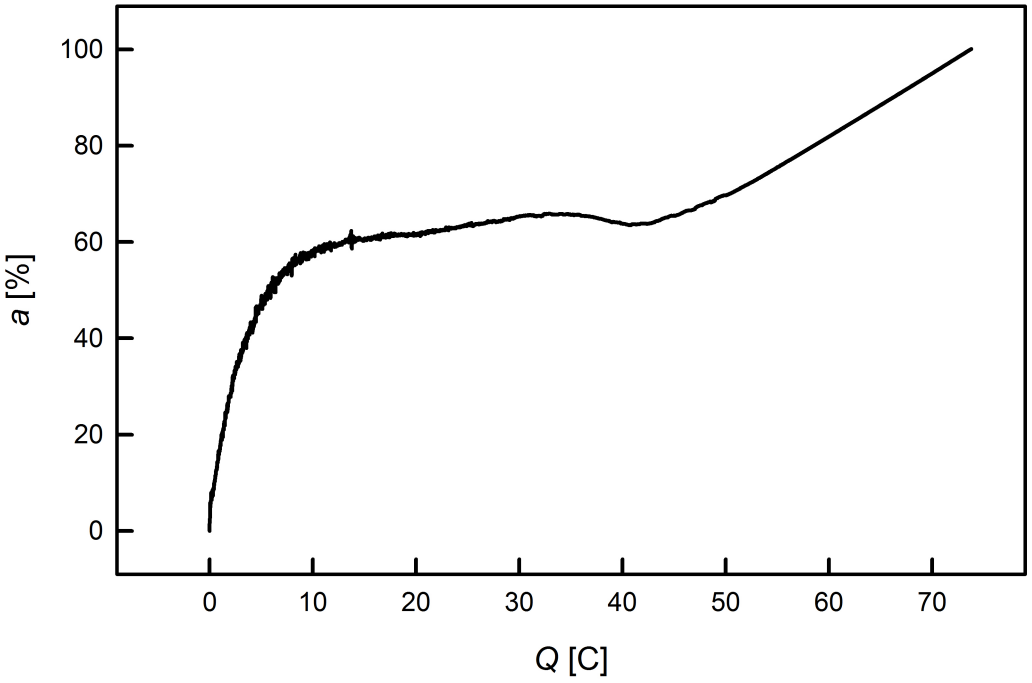

Figure 5.3: Average degree of dealloying a during the etching process of sample np-Au R1, determined from equation (5.5).

beginning and then becomes approximately constant over a wide range of the experiment, here approximately between 5 C and 45 C, before it starts to increase again until the structure reaches its final state with $a = 100\%$.

While a is constant, the progress of the etching front can be considered proportional to the charge flow. The limits of this regime have to be determined individually for each set of dealloying parameters. In the present case of np-Au, the degree of dealloying reaches a constant value at a charge transfer Q/Q_{tot} of about 10 %. However, since the resistance changes are very small in the early stages of dealloying, a can approximately be considered as constant from the beginning of the experiment until an upper limit characterized by a charge flow Q_c is reached. In the present case this upper limit lies at $Q_c/Q_{tot} = 60$ % (i.e. at $a \approx 60\%$), associated with a resistance $R_c = 26.6$ mΩ. Below this limit, the porous cross section A_p^* is considered to grow proportionally to the charge flow, along with a linear decrease of the master alloy cross section A_m^* which yields

$$\frac{A_m^*}{A_0} = 1 - \frac{Q}{Q_c}(1 - \frac{A_{m,c}}{A_0}) = 1 - \frac{Q}{Q_c}(1 - \frac{R_0}{R_c}). \tag{5.6}$$

In this regime where a is constant, also the averaged specific resistance ρ_p^* of the porous structure is constant, but has not yet reached its final condition ($\rho_p^* < \rho_p$). However a simple estimation shows that even if ρ_p^* were an order of magnitude smaller than ρ_p, the resistance contribution by the porous structure would amount to less than 10% of the total resistance while $A_p^*/A_0 < 90\%$. Therefore the overall resistance of the sample can still be reasonably considered as dominated by the master alloy backbone, which leads to an improved resistance prediction[1]

$$R_{||}^*(Q) = R_0 \frac{A_0}{A_m^*} = R_0 \frac{1}{1 - \frac{Q}{Q_c}(1 - \frac{R_0}{R_c})} \tag{5.7}$$

in the regime of constant a. This advanced model is plotted along with the data recorded during the formation of np-Au (sample np-Au R1) in figure 5.4 A, showing excellent agreement.

Figures 5.4B and C demonstrate, that the model is not only applicable to gold, but also agrees well with the dealloying curves recorded for palladium and platinum, respectively. As already described in section 4.1, both of these cases do not possess the smoothness of the comparable signal recorded for nanoporous gold (figure 5.4A). Nevertheless, the modified parallel circuit model shows also good agreement with the recorded data and, especially in the case of platinum, the model is applicable over a very wide range of the measurement up to $Q_x/Q_F = 90$ %. This difference of the upper limit between Pt and Au can be interpreted as caused by the higher melting point and therefore lower mobility of Pt atoms. Because of this, the primary dealloying process is more pronounced for Cu-Pt due to the formation of smaller ligaments, associated with a more thorough removal of Cu, which is in good agreement with the EDX measurements presented above (see chapter 4.3).

[1]For comparison with the simple model (equation (5.4)) it should be noted, that in the simple model $Q = Q'$.

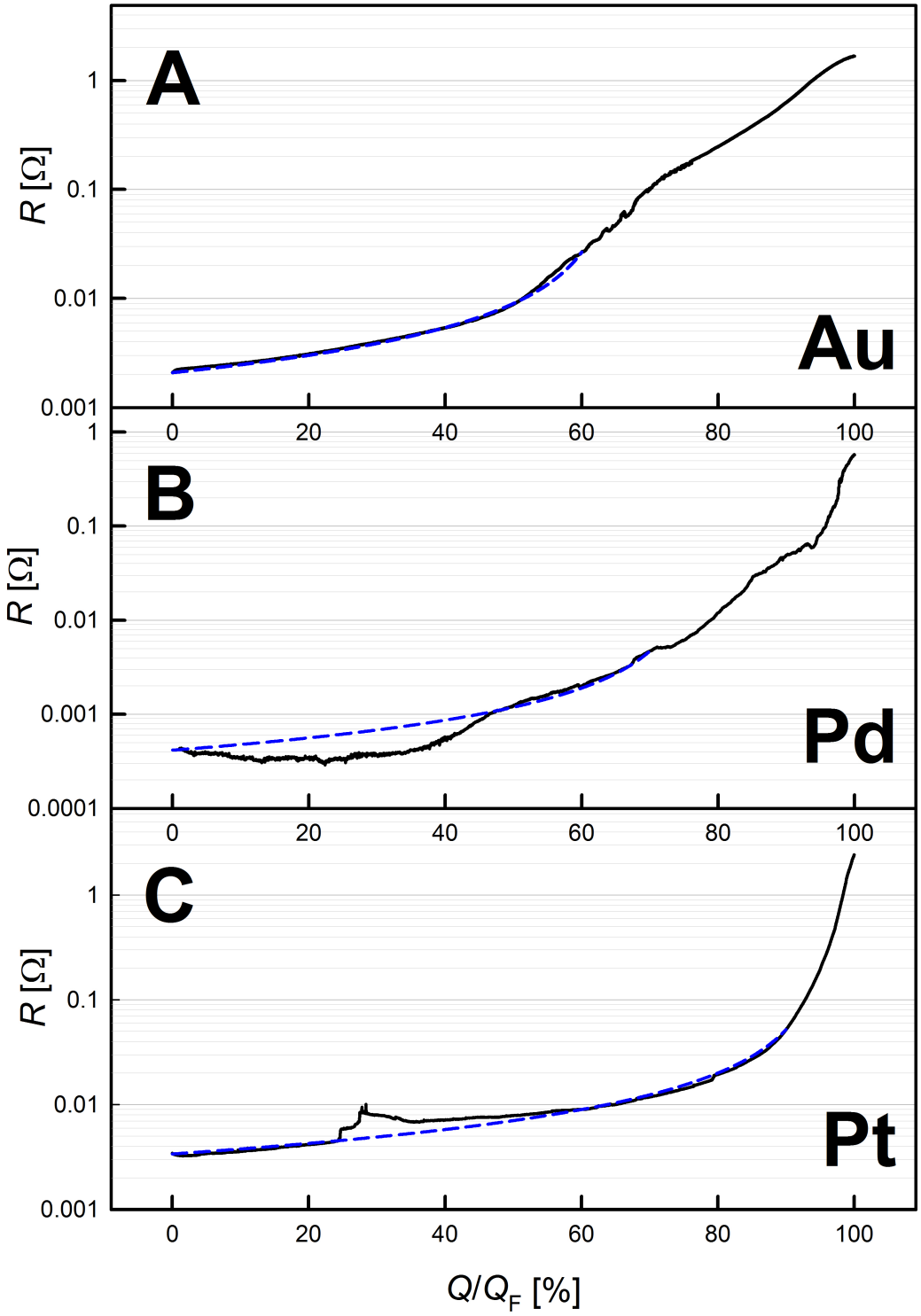

Figure 5.4: Comparison of the predicted resistance (blue, dashed), according to the improved parallel circuit model given in equation (5.7), with experimental data (black, solid) recorded during the dealloying process of np-Au R1 (A), np-Pd R1 (B) and np-Pt R1 (C) upon dealloying according to table 4.1.

The presented model is also rather stable towards thickness variations of the master alloy backbone along the sample, that might arise during the etching process. In a linear approximation small variations $|\Delta A| \ll A_0$ do not affect the resistance.

5.2 Tunable Resistance of Metallic Samples

The origin of the resistance tunability of porous nanoscaled metals can be considered to arise mainly from manipulations of the charge-carrier scattering at the metal-electrolyte interface. As discussed in previous studies [24, 29] the effect of a charging-induced actuation of nanoporous metals [23, 25, 27, 78] or of a variation of the charge carrier density on the resistance turned out to be insignificant. Following references [24] and [29] this will briefly be demonstrated in the following, using double layer charging of np-Pt R2 as an example. In the experiment shown in figure 4.13, the sample exhibited a resistance increase of about 1.1 % upon imposing a charge of approximately 6 As/g (positive charge coefficient $(\Delta R/R_0)/\Delta Q$).

Actuation

The expected resistance variation due to the actuator behavior can be calculated from

$$\frac{\Delta R}{R} = -\gamma K \frac{\Delta V}{V_0} \tag{5.8}$$

with the bulk modulus $K = -\Delta p \cdot (\Delta V/V_0)^{-1}$ of 278.3 GPa and the pressure coefficient $\gamma = \Delta p^{-1} \cdot \Delta R/R$ of -2.07×10^{-6} bar^{-1} [115] for platinum. In the investigated potential range, sample np-Pt D1 exhibited thickness variations $\Delta L/L_0$ of only 0.04 % (see figure 4.14), leading to an expected resistance variation no higher than 0.2 % in the investigated regime, which is more than a factor of 5 smaller than the observed value and which, therefore, can not account for the observed effect.

Charge Carrier Density

Imposing a positive charge Q=0.5 As/g to a material, as observed in the double layer region of np-Pt R2, corresponds to a removal of free charge carriers $\Delta n = Q/e = -0.3 \times 10^{19}$ g^{-1} with e being the elementary charge. Using the relationship

$$\frac{\Delta\sigma}{\sigma} = \frac{2}{3}\frac{\Delta n}{n} \tag{5.9}$$

taken from reference [63], an estimate for the resistance increase caused by a reduced charge carrier density can be given. However, assuming a contribution of 0.55-0.6 charge carriers per platinum atom [116], a resistance increase of only 0.012% would be expected due to the reduced number of electrons, which is two orders of magnitude smaller than the observed variation. Therefore a significant influence of this effect can be ruled out as well.

Scattering at the Metal-Electrolyte Interfaces

Concludingly the resistance is assigned to an increasing scattering probability of electrons at the crystal-electrolyte interface with positive charging, which was described for thin films by Tucceri and Posadas in 1990 [67]. As discussed intensively in the first work on resistance tuning of a three-dimensionally macroscopic sample, published by M. Sagmeister et al. [24], scattering is particularly important in the case of platinum due to its partially filled d band: The resistance of Pt sensitively depends on the scattering probability of conducting s electrons into available d band states, which strongly varies upon d band filling due to interfacial charging.

An attempt of an estimation given in [24], however, shows that the resistance variations due to variations in the density of states at the Fermi edge in the d band cannot be approximated in a simple manner. In the mentioned case, the resistance variation was overestimated by about a factor of 6 compared to the experimental results. This difference probably arises

due to some oversimplified assumptions made for the estimation, especially neglecting any contributions to the sample resistance other than interfacial ones. [24]

Nevertheless, even though a quantitative estimation is obviously difficult, a strong influence of interfacial scattering on the resistance tuning is evident simply by a comparison of the structure sizes of the porous, nanophase metals with the electron mean free paths in the respective elements. In fact, the pore and crystallite/ligment sizes of the structures used in the aformentioned articles [24, 29] as well as in the present work (e.g. see figures 4.37 and 4.38) are in the range of or even smaller than the bulk mean free paths λ_f of the investigated metals: $\lambda_{f,Pt} \approx 11$ nm [117], $\lambda_{f,Au} \approx 31$ nm [117], $\lambda_{Pd} \approx 25$ nm [118].

In the free electron model of conductivity [119]

$$\sigma = \frac{e^2 n \tau}{m} \tag{5.10}$$

with the elementary charge e, charge carrier density n and the electron mass m, the bulk conductivity of a metal is inversely proportional to the scattering rate τ^{-1}

$$\tau^{-1} = \frac{v_F}{\lambda_f} \tag{5.11}$$

which in this simple model only depends on λ_f and the Fermi velocity v_F.

In the present case of a porous nanophase solid with structural sizes in the range of λ_f, scattering at the interfaces gives a strong contribution to the scattering rate. Therefore interfacial manipulations, such as electrochemical charging, may strongly influence the electrical resistance. This picture is particularly supported by the fact, that for all investigated samples the strongest resistance variations could be generated in the oxygen regime (e.g. see figures 4.4, 4.10, 4.26 and 4.32). As already described in chapter 2.1, anions show a stronger tendency for specific adsorption due to their larger ionic radii and therefore weaker bound

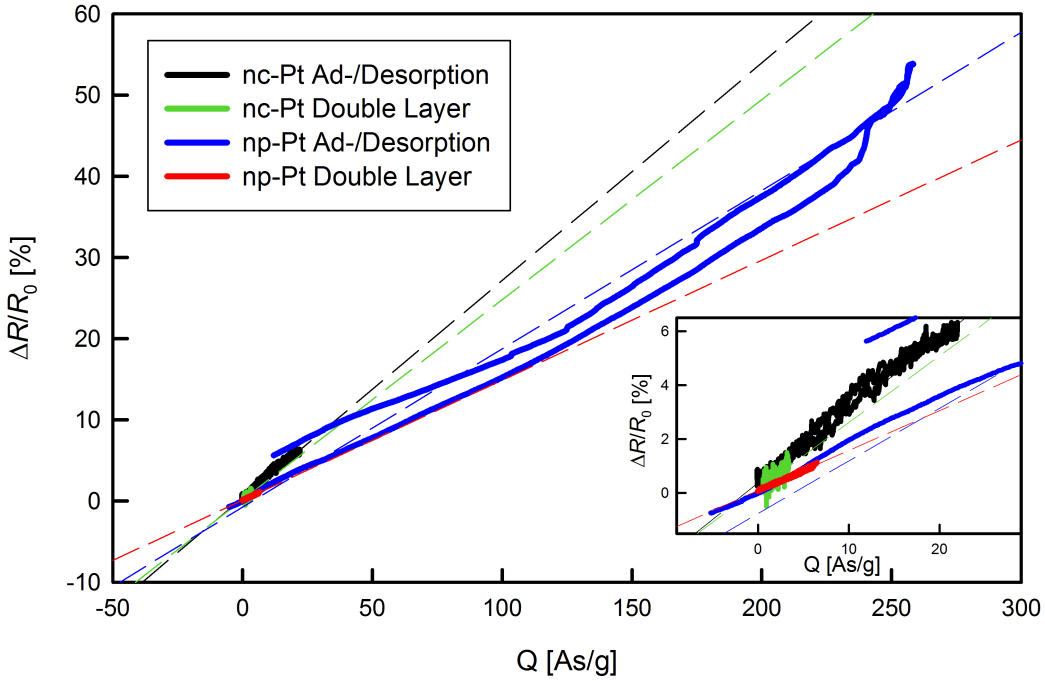

Figure 5.5: Resistance variations $\Delta R/R_0$ of np-Pt and nc-Pt upon imposing charges ΔQ in different electrochemical regimes. The linear regressions of the obtained data are given by dashed lines. The inset (lower right corner) shows a magnification of the resistance variations at small charge transfers.

solvation shells, forming additional scattering centers close to the sample surface.

For a systematic discussion of the present results, a summary of resistance variations and charge coefficients obtained in this work is given below in table 5.1, along with selected values from table 2.1 for comparison. Generally it can be said that significantly higher R variations could be obtained for the dealloyed materials compared to compacted powders. This finding can be attributed to the high surface-to-volume ratios obtained by dealloying and therefore higher achievable charge densities. A detailed discussion of possible influences, particularly relevant for dealloyed materials, will be presented in the following.

Structural Sizes and Charging Capacity

The most detailed resistometric investigations were performed for dealloyed, nanoporous platinum (np-Pt) and compacted Platinum Black (nc-Pt) in this thesis. The dependence of

the electrical resistance on imposed charge, observed for both sample types upon CV cycling is visualized in figure 5.5, each for the double layer regime (red: np-Pt, green: nc-Pt) and the regime of specific adsorption (blue: np-Pt, black: nc-Pt).

Due to the extremely high charging capacity of more than 300 As/g and the associated strong resistance increase that can be achieved for the dealloyed material in the regime of specific adsorption, the other curves can hardly be recognized in a full scale image of this plot. Therefore, an inset showing the resistance variations at small charge transfers is given in figure 5.5. Even though the achieved absolute resistance variations are smaller for nc-Pt, the slopes of the linear regressions (dashed lines), which represent the charge coefficients, show a higher sensitivity of R to imposed charge (stronger slopes) for the compacted powder (compare table 5.1), which will be adressed in the next subsection. The yet observed 4-fold increase of $(\Delta R/R_0)_{max}$ of np-Pt compared with nc-Pt simply arises from the much higher charging capacity upon adsorption/desorption (imposed charges as high as 300 As/g) which is possible due to the high surface-to-volume ratio of the dealloyed structures.

The values listed under 'oxidized' denote a steady state condition of Platinum Black well above the oxygen desorption peak where reversible charging is performed entirely within the oxygen adsorbed steady state without removing it.[2] Cycling nc-Pt in this condition results in a featureless, steady-state CV similar to that of the double layer regime of the sample (see figure 4.3). Therefore the charge transfer in this regime can be considered as 'double layer like' charging of a previously oxygen-covered surface. This results in a weaker response of the resistance, because charging does not directly affect the underlying platinum surface. This explains the lower charge coefficient of $0.7 \cdot 10^{-5}$ mol/As observed in this regime.

When nanoporous metals are subjected to charging treatments for elongated times, certain aging effects are observed, which was presented for sample np-Pt R2 in figure 4.15. With increasing lifetime, the sample resistance measured in the double layer regime as well as the resistance tunability tend to decrease, which occurs most probably due to slight structural

[2]Please note that the sign inverted resistance variations observed for the primary oxide and re-oxidized condition of dealloyed np-Pt samples will be treated separately in chapter 5.3.

Table 5.1: Maximum resistance variations $(\Delta R/R_0)_{max}$ and charge coefficients $(\Delta R/R_0)/\Delta Q$ of porous nanophase metals.

		$(\Delta R/R_0)_{max}$ [%]	$(\Delta R/R_0)/\Delta Q$ [10^{-5} mol/As]
Double Layer Charging			
nc-Pt	this work	0.8	1.3
np-Pt	this work	1	0.9
np-Au	this work	5	5.2
nc-Pt	Sagmeister et al. [24]	8	1.5
np-Au	Wahl et al. [29]	4	11.2
np-Au	Mishra et al. [28]	6	-
Specific Adsorption/Desorption			
nc-Pt	this work	15	1.6
nc-Pd	this work	14	1.4
np-Pt	this work	58	1.0
np-Au	this work	88	1.5
np-Pd	this work	26	2.6
np-Au	Wahl et al. [29]	43	4.6
Oxidized Sample (Pseudocapacitive Charging)[2]			
nc-Pt	this work	1	0.7

coarsening: if the ligament diameters in the porous structure grow due to rearrangement of the Pt atoms, the resistance, which is dominated by charge carrier scattering events at the metal-electrolyte-interfaces, is reduced. This reduction of the surface-to-volume ratio is associated with a weaker response to property tuning.

Residues of the Sacrificial Elements

As mentioned above, a comparison of the data recorded upon charging np-Pt and nc-Pt shows, that even though much higher resistance variations could be obtained for np-Pt, the charge coefficient $(\Delta R/R_0)/\Delta Q$, representing the sensitivity of R to imposed charge, is lower for the dealloyed material. This means, that the higher $(\Delta R/R_0)_{max}$ values simply arise from a higher charging capacity (see above).

Compared to np-Au also the resistance variations observed for the np-Pt samples are rather low: With $(\Delta R/R_0)_{max}$ =88 % the strongest resistance variation achieved so far by

ad-/desorption on a nanoporous metal could be recorded for np-Au in the framework of this thesis. The charge coefficient $(\Delta R/R_0)/\Delta Q$ of np-Au is also higher than that recorded for np-Pt in this work (see table 5.1), however, it is reduced by a factor of 2 to 3 compared to previous studies on np-Au available in the literature [28, 29]. To understand these trends, besides the ligament sizes of the nanoporous structures, also the specific resistances of the respective pure metals and possible influences by residues of the sacrificial elements have to be taken into consideration.

Even though the bulk resistivity of (pure) Pt is higher by a factor of 5 compared to that of Au [117], the relative resistivity increase due to residual Cu or Ag in np-Pt or np-Au, respectively, may be considered to be similar if one assumes that similar amounts of Cu or Ag remain after dealloying. This is because bulk Pt and Au exhibit a similar relative resistivity increase of about 10 % per 1 at% of doping [120, 121]. In fact, due to the low Cu-concentrations that remain in np-Pt (see tables 4.5 and 4.6), a reduction of the charge coefficient by dopants would even be expected to be less significant for np-Pt compared to np-Au, which is in contradiction to the observed trends. Therefore, irrespective of residual concentrations of the sacrifical elements, the different charging sensitivities of the relative resistance in np-Pt and np-Au are presumably caused by differences in the electron mean free path.

Due to the above discussed *s*-*d*-scattering, the electron mean free path $\lambda_{f,Pt}$ in pure coarse-grained Pt at ambient temperature is lower by about a factor of three than in Au ($\lambda_{f,Au}$=31 nm), which is also reflected in the five-fold higher bulk resistivity. Because of the shorter mean free path, scattering processes inside of the ligaments of the porous structure of np-Pt add more strongly to the overall scattering rate. Therefore the influence of charging-induced variations of the scattering at the metal-electrolyte interfaces is smaller compared with np-Au.

While the differences in the charge coefficients of Pt and Au obviously do not arise from remaining sacrificial alloy components, residues may yet be the reason for the abovementioned differences arising between nanostructures of the same element, produced by different

procedures: comparing np-Pt with nc-Pt, the slightly reduced sensitivity of np-Pt with respect to charging may be caused by a higher matrix resistance of np-Pt due to incompletely etched copper.

Also for np-Au, the reason for the extraordinarily strong resistance variations $(\Delta R/R_0)_{max}$ as well as the relatively small charge coefficients $(\Delta R/R_0)/\Delta Q$ obtained in the present work may be found in the preparation method: while the samples in the reference studies [28, 29] were dealloyed in diluted HNO_3 or $HClO_4$, representing the acids most commonly used for etching Ag-Au master alloys in the literature, a neutral silver nitrate solution ($AgNO_3$) was used in this work in order to prevent free corrosion. Dealloying in $AgNO_3$ is known to result in smaller ligament sizes (4-6 nm) but also higher amounts of residual silver [48], compared to conventional systems. This agrees very well with the present findings, since a higher amount of residual silver causes an increased matrix resistance and in further consequence a lower senisitivity to surface charging due to increased internal scattering, equivalent to the differences between nc-Pt and np-Pt discussed above.

With regard to $\Delta R/R$, the reason for the strong resistance variations up to 88 %, observed for np-Au, may be again be found in the small structural sizes (ligaments) and therefore high surface-to-volume ratio associated with high charging capacities: Similar to the results for np-Pt, charges up to about 300 As/g could be imposed to the np-Au samples in this thesis. At this point, however, also a resistance contribution by dissolution and redeposition of residual silver cannot be excluded, which might also be the reason for the slight drift towards higher R during repeated cycling (see figure 4.32) due to a loss of material by incomplete silver redeposition and therefore increasing porosity. Since the preliminary results obtained here promise an excellent tunability of the resistance of np-Au dealloyed in silver nitrate solution, these effects should be investigated in detail in future studies.

While the trends of the charge coefficients $(\Delta R/R_0)/\Delta Q$ observed for differently prepared gold and platinum samples can be explained by the concentration of impurities, the results obtained for palladium cannot: nc-Pd exhibits a behavior very similar to Platinum Black with a charge coefficient of 1.4×10^{-5} mol/As upon ad/desorption, for the dealloyed np-Pd

a charge coefficient almost twice as high (2.6×10^{-5} mol/As) is determined. This represents an opposite trend compared to dealloyed and powder compacted platinum (or also dealloyed np-Au with different Ag concentrations), where the sensitivity of R to charging was slightly reduced due to residues of the sacrificial element.

In the case of np-Pd as well as np-Pt, a dissolution/redeposition effect of the sacrificial elements (Co and Cu) appears rather unlikely. In contrast to np-Au dealloyed in $AgNO_3$, the preparation methods applied for the platinum and palladium samples result in low concentrations of the less noble alloy component, which was demonstrated in the present work for np-Pt (see table 4.5) and reported in the literature for np-Pd [52]. Moreover no signal of the sacrificial elements (exposed to the electrolyte) is visible in the cyclic voltammograms of the respective samples (see figures 4.10 and 4.26). Therefore a significant influence of dissolution/redeposition on the R-variation of np-Pd or np-Pt can reasonably be excluded and the high charge coefficient of np-Pd must be caused by a different effect.

Network Connectivity

Recently the influence of network connectivity, thus broken or dangling ligaments, was discussed in the literature with regards to the mechanical properties (strength and stiffness) of nanoporous gold [122]. This property certainly also influences the resistance behavior of nanoporous materials and may give an extraordinarily strong contribution for the present np-Pd samples: Since the master alloy used here for np-Pd was extremely dilute in Pd (20 wt% Pd, 80 wt% Co $\approx$ 12 at% Pd, 88 at% Co), which is only half as much as the concentration of the more noble elements in the master alloys used for np-Au and np-Pt, the nanoporous structure resulting after the dealloying process may contain strong damages on different scales. This may not only result in a complicated handling of the, even for a dealloyed material extraordinarily brittle, samples, which can even in primary-oxide condition hardly be grasped by tweezers without cracking, but also lead to (dis-)connections of cracks due to actuation. An expansion/contraction of the sample upon positive/negative charging may open/close electrical contacts in the nanoporous network which may in further

consequence lead to additional leaps/drops in the resistance with a rather fuzzy behavior as observed in figure 4.26.

Even though a contribution of crack-opening/-closing cannot be excluded completely in the case of np-Pt and np-Au, it can reasonably be assumed to be of minor significance, since opposite trends of the charging coefficients as well as smooth resistance variation curves were recorded upon charging. Moreover nanoporous gold and platinum were produced from master alloys with concentrations of the noble component being twice as high and the samples showed a significantly enhanced mechanic stabilty upon handling, compared to palladium, indicating reduced damage in the structure.

5.3 Primary Oxide of Dealloyed Materials

The primary oxide of dealloyed samples is associated with a characteristic behavior that strongly differs from the well-reduced condition. The actuation of (primary) oxidized np-Pt and np-Pd (see figures 4.18, 4.25 and 4.29) exhibits an opposite sign compared to well-reduced samples, which matches previous results obtained for compacted Pt nanopowder [62] as well as dealloyed np-Au [46].

The resistance behavior of nanoporous Pt in primary oxide condition is even more peculiar. Even though of slightly different shape from sample to sample - most probably sensitively dependent on the dealloying process - the resistance variation shows a characteristic sign inversion: upon positive as well as negative CV scan, R first increases and subsequently decreases. Thus relative resistance minima near the reversal points of the cyclic voltammogram are observed with maxima in between (e.g. figures 4.17 and 4.19). The sign inversion behavior of $\Delta R/R_0$ is considered to arise from the electronic structure of PtO that is present in the oxidized state. Several other possible effects could be excluded, which will be discussed briefly in the following.

Residual Copper

Similar to the possible dissolution/redeposition of rather high amounts of silver present in np-Au after dealloying in $AgNO_3$ (see previous chapter 5.2), an influence of residual copper on the behavior of np-Pt in primary oxide condition should be discussed here. Compared to platinum nanopowders, thin films or also well-reduced dealloyed samples cycled repeatedly in steady state, freshly dealloyed samples may contain higher amounts of Cu, which might be dissolved and redeposited in an - at least partially - reversible manner.

As shown for electrolytic Cu deposition on platinum thin films by Fujihara et al. [123], the development of a copper layer would provide additional charge carriers and thus cause a decrease of resistance. The dissolution/redeposition of metal atoms would therefore lead to a resistance increase/decrease upon positive/negative scan (as it is observed for the well reduced samples, see above). The behavior observed in the primary oxide, however, exhibits an opposite sign, showing a pronounced resistance minimum at the higher potential edge. Therefore residual copper can be ruled out as a reason for the sign inversion.

Cracks

The most simple explanation for the observed behavior would be a reversible opening and closing of cracks, like discussed for np-Pd. Even though this hypothesis can not easily be disproved completely, it appears rather unlikely. In this picture, a resistance increase/decrease would be directly related to an expansion/contraction of the sample. A sign inversion in the resistance would therefore require a sign inversion in the actuation as well, which is yet not observed in the investigated potential range (see figure 4.18). Moreover a fuzzy behavior of the resistance, as observed for np-Pd (see figure 4.26), would be expected upon (dis-)connecting cracks. The R-characteristics of np-Pt in the primary oxide however is reproducible and smooth.

Oxygen Coverage

For thin copper layers it has been shown in the literature, that O_2 adsorption from the gas phase can influence the electrical resistance by almost 10% [124]. As sketched in figure 5.6, adsorbing oxygen to a clean copper surface at first causes an increase of resistance due to increasingly diffuse charge carrier scattering at the surface. At a certain oxygen coverage, which will be referred to as diffuse scattering coverage in the following, the fraction of diffuse charge carrier scattering and thus the resistance, reaches its maximum. Further adsorption of oxygen will reverse this trend and make the resistance decrease again, as the adsorbate is approaching a smooth layer geometry, thus reducing diffuse scattering.

Applying these findings to the present data might bring up the suggestion, that the oxygen coverage of np-Pt in as-dealloyed condition lies slightly below the diffuse scattering coverage at the lower edge of the investigated potential range. When the oxygen coverage is increased by positive charging, in this picture the transition between positive and negative sign of charge coefficient (resistance maximum) would be associated with a surface oxygen coverage at which the most diffuse scattering occurs. Further positive charging associated with O-adsorption would then lead to a drop in resistance. In this context the slightly different R-characteristics observed from sample to sample might be understood as slight variations in the amount of oxygen induced during dealloying: the higher the initial oxygen coverage, the smaller the potential range of positive $(\Delta R/R_0)/\Delta Q$.

This hypothesis can however be ruled out based on the measurements recorded for well-reduced samples. Within the scanned potential range (e.g. shown for sample np-Pt R2 in figure 4.10), the oxygen adsorption on the sample clearly goes beyond one monolayer [113]. Since in the above presented picture a maximum of diffuse charge carrier scattering is associated with a semimonolayer coverage of oxygen and a minimum with an oxygen monolayer, a resistance maximum (semimonolayer coverage) followed by a resistance minimum (monolayer coverage) and finally an increasing resistance at higher adsorpiton would be expected upon scanning through the oxygen regime. The recorded resistance curve (figure 4.10) however

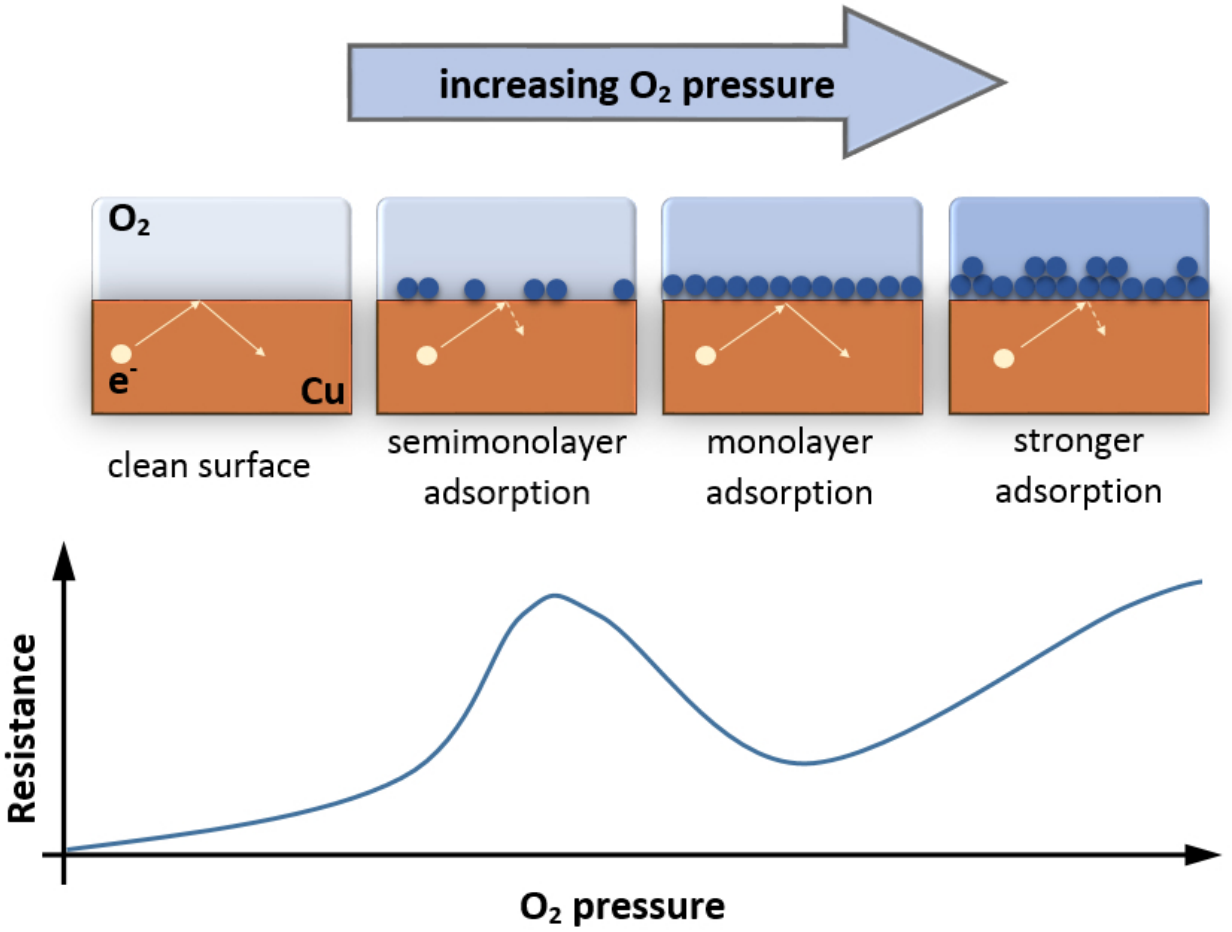

Figure 5.6: Schematic of the resistance variation of Cu thin films upon O_2 adsorption from the gas phase as described in reference [124]. Starting from a clean surface the electrical resistance increases by adsorption until at semimonolayer coverage the fraction of inelastic scattering processes reaches a maximum. By further adsorption the adsorbate layer is increasingly smoothened resulting in a decreasing resistance, which reaches a local minimum with ab adsorption of one monolayer. Stronger adsorption causes again a resistance increase.

constantly increases with O-adsorption during the entire positive scan.

Semiconducting Nature of PtO

After excluding the above discussed factors, the sign inversion behavior of np-Pt is assigned to the electronic structure of platinum monoxide (PtO). As shown by DFT calculations [125], PtO exhibits a minimum of the density of states (DOS) at the Fermi edge similar to graphite, which is sketched in figure 5.7. In graphite, due to this minimum, the DOS increases and, hence, the resistance decreases upon charging in both directions [81]. The same appears to

apply to the charging of the oxidized Pt sample: the resistance maximum observed upon positive as well as negative scan can be explained by passing through the DOS minimum. The exact potential of the maximum depends on the Fermi edge of the uncharged sample and thus the degree of oxidation.

As already mentioned above, the fact that the charging-induced property tuning substantially changes upon the removal or generation of a surface oxide has been known before for mechanical properties. For porous nanophase platinum produced from compacted Pt nanopowder, Viswanath et al. [62] reported on the opposite sign of the surface stress-charge coefficients[3], when reversibly switching from double layer charging (positive strain-charge response) to charging in the oxide layer regime (negative strain-charge response) by appropriate electrochemical treatment. Also here, the particular behavior of the oxide covered sample was considered to be associated with the electronic properties of PtO [62].

At this point it should be mentioned, that in spite of various attempts of oxidation including different charging sequences as well as electrolytes, no sign-change in the resistance tunability of powder compacted nc-Pt could be achieved in the present work. After strong oxidation the sample showed pseudocapacitive charging characteristics in the oxidized state with a reduced but still positive charge coefficient, as shown in figure 4.9 and discussed above in chapter 5.2. However it seems likely, that this discrepancy arises not due to monitoring different measurement parameters (actuation in [62], resistance here), but is rather caused by the fact, that the Platinum Black samples investigated in the present work had a significantly lower specific surface area compared to reference [62]. A high surface-to-volume ratio may, however, be crucial to obtain a sufficient oxidation per Pt atom in order to achieve the typical PtO behavior.

On the other hand for the np-Pt samples produced by dealloying, owing to an extraordinarily high specific surface, the behavior observed before removing the primary oxide can, at least partially be recovered by suitable re-oxidation, as demonstrated in figures 4.24 and

[3]not to be intermixed with a sign inversion within one CV scan as observed for the resistance in the present study

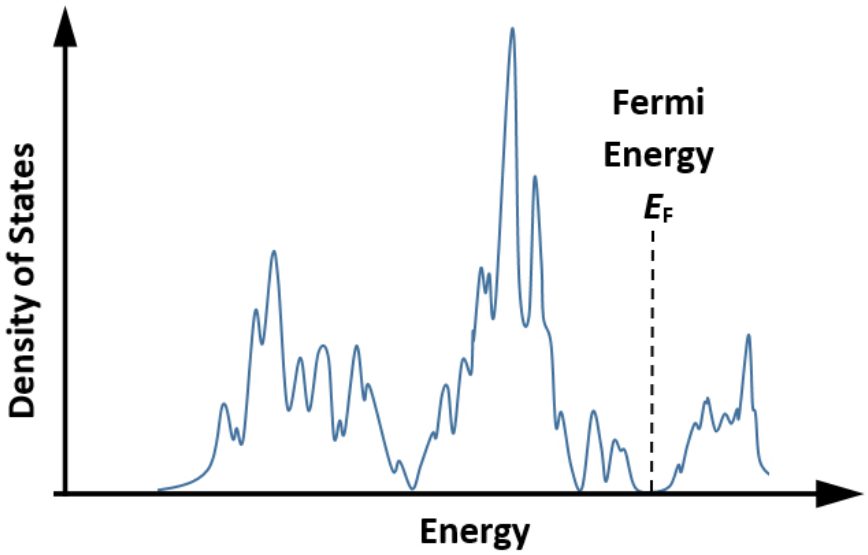

Figure 5.7: Sketch of the density of states of platinum monoxide (PtO) as obtained by DFT calculations in reference [125]. PtO exhibits semiconducting behavior with the Fermi Energy E_F located in a DOS minimum.

4.25. At the potential applied for strong oxidation ($U_{Ag/AgCl}$=+450 mV), site-exchange steps of adsorbed oxygen with underlying platinum atoms can be expected [126], which may affect a substantial portion of the sample, taking into account the fine porosity of the sample. With the recorded charge transfer of 0.7 oxygen species per Pt atom, the resulting nanoporous structure may become goverend by the behavior of PtO, exhibiting a qualitatively similar resistance behavior as in dealloyed state, while nc-Pt in the same potential regime preserved metallic conduction behavior.

Finally the primary oxide behavior of np-Pt will also be compared to previous studies on freshly dealloyed nanoporous gold. Also for np-Au, strongly different property-to-charge responses have been reported before and after reduction of the primary oxide [29, 46]. For the reistance variation of np-Au, a change in the magnitude, yet not in sign of the charge coefficient upon removing the primary oxide was observed [29]. The electrochemically induced length change of np-Au even showed opposing sign behavior of the surface stress-charge coefficients before and after reduction [46]. In both experiments on np-Au, however, once the primary oxide had been removed, the as-dealloyed behavior could not be regenerated by

re-oxidation in contrast to np-Pt.

This difference in behavior may again be related to the pore and ligament sizes of the respective nanoporous metals, which emerge due to differences in the atomic diffusivities that scale with the strongly different melting temperatures: While dealloyed gold is known for structural rearrangement during and after dealloying [4, 47, 48], coarsening processes are suppressed in np-Pt. This not only causes the extraordinarily fine porosity of dealloyed np-Pt [5] but also makes Pt applicable as a minor component in ternary dealloying systems to yield finer porosities [48].

Due to the low diffusivity of Pt, it can also be assumed that a reduction of the primary oxide of np-Pt may lead only to minor reordering. This assumption is supported by electron microscopy as shown above in figures 4.37 and 4.38. The retained, fine porosity enables re-oxidation conditions similar to those upon dealloying, at least partially regenerating the characteristics of the primary oxide, in contrast to np-Au.

5.4 Hydrogen Absorption in Nanoporous Palladium

For nanoporous palladium the focus of the investigations was placed on the hydrogen regime in this work, since the ability of Pd to absorb hydrogen into the bulk promises interesting effects with regards to property tuning. By cyclic voltammetry in the hydrogen regime at potentials $U_{Ag/AgCl}$ between −1000 mV and −550 mV property variations up to about $\Delta R/R_0$=10% and $\Delta L/L_0$=0.6% could be generated, which was presented in figure 4.27. For dilatometry (figure 4.27B) these results agree fairly well with the behavior of consolidated palladium nanoparticles, which was discussed within a model of electrocapillary coupling by Viswanath and co-workers [62].

For the resistance variation, the total charge flow of about −1.2 As recorded upon cycling at the said potentials arises from a transfer of about −0.3 As in the adsorption and −0.9 As in the absorption regime. Converting the latter into the absorbed hydrogen concentration c yields a H/Pd atomic ratio of about 5% associated with a variation of R of about 9.6%,

which corresponds to a resistance coefficient $(\Delta R/R_0)/c$ of about 1.9. At such low hydrogen concentrations, the electrical resistance of bulk Pd is known to be particularly sensitive to hydrogen absorption. Values for the resistance coefficient deduced from the literature range from 1.8 [127] to 2.3 [103].

The fact that the resistance coefficient $(\Delta R/R_0)/c$ determined here for np-Pd lies in the range of values recorded for bulk samples is, however, surprising: Since nanoporous metals possess a high initial resistance, governed by surface scattering processes [29], a lower sensitivity to additional scattering centers inside the crystal due to absorbed hydrogen would be expected. According to the small R variations observed in the regime of adsorption (see figures 4.26 and 4.27), a significant resistance contribution due to adsorbates (in analogy to the oxygen regime of porous nanophase metals [29, 32]), which might be superimposed to the absorption-related resistance increase, seems unlikely.

In analogy to the discussion of the resistance behavior in the oxygen regime (see chapter 5.2), a possible explanation of the strong R-variation may also here be found in the actuation behavior (compare the striking similarities between $\Delta R/R_0$ and $\Delta L/L_0$, figure 4.26). An expansion during hydrogenation may disconnect electrical contacts in the nanoporous network, leading to a resistance increase. Such a mechanical effect would also explain the noisy R-signal due to immediate resistance changes caused by opening/closing connections at various scales, such as broken ligaments or cracks, in the nanoporous network.

The dilatometric investigations were extended to higher hydrogen concentrations. The strong hydrogen loading, which was performed in chrono-amperometric and -potentiometric modes, is presented in table 4.4 and figure 4.28. Upon absorbing hydrogen up to an atomic ratio H:Pd of about 0.6 into the nanoporous structure, a strong actuation behavior up to more than 5% could be observed, representing the highest electrochemically induced actuation reported for a dealloyed material so far. This variation is significantly higher than predicted by literature data for bulk Pd [105], according to which an approximately linear variation of only about 3.5% would be expected at this concentration. Moreover, the maximum hydrogen solubility as well as the relative sensitivity of actuator response to

hydrogen loading obtained here also exceeds that recently reported for nanoporous palladium produced by free corrosion of an Al-Pd master alloy, which showed an actuation of about 3.3 % upon loading to a maximum hydrogen concentration of about 0.49 [96].

While the observed differences in the hydrogen solubilities most likely simply arise due to different hydrogenation parameters, such as the chosen electrolyte and charging procedure, the strong sensitivity of the sample expansion to hydrogenation is a material property, directly related to the nanoporosity of np-Pd, i.e., its high surface-to-volume ratio. Since nanoporous Pd possesses very fine pore sizes of 5-20 nm [5,52,128], which strongly depend on the dealloying parameters, a significant fraction of the total H absorption takes place on sites close to the surface. Being subjected to significantly lower constraints than atomic layers inside the bulk, superficial planes may show stronger outward relaxation during hydrogen uptake, similar to the surface-chemistry-driven actuation behavior known for nanoporous gold, which is caused by alterations in the atomic bindings in superficial layers [25].

6 | Summary and Conclusions

In the present thesis, porous nanophase metals were studied with regards to electrochemically induced variations of their physical properties, especially the electrical resistance. The major focus was placed on nanoporous platinum prepared by dealloying, but also nanoporous gold and palladium as well as compacted nanopowder samples of Pt and Pd were investigated. The key results can be grouped in four major topics: resistometric studies of the dealloying process, the tunable resistance of metallic nanoporous samples in the double layer as well as the O-adsorption regime, the primary oxide of materials prepared by dealloying, and the hydrogen absorption properties of nanoporous palladium.

Resistometric Studies of Dealloying

The resistance increase of samples upon electrochemical dealloying could be dynamically measured in-situ for the first time. During etching, the resistance increases by about three orders of magnitude due to nanoporosity evolution and concomitant oxide formation. It was shown, that etching proceeds in two stages, which are called 'primary (or bulk) dealloying', characterized by the progress of the etching front into the bulk master alloy, and 'secondary (or ligament) dealloying', referring to further etching in the already formed ligaments. The present findings represent the in-situ experimental confirmation of these processes proposed by Ye et al. in 2014, based on ex-situ electron microscopy [45].

A variable called the degree of dealloying a was introduced, characterizing the average etching progress in the already porous structure. This averaging approach, capable of describing dealloying over a wide range of the etching process of a macroscopic sample, perfectly complements earlier studies performed ex-situ and/or for microscopic portions of material. As long as the value of a is approximately constant, the resistance behavior can be very well described as governed by a reduction of the master alloy cross section, which is proportional to the transferred charge. Conductivity contributions of the parallel-connected nanoporous structure can be reasonably neglected due to its high specific resistance. The developed model was applied to three different alloy systems, yielding excellent agreement with the experiments in all cases.

To give a brief outlook on this particular topic, following these first results on the feasibility of a resistometric characterization of dealloying, the level and range where the degree of dealloying remains constant during the process should be investigated systematically with regards to alloy systems and etching parameters in future studies in order to gain a deeper understanding to the dealloying process.

Tunable Resistance of Metallic Porous Samples

The tunability of the electrical resistance of porous nanophase metals is governed by scattering processes at the metal-electrolyte interfaces. Therefore, dealloyed materials exhibit particularly strong resistance variations upon electrochemical charging due to their extraordinarily high surface-to-volume ratio. While for the samples produced by compacting a nanoporous powder, the highest generated resistance variations ranged around 15 % (nc-Pt), resistance variations of dealloyed metals due to reversible ad-/desorption reached up to about 25 % for np-Pd, almost 60 % for np-Pt and as high as 88 % for np-Au, representing the highest value reported for a nanoporous metal so far.

The reason for obtaining the strongest variation in the case of gold, even though np-Au exhibits significantly larger pores and ligaments than np-Pt and np-Pd, is interpreted to lie in the lower bulk resistivity and longer electron mean free path. In Pt and Pd, scattering

processes inside of the ligaments add more strongly to the overall scattering rate. These materials, therefore, react less sensitive to variations in interfacial scattering, compared to Au.

Dealloying-specific effects were evaluated by drawing a direct comparison between powder-compacted nc-Pt and dealloyed np-Pt. Interestingly, even though significantly higher relative changes could be generated for np-Pt than for nc-Pt, the charge coefficients $(\Delta R/R_0)/\Delta Q$, thus the relative sensitivity of the material's resistance per imposed charge, show an opposite trend. This difference in sensitivity is interpreted as caused by residues of the less noble element (here Cu) in the case of the dealloyed material, causing a higher matrix resistance, which makes the resistance less sensitive to interfacial scattering, while the strong absolute R variation in np-Pt simply arises from an enhanced absolute charge transfer due to the higher specific surface area.

Primary Oxide

Due to the dealloying process, nanoporous metals are strongly oxidized. This as-dealloyed condition, which is associated with material properties that fundamentally differ from well-reduced samples, is called the primary oxide. Carefully avoiding reduction, primary oxidized samples were studied with regards to actuation and resistance variations.

The charging-induced actuation of np-Pt and np-Pd in primary oxide condition was found to exhibit an opposite sign, compared to the reduced state of the samples, thus a contraction upon positive charging. This observation agrees well with previous reports on nc-Pt [62] and np-Au [46], where this behavior was discussed as being caused by less effective electronic screening in the oxidized material. This allows for a deeper penetration of an electronic excess charge imposed due to the electrochemical treatment, which weakens atomic bonds in surface-near layers and thus causes an expansion of the sample.

The resistance behavior of as-dealloyed np-Pt is even more peculiar: upon CV cycling in the primary oxide regime, the variation exhibits a sign inversion. The resistance reaches relative minima near the scan's reversal points and maxima in between, which is assigned to

the electronic structure of PtO. The observed resistance maximum is interpreted as beeing associated with a minimum density of states at the Fermi edge, as shown by DFT calculations for PtO [125]. In this case, a resistance decrease upon charging in both directions can be expected, similar to graphite [81].

Upon reduction of the primary oxide the conductivity of the nanoporous metal samples is strongly enhanced, in the case of np-Pt by about a factor of ten. The behavior characteristic for the primary oxide, can to some extent be regenerated for previously reduced samples. In fact, after re-oxidation under suitable conditions, the sign-inversion in the resistance variation is recovered, although with reduced amplitude.

Hydrogen Absorption in Nanoporous Palladium

Resistometry and dilatometry have proven as two efficient, independent methods to characterize the hydrogen concentration of np-Pd in-situ during electrochemical charging. The hydrogenation-induced expansion of the sample material was investigated in different charging sequences. The observed actuation up to 5 % is stronger than expected based on literature data, which may be due to the high surface-to-volume ratio of the present dealloyed samples.

Resistance variations of almost 10 % were observed upon H-absorption up to an atomic ratio of approximately 5 % H:Pd during cyclic voltammetry. Since this represents an unexpectedly strong dependence, besides charge carrier scattering processes also possible resistance contributions by actuation in the nanostructure were discussed.

To give a brief outlook, the influence of different master alloy compositions on the hydrogenation behavior of np-Pd is currently under investigation. Moreover, higher hydrogen concentrations might be achieved by using different electrolytes.

Bibliography

[1] G.Q. Lu and X. S. Zhao. *Nanoporous Materials: Science and Engineering*. Imperial College Press, London, 2004.

[2] J. Rouquerol, D. Avnir, C.W. Fairbridge, D.H. Everett, J.M. Haynes, N. Pernicone, J.D.F. Ramsay, K.S.W. Sing, and K.K. Unger. Recommendations for the characterization of porous solids (Technical Report). *Pure and Applied Chemistry*, 66(8):1739–1758, 1994.

[3] H.-D. Yu, M.D. Regulacio, E. Ye, and M.-Y. Han. Chemical routes to top-down nanofabrication. *Chemical Society Reviews*, 42(14):6006–6018, 2013.

[4] J. Erlebacher, M.J. Aziz, A. Karma, N. Dimitrov, and K. Sieradzki. Evolution of nanoporosity in dealloying. *Nature*, 410:450–453, 2001.

[5] Q. Chen and K. Sieradzki. Spontaneous evolution of bicontinuous nanostructures in dealloyed Li-based systems. *Nature Materials*, 12(12):1102–1106, 2013.

[6] J.-F. Huang and I.-W. Sun. Fabrication and Surface Functionalization of Nanoporous Gold by Electrochemical Alloying/Dealloying of Au-Zn in an Ionic Liquid, and the Self-Assembly of L-Cysteine Monolayers. *Advanced Functional Materials*, 15(6):989–994, 2005.

[7] F. Meng, X. Yan, J. Liu, J. Gu, and Z. Zou. Nanoporous gold as non-enzymatic sensor for hydrogen peroxide. *Electrochimica Acta*, 56(12):4657 – 4662, 2011.

[8] X.Y. Lang, H.T. Yuan, Y. Iwasa, and M.W. Chen. Three-dimensional nanoporous gold for electrochemical supercapacitors. *Scripta Materialia*, 64(9):923 – 926, 2011.

[9] X. Lang, A. Hirata, T. Fujita, and M. Chen. Nanoporous metal/oxide hybrid electrodes for electrochemical supercapacitors. *Nature Nanotechnology*, 6:232–236, 2011.

[10] V. Zielasek, B. Jürgens, C. Schulz, J. Biener, M.M. Biener, A.V. Hamza, and M. Bäumer. Gold Catalysts: Nanoporous Gold Foams. *Angewandte Chemie International Edition*, 45(48):8241–8244, 2006.

[11] R. Zeis, T. Lei, K. Sieradzki, J. Snyder, and J. Erlebacher. Catalytic reduction of oxygen and hydrogen peroxide by nanoporous gold. *Journal of Catalysis*, 253(1):132 – 138, 2008.

[12] A. Wittstock, V. Zielasek, J. Biener, C. M. Friend, and M. Bäumer. Nanoporous Gold Catalysts for Selective Gas-Phase Oxidative Coupling of Methanol at Low Temperature. *Science*, 327(5963):319–322, 2010.

[13] T. Fujita, P. Guan, K. McKenna, X. Lang, A. Hirata, L. Zhang, T. Tokunaga, S. Arai, Y. Yamamoto, N. Tanaka, Y. Ishikawa, Asao N., Y. Yamamoto, J. Erlebacher, and M. Chen. Atomic origins of the high catalytic activity of nanoporous gold. *Nature Materials*, 11(9):775–780, 2012.

[14] Y. Ding, M. Chen, and J. Erlebacher. Metallic Mesoporous Nanocomposites for Electrocatalysis. *Journal of the American Chemical Society*, 126(22):6876–6877, 2004.

[15] R. Zeis, A. Mathur, G. Fritz, J. Lee, and J. Erlebacher. Platinum-plated nanoporous gold: An efficient, low Pt loading electrocatalyst for PEM fuel cells. *Journal of Power Sources*, 165(1):65 – 72, 2007.

[16] L.Y. Chen, T. Fujita, and M.W. Chen. Biofunctionalized nanoporous gold for electrochemical biosensors. *Electrochimica Acta*, 67:1–5, 2012.

[17] X. Wang, X. Liu, X. Yan, P. Zhao, Y. Ding, and P. Xu. Enzyme-nanoporous gold biocomposite: excellent biocatalyst with improved biocatalytic performance and stability. *PLoS One*, 6(9):e24207, 2011.

[18] E. Seker, Y. Berdichevsky, M.R. Begley, M.L. Reed, K.J. Staley, and M.L. Yarmush. The fabrication of low-impedance nanoporous gold multiple-electrode arrays for neuralelectrophysiology studies. *Nanotechnology*, 21(12):125504, 2010.

[19] C.A.R. Chapman, H. Chen, M. Stamou, J. Biener, M.M. Biener, P.J. Lein, and E. Seker. Nanoporous gold as a neural interface coating: effects of topography, surface chemistry, and feature size. *ACS Applied Materials & Interfaces*, 7(13):7093–7100, 2015.

[20] E. Seker, Y. Berdichevsky, K.J. Staley, and M.L. Yarmush. Microfabrication-Compatible Nanoporous Gold Foams as Biomaterials for Drug Delivery. *Advanced Healthcare Materials*, 1(2):172–176, 2012.

[21] O. Kurtulus, P. Daggumati, and E. Seker. Molecular release from patterned nanoporous gold thin films. *Nanoscale*, 6(12):7062–7071, 2014.

[22] H. Gleiter, J. Weissmüller, O. Wollersheim, and R. Würschum. Nanocrystalline materials: a way to solids with tunable electronic structures and properties? *Acta Materialia*, 49(4):737 – 745, 2001.

[23] J. Weissmüller, R.N. Viswanath, D. Kramer, P. Zimmer, R. Würschum, and H. Gleiter. Charge-Induced Reversible Strain in a Metal. *Science*, 300(5617):312–315, 2003.

[24] M. Sagmeister, U. Brossmann, S. Landgraf, and R. Würschum. Electrically Tunable Resistance of a Metal. *Physical Review Letters*, 96:156601, Apr 2006.

[25] J. Biener, A. Wittstock, L.A. Zepeda-Ruiz, M.M. Biener, V. Zielasek, D. Kramer, R.N. Viswanath, J. Weissmüller, M. Bäumer, and A.V. Hamza. Surface-chemistry-driven actuation in nanoporous gold. *Nature Materials*, 2009.

[26] H.-J. Jin and J. Weissmüller. Bulk Nanoporous Metal for Actuation. *Advanced Engineering Materials*, 12(8):714–723, 2010.

[27] H.-J. Jin and J. Weissmüller. A Material with Electrically Tunable Strength and Flow Stress. *Science*, 332(6034):1179–1182, 2011.

[28] A.K. Mishra, C. Bansal, and H. Hahn. Surface charge induced variation in the electrical conductivity of nanoporous gold. *Journal of Applied Physics*, 103(9), 2008.

[29] P. Wahl, T. Traussnig, S. Landgraf, H.-J. Jin, J. Weissmüller, and Roland Würschum. Adsorption-driven tuning of the electrical resistance of nanoporous gold. *Journal of Applied Physics*, 108(7), 2010.

[30] E.-M. Steyskal, Z. Qi, P. Pölt, M. Albu, J. Weissmüller, and R. Würschum. Electrochemically Tunable Resistance of Nanoporous Platinum Produced by Dealloying. *Langmuir*, 32(31):7757–7764, 2016.

[31] E.-M. Steyskal, C. Wiednig, N. Enzinger, and R. Würschum. In situ characterization of hydrogen absorption in nanoporous palladium produced by dealloying. *Beilstein Journal of Nanotechnology*, 7(1):1197–1201, 2016.

[32] E.-M. Steyskal, S. Topolovec, S. Landgraf, H. Krenn, and R. Würschum. In situ monitoring magnetism and resistance of nanophase platinum upon electrochemical oxidation. *Beilstein Journal of Nanotechnology*, 4:394–399, 2013.

[33] E.-M. Steyskal, M. Besenhard, S. Landgraf, Y. Zhong, J. Weissmüller, P. Pölt, M. Albu, and R. Würschum. Sign-inversion of charging-induced variation of electrical resistance of nanoporous platinum. *Journal of Applied Physics*, 112(7), 2012.

[34] W. Schmickler. *Grundlagen der Elektrochemie*. Vieweg Lehrbuch Physikalische Chemie, Braunschweig/Wiesbaden, 1996.

[35] C.H. Hamann and W. Vielstich. *Elektrochemie*. Wiley-VCH, Weinheim Deutschland, 2005.

[36] J. Mitchell. *The art of precolumbian gold.* The Metropolitan Museum of Art, New York, 1985.

[37] D.E. Williams, R.C. Newman, Q. Song, and R.G. Kelly. Passivity breakdown and pitting corrosion of binary alloys. *Nature*, 350(6315):216–219, 1991.

[38] R.C. Newman and K. Sieradzki. Metallic corrosion. *Science*, 263(5154):1708–1710, 1994.

[39] R. Li and K. Sieradzki. Ductile-brittle transition in random porous Au. *Physical Review Letters*, 68(8):1168, 1992.

[40] I. McCue, E. Benn, B. Gaskey, and J. Erlebacher. Dealloying and dealloyed materials. *Annual Review of Materials Research*, 46:263–286, 2016.

[41] J. Erlebacher. An Atomistic Description of Dealloying: Porosity Evolution, the Critical Potential, and Rate-Limiting Behavior. *Journal of The Electrochemical Society*, 151(10):C614–C626, 2004.

[42] F.U. Renner, A. Stierle, H. Dosch, D.M. Kolb, T.L. Lee, and J. Zegenhagen. In situ x-ray diffraction study of the initial dealloying and passivation of $Cu_3Au(111)$ during anodic dissolution. *Phys. Rev. B*, 77:235433, 2008.

[43] C.J. Dotzler, B. Ingham, B.N. Illy, K. Wallwork, M.P. Ryan, and M.F. Toney. In situ observation of strain development and porosity evolution in nanoporous gold foils. *Advanced Functional Materials*, 21(20):3938–3946, 2011.

[44] T.P. Moffat, F.-R. F. Fan, and A.J. Bard. Electrochemical and Scanning Tunneling Microscopic Study of Dealloying of Cu_3Au. *Journal of The Electrochemical Society*, 138(11):3224–3235, 1991.

[45] X.-L. Ye, N. Lu, X.-J. Li, K. Du, J. Tan, and H.-J. Jin. Primary and Secondary Dealloying of Au(Pt)-Ag: Structural and Compositional Evolutions, and Volume Shrinkage. *Journal of The Electrochemical Society*, 161(12):C517–C526, 2014.

[46] H.-J. Jin, S. Parida, D. Kramer, and J. Weissmüller. Sign-inverted surface stress-charge response in nanoporous gold. *Surface Science*, 602(23):3588 – 3594, 2008.

[47] Y. Ding, Y.-J. Kim, and J. Erlebacher. Nanoporous Gold Leaf: Ancient Technology/Advanced Material. *Advanced Materials*, 16(21):1897–1900, 2004.

[48] J. Snyder, K. Livi, and J. Erlebacher. Dealloying Silver/Gold Alloys in Neutral Silver Nitrate Solution: Porosity Evolution, Surface Composition, and Surface Oxides. *Journal of The Electrochemical Society*, 155(8):C464–C473, 2008.

[49] Y. Ding and J. Erlebacher. Nanoporous metals with controlled multimodal pore size distribution. *Journal of the American Chemical Society*, 125(26):7772–7773, 2003.

[50] H. Ji, X. Wang, C. Zhao, C. Zhang, J. Xu, and Z. Zhang. Formation, control and functionalization of nanoporous silver through changing dealloying media and elemental doping. *CrystEngComm*, 13(7):2617–2628, 2011.

[51] D.V. Pugh, A. Dursun, and S.G. Corcoran. Formation of nanoporous platinum by selective dissolution of Cu from $Cu_{0.75}Pt_{0.25}$. *Journal of Materials Research*, 18:216–221, 2003.

[52] M. Hakamada and M. Mabuchi. Fabrication of nanoporous palladium by dealloying and its thermal coarsening. *Journal of Alloys and Compounds*, 479:326 – 329, 2009.

[53] J.R. Hayes, A.M. Hodge, J. Biener, A.V. Hamza, and K. Sieradzki. Monolithic nanoporous copper by dealloying Mn-Cu. *Journal of Materials Research*, 21(10):2611–2616, 2006.

[54] M. Hakamada and M. Mabuchi. Preparation of nanoporous Ni and Ni–Cu by dealloying of rolled Ni–Mn and Ni–Cu–Mn alloys. *Journal of Alloys and Compounds*, 485(1):583–587, 2009.

[55] H.-J. Jin, D. Kramer, Y. Ivanisenko, and J. Weissmüller. Macroscopically strong nanoporous Pt prepared by dealloying. *Advanced Engineering Materials*, 9(10):849–854, 2007.

[56] J. Snyder, P. Asanithi, A.B. Dalton, and J. Erlebacher. Stabilized nanoporous metals by dealloying ternary alloy precursors. *Advanced Materials*, 20(24):4883–4886, 2008.

[57] A. Henglein. Nanoclusters of semiconductors and metals: Colloidal nano-particles of semiconductors and metals: Electronic structure and processes. *Berichte der Bunsengesellschaft für Physikalische Chemie*, 101(11):1562–1572, 1997.

[58] E. Feigenbaum, K.h Diest, and H.A. Atwater. Unity-Order Index Change in Transparent Conducting Oxides at Visible Frequencies. *Nano Letters*, 10:2111, 2010.

[59] C. Lemier, S. Ghosh, R.N. Viswanath, G.-T. Fei, and J. Weissmüller. Charge induced variation of the magnetization in nanoporous Ni-Pd. *MRS Online Proceedings Library Archive*, 876, 2005.

[60] H. Drings, R.N. Viswanath, D. Kramer, C. Lemier, J. Weissmüller, and R. Würschum. Tuneable magnetic susceptibility of nanocrystalline palladium. *Applied Physics Letters*, 88:253103, 2006.

[61] A.K. Mishra, C. Bansal, M. Ghafari, R. Kruk, and H. Hahn. Tuning properties of nanoporous Au-Fe alloys by electrochemically induced surface charge variations. *Physical Review B*, 81:155452, 2010.

[62] R.N. Viswanath, D. Kramer, and J. Weissmüller. Adsorbate effects on the surface stress-charge response of platinum electrodes. *Electrochimica Acta*, 53(6):2757 – 2767, 2008.

[63] A. Deubner and K. Rambke. Leitfähigkeitsänderungen dünner aufgedampfter Silberschichten bei elektrostatischer Aufladung. *Annalen der Physik*, 452(6-8):317–328, 1956.

[64] H. Shimizu. Resistance change of an evaporated platinum film working as cathode or anode in acid solutions - I. Adsorption and desorption of atomic and molecular hydrogen. *Electrochimica Acta*, 13(1):27–44, 1968.

[65] H. Shimizu. Resistance change of an evaporated platinum film working as cathode or anode in acid solutions - II. Fractions of cathodic current in the catalytic and the electrochemical mechanisms of the hydrogen-evolution reaction. *Electrochimica Acta*, 13(1):45–58, 1968.

[66] T. Dickinson and P.R. Sutton. The study of adsorption by measurement of electrode resistance. *Electrochimica Acta*, 19(7):427–435, 1974.

[67] R.I. Tucceri and D. Posadas. The effect of surface charge on the surface conductance of silver in surface inactive electrolytes. *Journal of Electroanalytical Chemistry and Interfacial Electrochemistry*, 283(1-2):159–166, 1990.

[68] D. Körwer, D. Schumacher, and A. Otto. Resistance changes of thin film electrodes of silver. *Berichte der Bunsengesellschaft für Physikalische Chemie*, 95(11):1484–1488, 1991.

[69] V. Marichev. In situ volt-resistometric study of adsorption and premonolayer oxidation of copper in alkaline solutions in connection with some aspects of electrocatalysis. *Electrochimica Acta*, 41(16):2551–2562, 1996.

[70] C. Hanewinkel, H. Winkes, D. Schumacher, and A. Otto. Adsorption of metal cations precisely quantified by surface resistance of thin epitaxial silver film electrodes. *Electrochimica Acta*, 42(20-22):3345–3349, 1997.

[71] B. Xu, H. He, and N.J. Tao. Controlling the conductance of atomically thin metal wires with electrochemical potential. *Journal of the American Chemical Society*, 124(45):13568–13575, 2002.

[72] R. Tucceri. A review about the surface resistance technique in electrochemistry. *Surface Science Reports*, 56(3):85–157, 2004.

[73] S. Dasgupta, R. Kruk, D. Ebke, A. Hütten, C. Bansal, and H. Hahn. Electric field induced reversible tuning of resistance of thin gold films. *Journal of Applied Physics*, 104(10):103707, 2008.

[74] M. Ding, Q. He, G. Wang, H.-C. Cheng, Y. Huang, and X. Duan. An on-chip electrical transport spectroscopy approach for in situ monitoring electrochemical interfaces. *Nature Communications*, 6:7867, 2015.

[75] M.J. Schöning. Voltohmmetry - a New Transducer Principle for Electrochemical Sensors. In *Ultrathin Electrochemical Chemo-and Biosensors*, pages 117–140. Springer, 2004.

[76] C. Bansal, S. Sarkar, A.K. Mishra, T. Abraham, C. Lemier, and H. Hahn. Electronically tunable conductivity of a nanoporous Au - Fe alloy. *Scripta Materialia*, 56(8):705 – 708, 2007.

[77] Q. Bai, J. Zhang, C. Si, Z. Qi, and Z. Zhang. Lattice defects and oxide formation coupledly enhanced giant electrical resistance change in nanoporous silver. *Electrochimica Acta*, 206:26–35, 2016.

[78] H.-J. Jin, X.-L. Wang, S. Parida, K. Wang, M. Seo, and J. Weissmüller. Nanoporous Au-Pt Alloys As Large Strain Electrochemical Actuators. *Nano Letters*, 10(1):187–194, 2010.

[79] B. Kastening, M. Hahn, and J. Kremeskötter. The double layer of activated carbon electrodes part 2. Charge carriers in the solid material. *Journal of Electroanalytical Chemistry*, 374(1-2):159–166, 1994.

[80] S. Kazaoui, N. Minami, N.H.H.K. Matsuda, H. Kataura, and Y. Achiba. Electrochemical tuning of electronic states in single-wall carbon nanotubes studied by in situ

absorption spectroscopy and ac resistance. *Applied Physics Letters*, 78(22):3433–3435, 2001.

[81] J.N. Barisci, G.G. Wallace, D. Chattopadhyay, F. Papadimitrakopoulos, and R.H Baughman. Electrochemical properties of single-wall carbon nanotube electrodes. *Journal of the Electrochemical Society*, 150(9):E409–E415, 2003.

[82] J.N. Barisci, G.G. Wallace, D.R. MacFarlane, and R.H. Baughman. Investigation of ionic liquids as electrolytes for carbon nanotube electrodes. *Electrochemistry Communications*, 6(1):22–27, 2004.

[83] E. Pollak, I. Genish, G. Salitra, A. Soffer, L. Klein, and D. Aurbach. The dependence of the electronic conductivity of carbon molecular sieve electrodes on their charging states. *The Journal of Physical Chemistry B*, 110(14):7443–7448, 2006.

[84] P.W. Ruch, R. Kötz, and A. Wokaun. Electrochemical characterization of single-walled carbon nanotubes for electrochemical double layer capacitors using non-aqueous electrolyte. *Electrochimica Acta*, 54(19):4451–4458, 2009.

[85] J. Biener, S. Dasgupta, L. Shao, D. Wang, M.A. Worsley, A. Wittstock, J.R. Lee, M.M. Biener, C.A. Orme, S.O. Kucheyev, B.C. Wood, T.M. Willey, Hamza A.V., J. Weissmüller, H. Hahn, and T.F. Baumann. Macroscopic 3d nanographene with dynamically tunable bulk properties. *Advanced Materials*, 24(37):5083–5087, 2012.

[86] R. Waser and M. Aono. Nanoionics-based resistive switching memories. *Nature Materials*, 6(11):833–840, 2007.

[87] R. Waser, R. Dittmann, G. Staikov, and K. Szot. Redox-based resistive switching memories–nanoionic mechanisms, prospects, and challenges. *Advanced Materials*, 21(25-26):2632–2663, 2009.

[88] R. Waser. Resistive non-volatile memory devices. *Microelectronic Engineering*, 86(7):1925–1928, 2009.

[89] R.N. Viswanath and J. Weissmüller. Electrocapillary coupling coefficients for hydrogen electrosorption on palladium. *Acta Materialia*, 61(16):6301–6309, 2013.

[90] D. Kramer, R.N. Viswanath, and J. Weissmüller. Surface-stress induced macroscopic bending of nanoporous gold cantilevers. *Nano Letters*, 4(5):793–796, 2004.

[91] Y. Xue, J. Markmann, H. Duan, J. Weissmüller, and P. Huber. Switchable imbibition in nanoporous gold. *Nature Communications*, 5:4237, 2014.

[92] C. Stenner, L.-H. Shao, N. Mameka, and J. Weissmüller. Piezoelectric Gold: Strong Charge-Load Response in a Metal-Based Hybrid Nanomaterial. *Advanced Functional Materials*, 26(28):5174–5181, 2016.

[93] F. Weigend, F. Evers, and J. Weissmüller. Structural relaxation in charged metal surfaces and cluster ions. *Small*, 2(12):1497–1503, 2006.

[94] E. Detsi, M. Sellès Sànchez, P.R. Onck, and J.T.M. De Hosson. Nanoporous silver as electrochemical actuator. *Scripta Materialia*, 69(2):195–198, 2013.

[95] M. Hakamada, S. Matsumura, and M. Mabuchi. Electrochemical actuation of nanoporous Ni in NaOH solution. *Materials Letters*, 70:132–134, 2012.

[96] J. Zhang, Q. Bai, and Z. Zhang. Dealloying-driven nanoporous palladium with superior electrochemical actuation performance. *Nanoscale*, 8:7287–7295, 2016.

[97] J. Zhang, Y. Wang, C. Si, Q. Bai, W. Ma, H. Gao, and Z. Zhang. Electrochemical actuation behaviors of bulk nanoporous palladium in acid and alkaline solutions. *Electrochimica Acta*, 220:91–97, 2016.

[98] T. Graham. On the occlusion of hydrogen gas by metals. *Proceedings of the Royal Society of London*, 16:422–427, 1867.

[99] A. Sieverts. Die Aufnahme von Gasen durch Metalle. *Z. Metallkunde*, 21(2):37, 1929.

[100] J.R. Lacher. A theoretical formula for the solubility of hydrogen in palladium. *Proceedings of the Royal Society of London. Series A, Mathematical and Physical Sciences*, pages 525–545, 1937.

[101] H.P. Stout. The electrodeposition of hydrogen on palladium. *Discussions of the Faraday Society*, 1:107–114, 1947.

[102] Y. Fukai. *The Metal-Hydrogen System.* Springer-Verlag Berlin Heidelberg New York, 1993.

[103] T.B. Flanagan and F.A. Lewis. Hydrogen absorption by palladium in aqueous solution. *Transactions of the Faraday Society*, 55:1400–1408, 1959.

[104] A. Vertova, S. Rondinini, and G. Busca. Monitoring hydrogen absorption in pd electrodes by means of electric and electrochemical signals. *Journal of Applied Electrochemistry*, 32(6):661–670, 2002.

[105] R. Feenstra, R. Griessen, and D.G. De Groot. Hydrogen induced lattice expansion and effective HH interaction in single phase PdHc. *Journal of Physics F: Metal Physics*, 16(12):1933, 1986.

[106] D.H. Everett and P.A. Sermon. Crystallite size effects in the palladium/hydrogen system: a simultaneous sorption and X-ray study. *Zeitschrift für Physikalische Chemie*, 114(114):109–122, 1979.

[107] R. Kirchheim, T. Mütschele, W. Kieninger, H. Gleiter, R. Birringer, and T.D. Koble. Hydrogen in amorphous and nanocrystalline metals. *Materials Science and Engineering*, 99(1):457–462, 1988.

[108] Y. Li and Y.-T. Cheng. Hydrogen diffusion and solubility in palladium thin films. *International Journal of Hydrogen Energy*, 21(4):281–291, 1996.

[109] T.B. Flanagan, R. Balasubramaniam, and R. Kirchheim. Exploring Lattice Defects in Palladium and Its Alloys Using Dissolved Hydrogen. *Platinum Metals Review*, 45(4):166–174, 2001.

[110] R. Kirchheim. Solid solutions of hydrogen in complex materials. *Solid State Physics-Advances in Research and Applications*, 59:203–292, 2004.

[111] V. Climent and J.M. Feliu. Thirty years of platinum single crystal electrochemistry. *Journal of Solid State Electrochemistry*, 15(7-8):1297, 2011.

[112] S. Trasatti and O.A. Petrii. Real surface area measurements in electrochemistry. *Journal of Electroanalytical Chemistry*, 327(1-2):353–376, 1992.

[113] H. Angerstein-Kozlowska, B.E. Conway, and W.B.A. Sharp. The real condition of electrochemically oxidized platinum surfaces. *Journal of Electroanalytical Chemistry and Interfacial Electrochemistry*, 43(1):9 – 36, 1973.

[114] S. Parida, D. Kramer, C.A. Volkert, H. Rösner, J. Erlebacher, and J. Weissmüller. Volume change during the formation of nanoporous gold by dealloying. *Physical Review Letters*, 97:035504, 2006.

[115] P.W. Bridgman. The electrical resistance of metals under pressure. *Proceedings of the American Academy of Arts and Sciences*, 52:573–646, 1917.

[116] P. Bizet and S.S. Minn. Effect of a Transverse Electric Field in Thin Metal Films. *Comptes Rendus Hebdomadaires des Seances de l'Academie des Sciences B*, 289(13):225–228, 1979.

[117] J. Vancea, H. Hoffmann, and K. Kastner. Mean free path and effective density of conduction electrons in polycrystalline metal films. *Thin Solid Films*, 121(3):201–216, 1984.

[118] S.M. Shivaprasad, Udachan L.A., and M.A. Agadi. Electrical resistivity of thin palladium films. *Physics Letters A*, 78(2):187, 1980.

[119] J.M. Ziman. *Principles of the Theory of Solids*. Cambridge University Press, 1972.

[120] J.O. Linde. Röntgenographische und elektrische Untersuchungen des CuPt-Systems. *Annalen Der Physik*, 422(2):151–164, 1937.

[121] C.Y. Ho, M.W. Ackerman, K.Y. Wu, T.N. Havill, R.H. Bogaard, R.A. Matula, S.G. Oh, and H.M. James. Electrical resistivity of ten selected binary alloy systems. *Journal of Physical and Chemical Reference Data*, 12(2):183–322, 1983.

[122] N. Mameka, K. Wang, J. Markmann, E. T Lilleodden, and J. Weissmüller. Nanoporous Gold - Testing Macro-scale Samples to Probe Small-scale Mechanical Behavior. *Materials Research Letters*, 4(1):27–36, 2016.

[123] M. Fujihara and T. Kuwana. Studies of electrochemical interfaces of thin Pt film electrodes by surface conductance. *Electrochimica Acta*, 20(8):565–573, 1975.

[124] J.S. Chawla, F. Zahid, H. Guo, and D. Gall. Effect of o_2 adsorption on electron scattering at cu(001) surfaces. *Applied Physics Letters*, 97(13):132106, 2010.

[125] J. Uddin, J.E. Peralta, and G.E. Scuseria. Density functional theory study of bulk platinum monoxide. *Physical Review B*, 71(15):155112, 2005.

[126] G. Jerkiewicz, G. Vatankhah, J. Lessard, M.P. Soriaga, and Y.-Su. Park. Surface-oxide growth at platinum electrodes in aqueous H_2SO_4: Reexamination of its mechanism through combined cyclic-voltammetry, electrochemical quartz-crystal nanobalance, and Auger electron spectroscopy measurements. *Electrochimica Acta*, 49(9):1451–1459, 2004.

[127] F. Fischer. Untersuchungen über die Widerstandsänderung von Palladiumdrähten bei der Wasserstoffokklusion. *Annalen der Physik*, 325(8):503–526, 1906.

[128] Y.K. Cao, X.Y. Ma, Y.Z. Chen, G.B. Shan, and F. Liu. Size effect of ligaments on charge induced surface stress response of nanoporous Pd prepared by dealloying. *Scripta Materialia*, 123:1–4, 2016.

Acknowledgements

I would like to express my sincerest gratitude to the following persons for their contributions to the success of this project:

Univ.-Prof. Dr. Roland Würschum,
Insitute of Materials Physics, TU Graz,
for giving me the opportunity to write this thesis at his institute and for always providing a pleasant, respectful working atmosphere. I am grateful for the valuable supervision and guidance through the past years and especially for the support during the writing process of this thesis and of our articles.

Prof. Dr. Hai-Jun Jin,
Institute of Metal Research, Chinese Academy of Sciences,
for acting as the external reviewer of this thesis.

Univ.-Prof. Dr. Reinhard Pippan,
Erich Schmid Institute of Materials Science, Austrian Academy of Sciences,
for accepting to act as the external member of the board of examiners for my thesis defence.

Dr. Stefan Topolovec,
formerly Insitute of Materials Physics, TU Graz,
for our longtime collaboration, many valuable discussions and especially for the productive work on our joint publication.

Dipl.-Ing. Michael Seidl, Markus Gössler and Lukas Weissitsch,
former/present master students at the Insitute of Materials Physics, TU Graz,
for the inspiring collaborations during their master theses I had the pleasure to co-supervise.

Prof. Dr.-Ing. Jörg Weissmüller, Dr. Zhen Qi, Dr. Yi Zhong and Dr. Matthias Graf,
Materials Physics and Technology, TU Hamburg-Harburg,
for providing sample materials and for many fruitful discussions.

Priv.-Doz. Dr. Peter Pölt and Dr. Mihaela Albu,
Institute of Electron Microscopy and Nanoanalysis, TU Graz,
for the morphological characterization of nanoporous platinum by SEM and TEM.

Prof. Dr. Stephan Landgraf,
Institute of Physical and Theoretical Chemistry, TU Graz,
for valuable advice in electrochemistry and especially for dealloying the first set of nanoporous platinum samples.

Prof. Dr. Heinz Krenn,
Institute of Physics, KFU Graz,
for fruitful discussions, especially during the writing process of our joint article.

Prof. Dr. Norbert Enzinger and Dipl.-Ing. Christopher Wiednig,
Institute of Materials Science and Welding, TU Graz,
for preparing the Co-Pd master alloys by electron beam melting.

Priv.-Doz. Dr. Christoph Hugenschmidt and Dipl.-Phys. Samantha Zimnik,
FRM II, TU München
for their support at the FRM II and especially for providing XPS spectra of nanoporous platinum.

Dr. Maximilian Besenhard and Dr. Thomas Traußnig,
formerly Insitute of Materials Physics, TU Graz,
for designing the first resistometry setup for dealloyed samples and for giving me an introduction to electrochemical property tuning.

Dr. Martin Luckabauer,
formerly Insitute of Materials Physics, TU Graz,
for his help during setting up the electrochemistry dilatometer.

All present and former members of the Institute of Materials Physics, TU Graz,
for all their help and support and especially also for the enjoyable working atmosphere.

My family
for their love, patience and support. Especially my parents, Annemarie and Johannes, for teaching me the most valuable things in life and for giving me so many great opportunities, my husband, Klemens, for being my perfect counterpart, for always believing in me and for unconditionally supporting everything I do, and my kids, Isabella and Konstantin, for being an inexhaustable source of motivation and for daily reminding me of what is really important.

AFFIDAVIT

I declare that I have authored this thesis independently, that I have not used other than the declared sources/resources, and that I have explicitly indicated all material which has been quoted either literally or by content from the sources used. The text document uploaded to TUGRAZonline is identical to the present doctoral thesis.

Date

Signature